

Charmonium and bottomonium production in heavy-ion collisions

R. Rapp,¹ D. Blaschke,^{2,3} and P. Crochet,⁴

¹ Cyclotron Institute and Physics Department, Texas A& M University
College Station, Texas 77843-3366, USA

Email: rapp@comp.tamu.edu

²Institute for Theoretical Physics, University of Wroclaw
Max Born pl. 9, 50-204 Wroclaw, Poland

Email: blaschke@ift.uni.wroc.pl

³Bogoliubov Laboratory for Theoretical Physics
JINR Dubna, 141980 Dubna, Russia

⁴Laboratoire de Physique Corpusculaire
F-63000 Clermont-Ferrand, France

Email: crochet@clermont.in2p3.fr

November 10, 2019

Abstract

We review the present status in the theoretical and phenomenological understanding of charmonium and bottomonium production in heavy-ion collisions. Starting from an introductory historical perspective, recapitulating the basic notion of “anomalous quarkonium suppression” in heavy-ion collisions, we develop ingredients and concepts aimed at a comprehensive approach to utilize heavy quarkonia as a probe of hot and dense matter. The theoretical discussion encompasses recent lattice QCD computations of quarkonium properties in the Quark-Gluon Plasma, their interpretations based on effective potential models, inelastic rate calculations and insights from the analyses of electromagnetic plasmas. In particular, we emphasize the powerful techniques of thermodynamic Green functions (T-matrices) which provide a rather general framework to implement microscopic quantities into a description of heavy quarkonium suppression and regeneration within a kinetic theory. The theoretical concepts are tested in applications to heavy-ion reactions at SPS, RHIC and LHC. We outline perspectives for future experiments on charmonium and bottomonium production in heavy-ion collisions over a large range in energy (FAIR, RHIC-II and LHC) which are expected to answer key questions in using quarkonium probes of hadronic matter under extreme conditions.

Contents

1	Historical Summary and Introduction	2
2	Equilibrium Properties of Charmonia	7
2.1	Correlation and Spectral Functions from Lattice QCD	8
2.2	Potential Models in the QGP	11
2.3	Charmonium Dissociation Reactions in the QGP	18
2.4	Effective Models in Hadronic Matter	22
2.5	Insights from Plasma Physics	25
3	Quarkonia in Heavy-Ion Collisions	32
3.1	Charmonium Transport	33
3.2	Nuclear Absorption and Pre-Equilibrium Effects	37
3.3	Applications at SPS, RHIC and LHC	40
3.3.1	Centrality Dependence	41
3.3.2	Transverse-Momentum Spectra and Elliptic Flow	45
3.3.3	Rapidity Distributions	47
3.3.4	Excitation Function	48
3.3.5	Excited Charmonia	49
3.3.6	Bottomonia	50
4	Future experiments	52
4.1	Quarkonia in heavy ion collisions at the RHIC-II	53
4.1.1	Experimental conditions	54
4.1.2	The PHENIX experiment	54
4.1.3	The STAR experiment	55
4.2	Quarkonia in heavy ion collisions at the LHC	55
4.2.1	Experimental conditions	57
4.2.2	The ALICE experiment	57
4.2.3	The CMS experiment	57
4.2.4	The ATLAS experiment	60
4.3	Quarkonia in heavy ion collisions at the SIS-300	60
4.3.1	Experimental conditions	61
4.3.2	The CBM experiment	61
5	Summary	62

1 Historical Summary and Introduction

The properties of heavy quarkonium states (charmonium and bottomonium) in a hot and/or dense strongly interacting medium have been intensely studied over the last 20 years, both experimentally and theoretically. Upcoming heavy-ion collision experiments at the Relativistic Heavy-Ion Collider (RHIC, at Brookhaven National Laboratory (BNL) in New York), at the Large Hadron Collider (LHC, at the European Center for Nuclear Research (CERN) in Geneva) and at the future Facility for Antiproton and Ion Research (FAIR, at the Heavy-Ion Research Center (GSI) at Darmstadt) carry heavy quarkonium programs as an essential component in their campaign. The strong interest in heavy quarkonia in medium is justified by the decisive role that they have played (and are expected to play) in the diagnostics of the highly excited nuclear medium created in ultrarelativistic heavy-ion collisions. The most prominent example is the celebrated J/ψ suppression effect as a possible signal of the formation of a Quark-Gluon Plasma (QGP) which was suggested by Matsui and Satz [1] in 1986 and which was instrumental in triggering the experimental programs at CERN, BNL and the future GSI facility, accompanied by as a broad spectrum of theoretical work (see, e.g., Ref. [2]). After many years of analysis and interpretation of the SPS data, with a first round of RHIC results completed, and with new insights on heavy-quarkonium properties from thermal lattice QCD accompanied by theoretical analysis, it is very timely to assess the current theoretical and experimental status prior to the next stage of developments. In the remainder of this introduction we will mainly elucidate important aspects of the physics of charmonia in a hot and dense medium to illustrate the difficulties in an unambiguous interpretation of the observed J/ψ suppression in heavy-ion collisions at SPS and RHIC.

The production of heavy quark pairs in nuclear collisions is a hard (i.e., high-momentum transfer) process which is rather well separated from the soft physics governing the evolution of a potentially formed QGP in the subsequent evolution. However, the formation of heavy quarkonia and heavy mesons may be well modified by final-state interactions induced by a surrounding hot medium. The first and now widely discussed probe in this context is the J/ψ . The original suggestion [1], somewhat contrary to naive expectations at the time, asserted that with increasing center-of-mass energy (cms) energy in a heavy-ion collision a suppression of the J/ψ peak in the dimuon invariant-mass spectrum should occur, relative to the (Drell-Yan) continuum. The underlying mechanism was based on the dissociation of the charmonium bound state in a dense medium, due to a “Debye” screening of the binding potential, largely driven by a deconfinement of color charges and thus intimately connected to the formation of a QGP. Such a mechanism is, in fact, a rather general one, very similar to the dissolution of atomic bound states in electromagnetic plasmas, or to the Mott transition [3] in semiconductors [4] where under high pressure electrons become delocalized and a conduction band emerges, signaling the plasma state.

Shortly after the prediction of J/ψ suppression, the NA38 experiment at the CERN-SPS found evidence for this effect in collisions of 200 AGeV oxygen (O) projectiles with uranium (U) nuclei, see Fig. 1.

The interpretation that the formation of a QGP had been signaled by this observation was immediately challenged by more conventional explanations in terms of inelastic J/ψ scattering on “primordial” target and projectile nucleons [7] (i.e., before the formation of the QGP), as well as on secondary produced hadronic comovers [8, 9]. The systematic experimental analysis of the nuclear mass-number dependence of J/ψ production in proton-nucleus (p -A) collisions at CERN (NA3, NA38) and FNAL (E772), together with collision systems with light-ion projectiles (O-U, S-U, Cu-U) at CERN, indeed confirmed that the J/ψ suppression in all these experiments could be understood in a unified way by the primordial absorption of the charmonium state on its path of mean length L through cold nuclear matter at density $n_0 = 0.16 \text{ fm}^{-3}$, with no further reinteractions before being detected via its dimuon decay. The suppression systematics could be quantitatively described following the simple absorption law, $S_{\text{nucl}} = \exp(-\sigma_{\text{abs}} n_0 L)$. In p -A collisions, the mean path length is determined by the radius, $R_A = 1.2 \text{ fm } A^{1/3}$, of the target nucleus as $L_A = \frac{3}{4} R_A$ while for A-B collisions one obtains

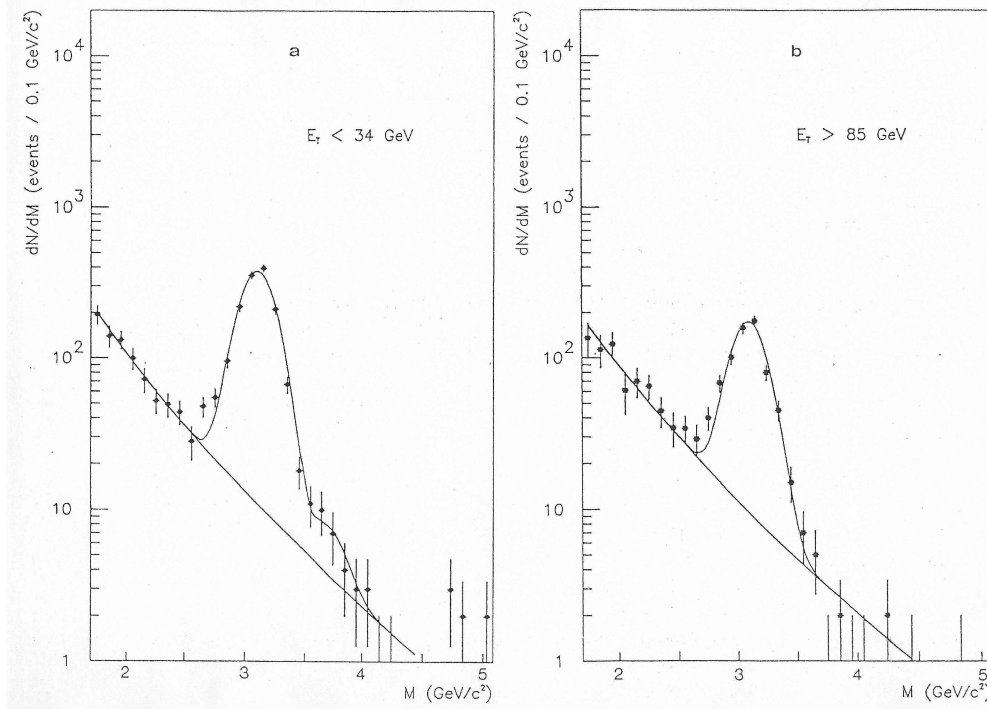


Figure 1: First observation of the J/ψ suppression effect in O(200 AGeV)–U collisions in the NA38 experiment at CERN-SPS. When comparing the invariant-mass spectrum of muon pairs produced in peripheral (collisions characterized by a small transverse energy $E_T < 34$ GeV; left panel) with that in central collisions (at high transverse energy, $E_T > 85$ GeV; right panel), a reduction of the J/ψ signal over the Drell-Yan continuum is apparent (from [5]).

$L_{AB} = L_A + L_B$. In fact, it came as somewhat of a surprise that this “nuclear absorption” systematics could account for not only the p –A but also for the A–B collision systems, see Fig. 2; the QGP signal seemingly had vanished [6]!

The situation changed when the Pb beam became available at the CERN-SPS. In central Pb(158 AGeV)–Pb collisions the successor experiment of NA38, NA50, found a significantly stronger J/ψ suppression than predicted by the extrapolation of the nuclear absorption law (based on the Glauber model) [10, 11]. This marked deviation was dubbed “anomalous J/ψ suppression”, as opposed to the “normal suppression” caused by absorption in cold nuclear matter (following the scaling with the L -variable introduced above). A first interpretation of the anomalous suppression as a signal for QGP formation was given by Blaizot and Ollitrault [12] within a “threshold-suppression” scenario. The latter is based on the assumption that a charm-anticharm quark pair cannot hadronize into a charmonium state when it is produced in a region where the transverse density of participant nucleons exceeds a certain “critical” value, n_p^{crit} , see Fig. 1. This scenario provided a consistent explanation with available data in the sense that the value for n_p^{crit} (characterizing the maximal energy density of the subsequently formed medium) required to describe the suppression in Pb–Pb was larger than the maximum value n_p reached in the light-ion systems (see also Ref. [13] for further details).

This initial interpretation was followed by a wide variety of theoretical investigations including hadronic comover dissociation, parton-induced break-up reactions in the QGP, pre-equilibrium effects, and combinations thereof. One of the controversially discussed issues was (and still is) whether the data provide evidence for some sort of threshold or onset behavior in terms of step-like patterns in the centrality dependence. Further clarification was hoped to be provided by studying intermediate size collision system, which was recently done by the NA60 collaboration using In(158 AGeV)–In colli-

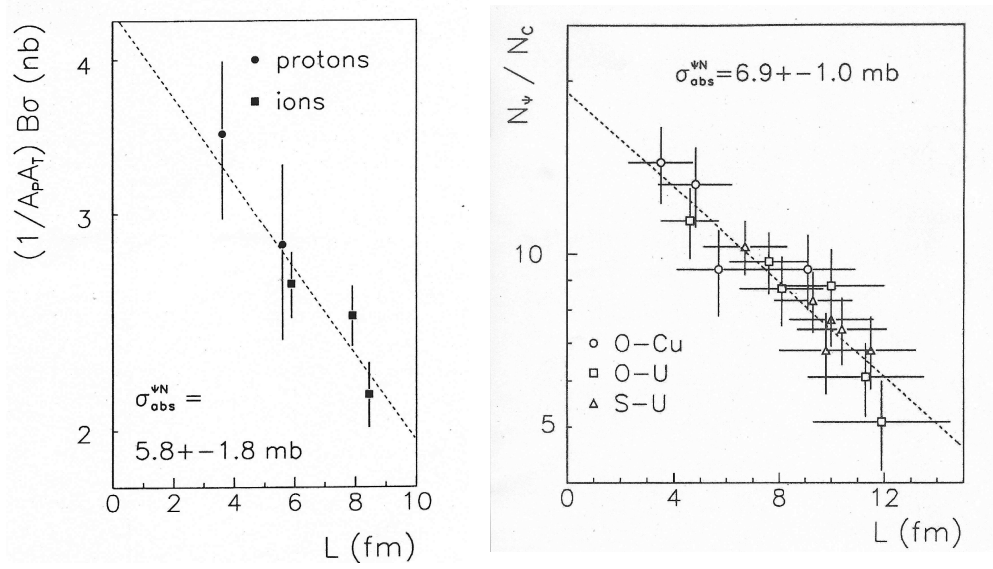


Figure 2: Nuclear absorption describes J/ψ suppression in p -A as well as A-B collision experiments, as long as the mass numbers are small enough [6]. For refined measurements of the absorption cross section, see below.

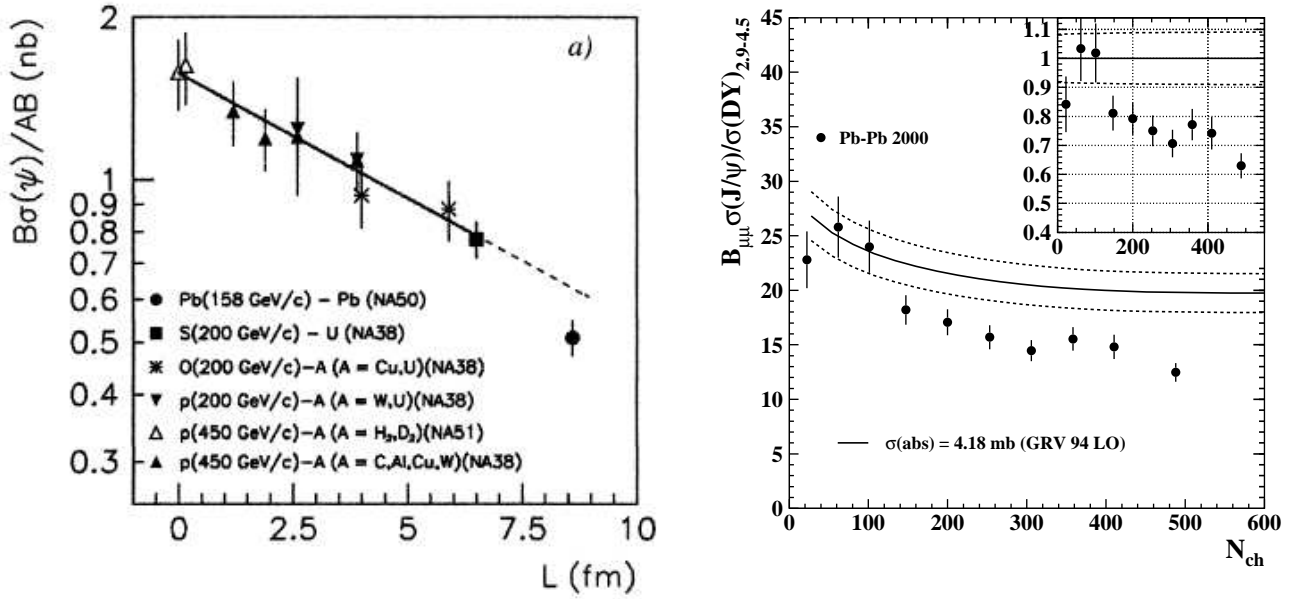


Figure 3: Anomalous J/ψ suppression in Pb(158 AGeV)-Pb collisions at the CERN-SPS measured by the NA50 experiment [10].

sions [14]. In particular, it could be confirmed that the “onset” of anomalous J/ψ suppression does not follow a scaling with the Glauber variable L but rather with the number of participants in the collision and thus a quantity related to the density of secondary particles, eventually forming a QGP cf. Fig. 5.

In the context of the CERN summary of the fixed-target heavy-ion program at the SPS in the year 2000, indicating the formation of a new form of matter in Pb(158 AGeV)-Pb collisions, the NA50 collaboration concluded that the J/ψ suppression pattern provides evidence for deconfinement of quarks and gluons [16]. In the same year the experimental program at RHIC commenced. Fig. 6 shows the

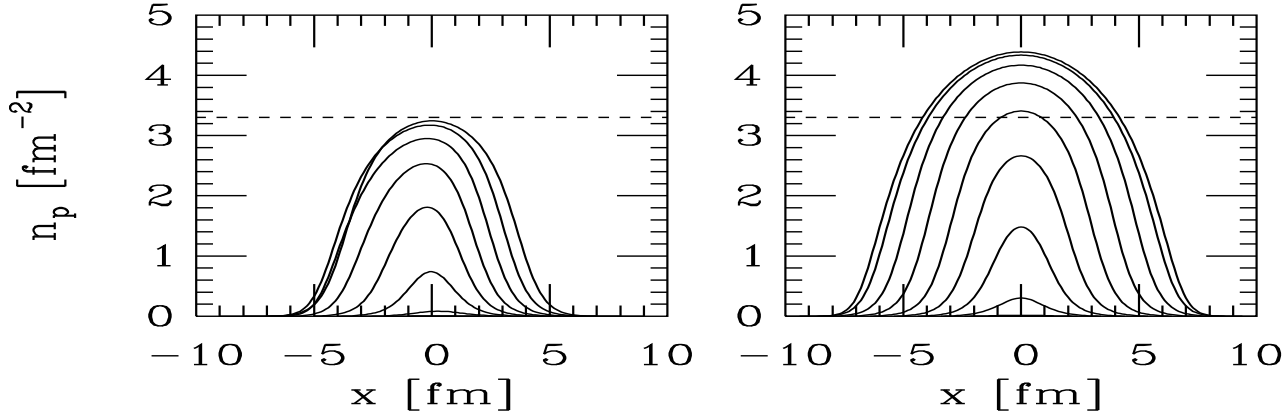


Figure 4: The transverse density of participants, n_p , in S-U (left) and Pb-Pb (right) collisions along the direction of the impact parameter vector, \vec{b} , for different values of $b = 0, 2, 4, \dots$ fm. The dashed line indicates the adopted threshold value $n_p^{\text{crit}} = 3.3 \text{ fm}^{-2}$ for the onset of anomalous J/ψ suppression. Figure taken from Ref. [12].

experimental data for J/ψ production in terms of the so-called nuclear modification factor, R_{AA} , as a function of centrality. It is defined as the yield observed in a heavy-ion reaction relative to the one in pp collision multiplied by the number, N_{coll} , of binary N - N collisions,

$$R_{AA}(N_{\text{part}}) = \frac{N_{AA}^{J/\psi}}{\langle N_{\text{coll}} \rangle N_{pp}^{J/\psi}}. \quad (1)$$

In the absence of any suppression (or medium effects) one expects $R_{AA}=1$. While the anomalous suppression of charmonium production was confirmed in semi-/central Au-Au collisions, its magnitude turned out to be very similar to what had been observed at the SPS. At first sight, this is a rather surprising result in view of the factor of 10 higher collision energy at RHIC, associated with much higher initial energy densities. However, it had been, predicted [21, 22, 120, 23], that under RHIC and LHC conditions the copious production of open charm leads to an additional source of J/ψ production due to the recombination of charm quarks (or charmed mesons) in the hot and dense medium. Calculations including both suppression and regeneration mechanisms [23] had predicted that a much stronger “anomalous” suppression would be largely compensated by secondary production via charm-anticharm coalescence. This is illustrated in the left panel of Fig. 6 where a comparison with reaction kinetic models for J/ψ production [17, 18] shows that a naïve extrapolation of the concept of an additional “anomalous” J/ψ suppression channel in a QGP environment from CERN-SPS to RHIC would fail. Additional support for this kinetic explanation of the J/ψ yield at RHIC follows from the observation that J/ψ suppression is less pronounced at central rapidity relative to forward rapidity, since at central rapidity the regeneration effect is larger due to a larger charm content in the medium, while dissociation mechanisms alone should increase the suppression due to larger energy densities attained.

The above discussion has given a first indication of the complexity in describing and understanding the various facets figuring into quarkonium observables in heavy-ion collisions, let alone their interpretation in terms of properties of the Quark-Gluon Plasma. It is thus mandatory to identify key concepts and combine them into a comprehensive approach that allows for a systematic interpretation of experimental data under a broad range of conditions (encompassing, e.g., all available collision energies, from FAIR via SPS and RHIC to LHC). This will be the main objective of this article, by means of a critical review of existing approaches and their comparison to data. An essential ingredient to such approaches are controlled reference points, e.g., equilibrium matter for in-medium properties, or p -A

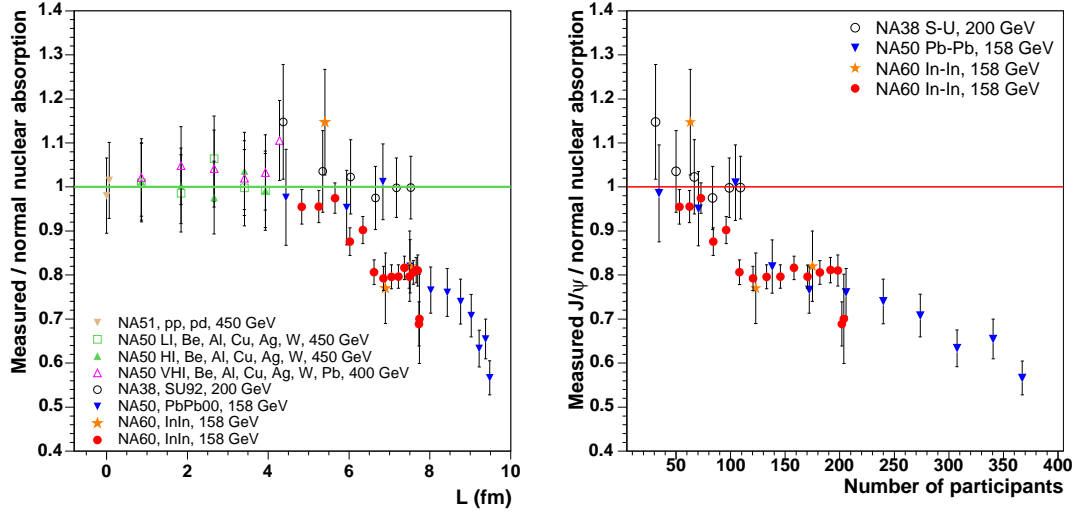


Figure 5: “Anomalous” J/ψ production (i.e., relative to expectations from normal nuclear absorption) in In(158 AGeV)–In collisions measured by the NA60 experiment compared to other projectile-target combinations at the CERN-SPS. The “threshold” for anomalous suppression appears to scale with the number of participants (right panel) rather than with the Glauber variable L (left panel). Taken from [15].

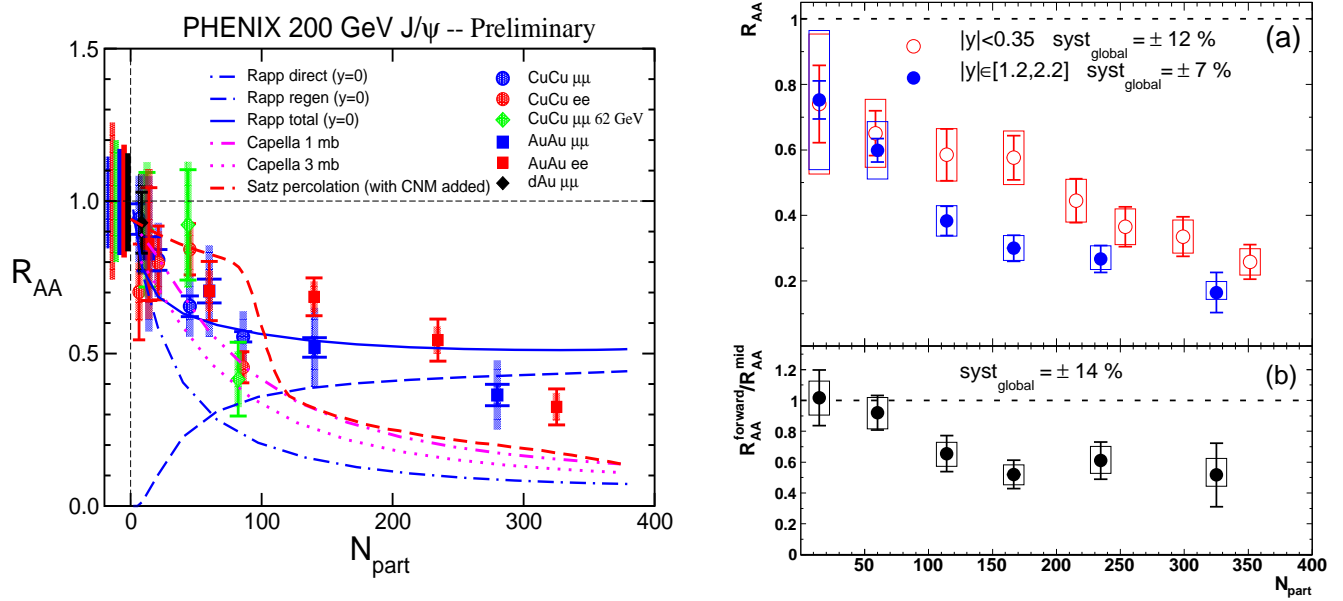


Figure 6: J/ψ production, relative to the binary-collision scaled yield in pp collisions, measured in the PHENIX experiment in $\sqrt{s_{NN}} = 200$ GeV Au–Au collisions at RHIC. Left panel: comparison with kinetic models [17, 18] of charmonium production at central rapidity, illustrating the importance of secondary J/ψ production via charm-anticharm recombination (figure from Ref. [19]). Right panel: increase of J/ψ suppression at forward relative to central rapidity, lending further support to the importance of charmonium regeneration mechanisms (from Ref. [20]).

collisions to separate “normal” nuclear effects from hot/dense matter effects. Our article is roughly organized according to the following decomposition of the problem:

(1) **Equilibrium properties of charmonia** (Sec. 2): these provide the main link between properties of the QGP and the medium created in heavy-ion collisions. The key quantity to be determined is the

thermodynamic spectral function: its pole mass (binding energy) largely determines the equilibrium abundancies (in connections with the properties of open charm), while in-/elastic reaction rates determines thermal and chemical relaxation times and are encoded in the spectral widths.

(2) **Charmonium transport** (Sec. 3.1), which is required to evaluate the coupling of the charmonia to the medium by computing the evolution of their phase space distribution, starting from realistic initial conditions. In principle, this evolution progresses toward equilibration, e.g., as a function of transverse momentum. The method of choice is a transport treatment incorporating regeneration reactions which are essential to allow for a relaxation toward thermal and chemical equilibrium. Since regeneration processes directly draw on open-charm spectra, a reliable assessment of the latter becomes mandatory.

(3) **Initial spectra and pre-equilibrium interactions** (Sec. 3.2): these determine the initial condition of the transport equation in item (i); they include modifications relative to spectra in pp collision (p_t broadening via Cronin effect, shadowing), as well as absorption and rescattering on primordial nucleons and secondary particles in the pre-equilibrium evolution of the medium.

(4) **Observables** (Sec. 3.3): to be computed by combining all of the above, where as an extra ingredient a realistic modeling of the bulk medium evolution is required, ideally (if applicable) in terms of a locally thermalized medium if, e.g., within a hydrodynamic evolution, or in terms of transport models in (kinetic) regimes of incomplete thermalization.

In Sec. 4 we give an outlook on the capabilities of, and physics questions to be addressed with, future experiments at LHC, RHIC-II and FAIR, while Sec. 5 contains a brief summary.

2 Equilibrium Properties of Charmonia

The full (gauge-invariant) information about the interactions in a given hadronic (color-singlet) channel with quantum numbers, α , is encoded in the two-point correlation function of the pertinent current, j_α . In coordinate space the correlator is defined by the amplitude of creating the current at the origin, propagating it to point (τ, \vec{r}) and absorbing it,

$$G_\alpha(\tau, \vec{r}) = \langle \langle j_\alpha(\tau, \vec{r}) j_\alpha^\dagger(0, \vec{0}) \rangle \rangle . \quad (2)$$

In a heat bath, the amplitude corresponds to a thermal average over the partition function of the system with the imaginary time variable $\tau = 1/T$ determining its temperature. For meson correlators, the QCD currents are given by quark bilinears, $j_\alpha = \bar{q}\Gamma_\alpha q$, where Γ_α specifies the spin-flavor channel (but neither mass nor orbital excitations). The imaginary part of the Fourier transform of the (retarded) correlation function, $G_\alpha^R(\tau, \vec{r})$, is commonly referred to as the spectral function,

$$\rho_\alpha(E, p) = -2 \text{Im} G^R(E, p) , \quad (3)$$

since it represents the physical spectrum in the channel α , which, in principle, can be measured in experiment (E and p are the energy and 3-momentum modulus, respectively, of meson α). Note, however, that in the context of charmonium production in heavy-ion collisions, it is very unlikely that spectral modifications can be directly detected in the dilepton invariant-mass spectrum of J/ψ decays¹. Thus, the relevant connections of the J/ψ 's in-medium spectral properties to heavy-ion collision phenomenology are: (a) its mass which determines the equilibrium abundance, (b) its inelastic width which determines formation and destruction rates (or equilibration times), (c) its dissolution temperature which determines the absence of formation processes, and, (d) its elastic width which affects the 3-momentum spectra.

¹The J/ψ lifetime in free space is about $\tau_{J/\psi}^{\text{vac}} = 1/\Gamma_{J/\psi}^{\text{tot, vac}} \simeq 2000 \text{ fm}/c$, compared to a typical fireball lifetime of $\sim 10 \text{ fm}/c$. This means that the ratio of J/ψ decays inside to outside the medium is about $1/200$. If the average in-medium J/ψ width is $\sim 200 \text{ MeV}$, a detection of this effect would require a mass resolution of about 1 MeV , corresponding to an unrealistic 0.03% at the J/ψ mass.

In the following we discuss equilibrium properties of charmonia (and bottomonia) with focus on modifications in the QGP, starting with lattice QCD (lQCD) results in Sec. 2.1, followed by potential-model approaches (which have recently been developed in close contact with lQCD) in Sec. 2.2 and calculations of inelastic reaction rates (and mass shifts) in the QGP and hadron gas (HG) in Secs. 2.3 and 2.4, respectively. In Sec. 2.5 we elaborate on techniques which have been developed for the fermionic two-body problem in electromagnetic plasmas which shares several common features with in-medium quarkonia and thus might provide useful insights.

2.1 Correlation and Spectral Functions from Lattice QCD

In statistical mechanics, the field-theoretic construction of the thermal partition function involves the transformation of the vacuum transition rate in real time to imaginary time at finite temperature. The temporal direction is thereby restricted to the interval $[0, \beta]$ with the upper limit being identified with the inverse temperature of the system, $\beta = 1/T$. The evaluation of thermal expectation values of correlation functions, Eq. (2), is routinely performed in lQCD. At large r , an exponential decay of the spatial correlator renders the lowest mass state dominant, $G_\alpha(r) \propto e^{-m_\alpha^{scr} r}$, which can be used to extract hadronic screening masses, m_α^{scr} , at finite temperature [24, 25]. For temporal correlators, usually projected onto a fixed 3-momentum, $G(\tau, p)$, the limited extent of the τ interval renders an extraction of physical pole masses much more difficult.

The information on the excitation spectrum in a given hadronic channel is encoded in the spectral function which is related to the temporal correlator via

$$G_\alpha(\tau, p; T) = \int_0^\infty dE \sigma_\alpha(E, p; T) K(E, \tau; T) \quad (4)$$

with the finite- T kernel

$$K(E, \tau; T) = \frac{\cosh[(E(\tau - 1/2T))] }{\sinh[E/2T]} \quad (5)$$

and $\sigma_\alpha = \rho_\alpha/2\pi$. The extraction of the latter thus requires an inverse integral transform, which, on a finite number of points, is, in principle, not unambiguously possible. However, in Ref. [26], it has been suggested to employ the so-called Maximum Entropy Method (MEM) to obtain a probabilistic reconstruction of the most likely spectral functions. Subsequently, this method has been widely used to extract hadronic spectral functions from lQCD correlators [27, 28, 29, 30, 31]. A few examples in various charmonium channels are collected in Fig. 7. The general picture emerging from these calculations is that the ground state S -wave charmonia, i.e., the η_c ($J^P=0^-$) and J/ψ ($J^P=1^-$), are surviving in the QGP up to temperatures of $\sim 2 T_c$, while the P -wave χ_c states ($J^P=0^+, 1^+, 2^+$) dissolve at temperatures slightly above the critical one, $\sim 1.2 T_c$ or so. The first excited S -wave state (ψ'), cannot be resolved numerically, but presumably dissolves earlier than the stronger bound χ_c states, possibly even below T_c . The ψ' should therefore be quite sensitive to modifications in the hadronic phase of a heavy-ion collision. Ground-state bottomonia seem to survive to even higher temperatures, $2.5\text{--}3 T_c$ or more [32, 30].

It is instructive to examine the underlying temporal correlators, examples of which are displayed in Fig. 8 (at vanishing 3-momentum, $p=0$). To facilitate their interpretation, they have been normalized to a so-called reconstructed correlator, which is evaluated with the kernel at temperature T ,

$$G_{\text{rec}}(\tau; T) = \int_0^\infty dE \sigma(E; T^*) K(E, \tau; T) , \quad (6)$$

but employs a spectral function at a low temperature, T^* , where no significant medium effects are expected. The correlator ratio,

$$R_G(\tau, T) = G(\tau; T)/G_{\text{rec}}(\tau; T) , \quad (7)$$

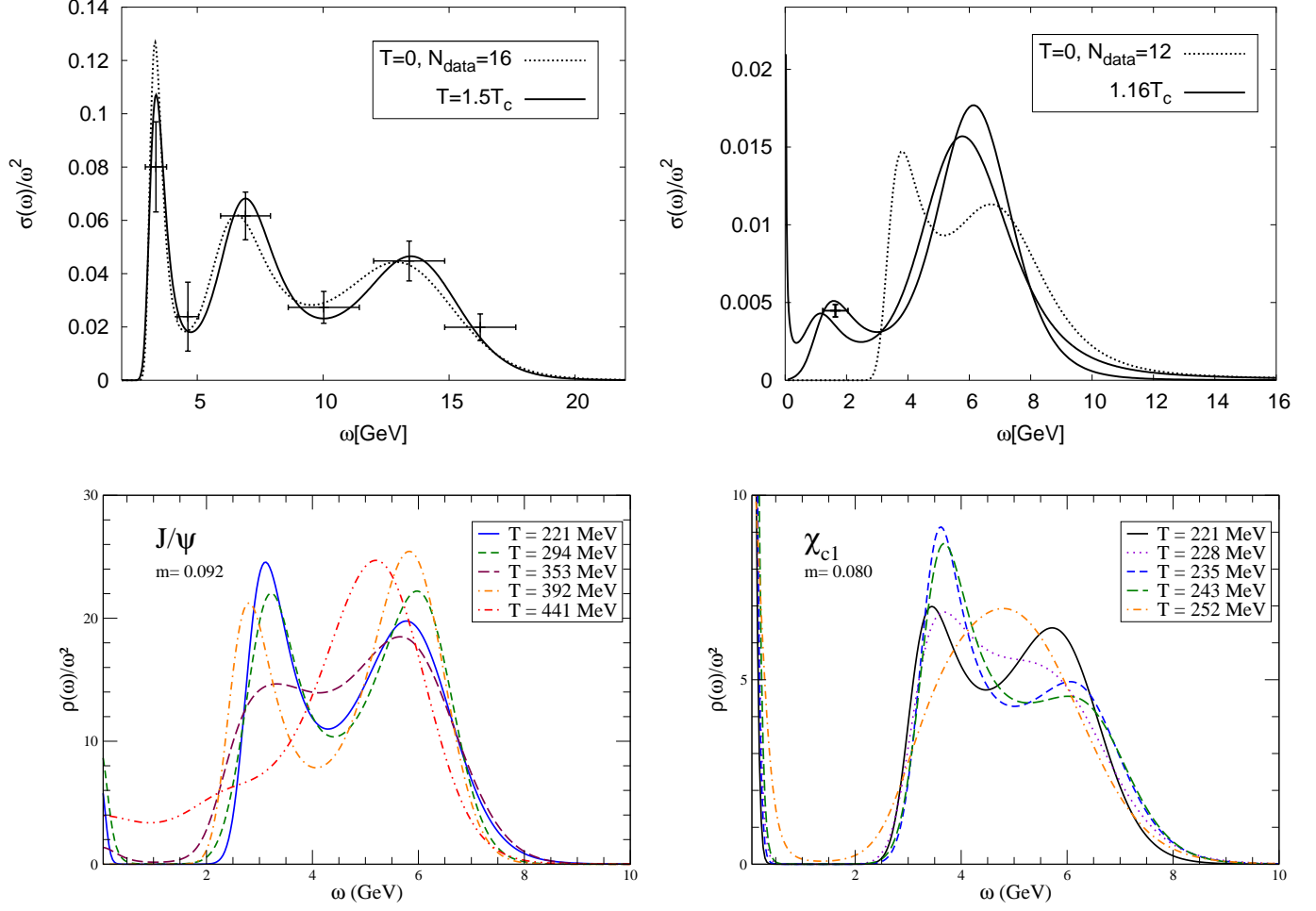


Figure 7: Charmonium spectral functions vs. energy, $\omega \equiv E$, and at vanishing 3-momentum, $p=0$, as evaluated from lQCD correlation functions using the maximum entropy method. Upper panels: η_c (left) and χ_c (right) in quenched QCD, compared to their vacuum spectral functions (dotted lines) [30]; the S -wave (η_c) signal at $1.5 T_c$ is essentially unmodified compared to the vacuum, while the P -wave (χ_c) signal at $1.16 T_c$ is largely distorted (the 2 solid lines in the right panel indicate systematic errors). Lower panels: J/ψ (left) and χ_c (right) computed in full QCD for 2 light flavors [31]; the critical temperature in these simulations is $T_c \simeq 210$ MeV; a J/ψ signal around $E \simeq 3$ GeV survives up to temperatures of at least 392 MeV $\simeq 1.9 T_c$ while the χ_c peak is essentially smeared out at $T=252$ MeV $\simeq 1.2 T_c$.

is then an indicator of medium effects in $G(\tau; T)$ through deviations from 1 (note that a normalization to $G(\tau; T^*)$ is not meaningful due to different τ ranges for T^* and T). In the temporal correlator ratios, the survival of the S -wave charmonia is associated with their relative stability, i.e., small deviations from one, while the variations for the χ_c are much larger and set in much closer to T_c (e.g., up to 40-50% at $T=1.2 T_c$).

Another quantity that can be computed with good accuracy in lQCD, and which encodes valuable information about charmonium properties at zero and finite T (although somewhat indirectly), is the free energy, $F_{Q\bar{Q}}(r)$, of a static pair of heavy quark and antiquark. In fact, as pointed out in Ref. [33], in gluo-dynamics the large distance limit of the free energy, $F_{Q\bar{Q}}^\infty \equiv F_{Q\bar{Q}}(r \rightarrow \infty)$, can be related to the expectation value of the Polyakov loop,

$$e^{-F_{Q\bar{Q}}^\infty/T} = |\langle L \rangle|^2, \quad (8)$$

where L characterizes a heavy-quark (HQ) source whose expectation is zero (finite) in the (de-) confined phase, and thus serves as an order parameter of deconfinement. At zero temperature, the free energy

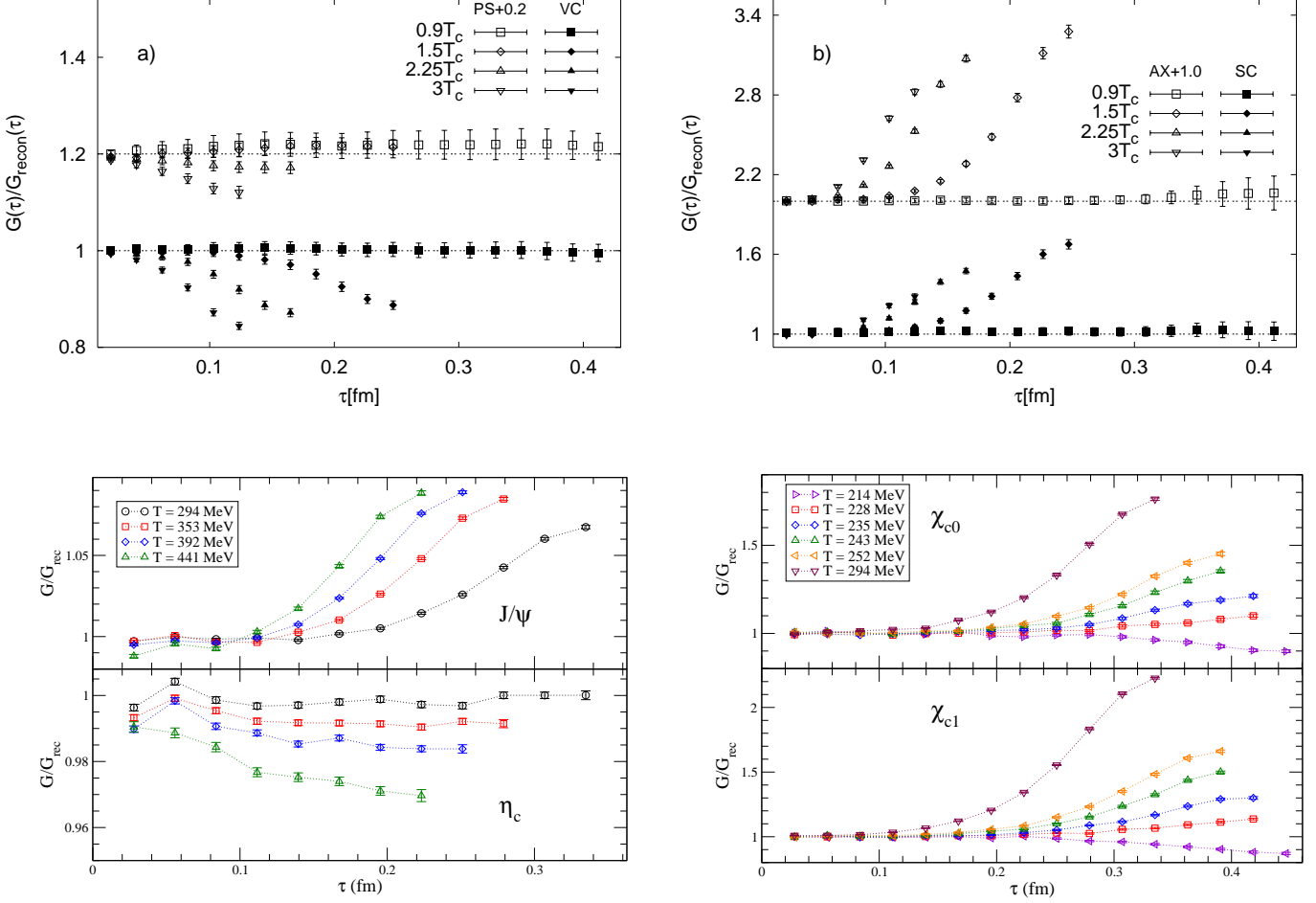


Figure 8: Temporal charmonium correlators at zero 3-momentum computed for J/ψ , η_c (left panels) and χ_{c0} , χ_{c1} (right panels) in quenched (upper panels) [28] and $N_f=2$ (lower panels) [31] lattice QCD. The critical temperature in these simulations is $T_c \simeq 270$ MeV and 210 MeV, respectively. Note the comparatively small variations in the S -waves (left panels), and the rather large increase in the P -waves (right panels) indicative for additional low-energy strength relative to the reconstructed correlator.

computed in the color-singlet channel closely follows the form expected for a phenomenological Cornell-type potential [34, 35, 36], consisting of a color-Coulomb and a linearly confining term,

$$F_{\bar{Q}Q}^{(1)}(r; T=0) = -\frac{4}{3} \frac{\alpha_s}{r} + \sigma r, \quad (9)$$

where σ denotes the string tension. This finding, in connection with the development of HQ effective theories, has confirmed a posteriori the suitability of potential models to quantitatively compute charmonium and bottomonium spectroscopy in free space based on first principles [35]. In the presence of light quarks, string breaking occurs, being characterized by $F_{\bar{Q}Q}^{(1)}(r; T=0)$ leveling off at a finite value even in vacuum. This may be interpreted as an effective quark or D -meson mass according to $m_D = m_c^0 + F_{\bar{Q}Q,\infty}^{(1)}/2$ (where $m_c^0 \simeq 1.2$ GeV is the bare quark mass); numerically, with a typical string-breaking separation of $r_{\text{sb}} \simeq 1.2$ fm, one finds $V_{\bar{Q}Q}^{(1)}(r_{\text{sb}}) \simeq 1.2$ GeV, which roughly recovers the empirical D -meson mass. At finite temperature, lQCD computations for $F_{\bar{Q}Q}^{(1)}(r; T)$ find the expected color-Debye screening, which gradually penetrates to smaller distances as the temperature increases, cf. left panel of Fig. 9. However, the implications for HQ bound states (or spectral functions) are quite subtle. First, at finite T the free energy receives an extra contribution due to an entropy term,

$$F_{\bar{Q}Q}(r; T) = U_{\bar{Q}Q}(r; T) - TS_{\bar{Q}Q}(r; T), \quad (10)$$

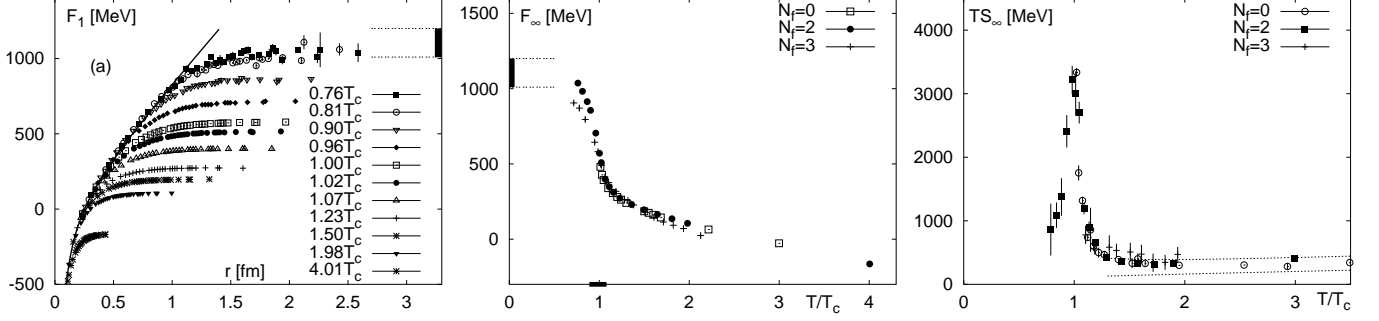


Figure 9: Left panel: free energy of a color-singlet heavy quark-antiquark pair as a function of its size for various temperatures as computed in $N_f=2$ lattice QCD [36]; the vertical bar in the upper left part indicates the estimated string-breaking energy, $V_{\bar{Q}Q}^{(1)}(r_{\text{sb}}) \simeq 1.2$ GeV, in vacuum. Middle panel: temperature dependence of the asymptotic value, $F(r \rightarrow \infty; T)$, of the color-averaged free energy in quenched ($N_f=0$) [37], $N_f=2$ [36] and $N_f=3$ [38] lQCD; the pertinent critical temperatures are $T_c=270$, 200 and 193 MeV, respectively. Right panel: entropy contribution to the color-averaged free energy at asymptotically large quark-antiquark separation corresponding to the free energies of the middle panel. The band enclosed by the dotted lines for $T \geq 1.3T_c$ indicates a perturbative estimate of $TS_{\bar{Q}Q}^\infty$.

and it is currently not clear whether the internal energy, $U_{\bar{Q}Q}(r; T)$, or the free one, $F_{\bar{Q}Q}(r; T)$, is the more appropriate quantity to be identified with a finite-temperature HQ potential. Second, the temperature introduces an extra scale into the problem which needs to be properly implemented into the construction of a HQ effective theory (cf. Ref. [39] for recent progress). Third, the presence of the entropy term, which does not vanish at large separation r , renders the identification of an effective HQ mass more problematic, especially close to T_c , where $TS_{\bar{Q}Q}^\infty$ becomes very large, see right panel of Fig. 9. Notwithstanding these obstacles, the application of potential models at finite temperature has provided valuable insights into heavy quarkonium properties at finite T . In particular, the synthesis of the now available, independent information on correlators and free energies from lQCD has enabled interesting insights, as we discuss in the following Section.

2.2 Potential Models in the QGP

Early applications [40] of heavy-quark potentials in the medium have employed a phenomenological ansatz for a screened version of the Cornell potential,

$$V(r; T) = \frac{\sigma}{\mu_D(T)} \left(1 - e^{-\mu_D(T)r}\right) - \frac{\alpha}{r} e^{-\mu_D(T)r} \quad (11)$$

where the temperature dependence is encoded in the Debye mass, $\mu_D(T)$ (the vacuum potential is recovered for $\mu_D \rightarrow 0$, with parameters fitting the vacuum charmonium spectroscopy, $\sigma \simeq 1$ GeV/fm and $\alpha_s \simeq 0.35$). Defining the Hamiltonian as

$$\hat{H}(r; T) = 2m_Q + \frac{\vec{\nabla}^2}{m_Q} + V(r; T) , \quad (12)$$

the Schrödinger equation for the bound state problem,

$$\hat{H} \phi_{nl}(r; \mu_D) = E_{nl}(\mu_D) \phi_{nl}(r; \mu_D) , \quad (13)$$

has been solved for the eigen-energies, E_{nl} , as a function of the Debye mass. A state (n, l) was considered to be dissolved at a critical Debye mass, μ_D^c , if the “dissociation” energy,

$$E_{nl}^{\text{diss}} \equiv 2m_Q + \frac{\sigma}{\mu_D} - E_{nl} \quad (14)$$

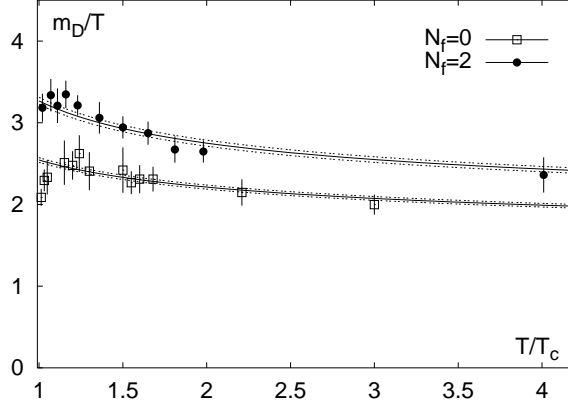


Figure 10: Nonperturbative extraction of the Debye mass based on exponential fits of a screened Coulombic term to the in-medium color-singlet HQ free energy in $N_f=2$ (solid circles) [36] and pure gauge ($N_f=0$, open squares) [41] lQCD. The bands are analytic fits using the perturbative form of the Debye mass, $\mu_D/T = A(1 + N_f/6)^{1/2} g_{2\text{-loop}}$ with a 2-loop finite- T running coupling and a multiplicative constant $A \simeq 1.5$ to account for nonperturbative effects. Absolute units are obtained by using the pertinent critical temperatures of $T_c \simeq 200(270)$ MeV for $N_f=2(0)$.

reaches zero. Note that the term $\frac{\sigma}{\mu_D}$ corresponds to the large-separation limit of the potential, cf. the discussion following Eq. (9) in the previous Section. The critical Debye masses for dissolution were found to be $\mu_D^c(n=1) \simeq 0.7(1.6)$ GeV for ground state charmonium (bottomonium), and $\mu_D^c(n=2) \simeq 0.35(0.6)$ GeV for the first excited states, ψ' and χ_c (Υ' and χ_b) [40]. Recent lQCD computations of the in-medium Debye mass based on the Coulombic term in the color-singlet free energy are displayed in Fig. 10 [36]. Comparing these to the values for μ_D^c extracted from the in-medium Cornell potential, Eq. (11), suggests dissociation temperatures of all charmonia at or slightly above T_c .

The next step became possible with the availability of quantitative lQCD results for heavy-quark free energies. In Ref. [42], the color-singlet free energy, $F_{\bar{Q}Q}^{(1)}$ was used in a Schrödinger equation, and the J/ψ dissolution temperature was found at about $1.1 T_c$, while χ_c (ψ') were found to melt (well) below T_c . The recent lQCD spectral function results, indicative for J/ψ states surviving well above T_c , appear to challenge this conclusion (recall Fig. 7). In Ref. [43] it has been suggested to employ the internal, rather than the free, energy as an interquark potential. It was argued that $U_{\bar{Q}Q}$ is the appropriate quantity in the limit where the typical bound state (formation or life) time is much smaller than the typical time for heat exchange with the environment, $\tau_{\text{bound}} \ll \tau_{\text{heat}}$. In this case, the entropy term is not active and should be removed from the free energy, leading to the internal energy. While on first sight, according to Eq. (10), $U_{\bar{Q}Q} > F_{\bar{Q}Q}$, the actually used potentials become deeper upon subtraction of the asymptotic values of the internal energy. As noted in the previous Section in connection with Fig. 9, this procedure is problematic in the immediate vicinity of T_c , but appears to be more reasonable for $T \geq 1.1 T_c$. This problem is currently the weakest link in converting lQCD results to effective heavy-quark potentials. From a pragmatic point of view, the use of $U_{\bar{Q}Q}$ in a Schrödinger equation [43, 44, 45] improved the qualitative agreement of the potential approach with the lQCD spectral functions in that J/ψ bound states are supported up to temperatures of $\sim 2\text{--}2.5 T_c$, while the χ_c dissolves at around $1.1\text{--}1.2 T_c$. In Ref. [46], the internal energies have been implemented into a T -matrix approach for $Q\text{--}\bar{Q}$ (and $q\text{--}\bar{q}$) interactions, which has the important advantage over the Schrödinger equation that it provides a unified description of bound and scattering states (i.e., above the nominal $Q\text{--}\bar{Q}$ threshold). For S -wave charmonia, it was found that the lowest bound state moves into the continuum at $\sim 2 T_c$, after which it rapidly dissolves. However, it was also noted that the extractions of the internal energy from different

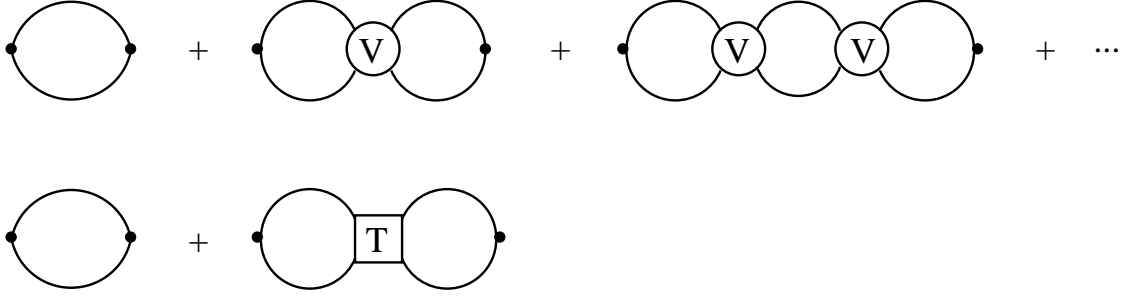


Figure 11: Diagrammatic representation of the $Q\bar{Q}$ correlation function as obtained from resumming the HQ potential (upper panel) resulting in a folding with the T -matrix (lower panel) corresponding to Eq. (17). The solid dots represent operators projecting into different mesonic channels; figure taken from Ref. [50].

lQCD calculations are not unique, thus adding to the uncertainty in the potential definition.

Model comparisons to lattice QCD “data” can be made more quantitative by computing the pertinent spectral functions, $\rho_\alpha(E)$ within a given approach (see, e.g., Ref. [47] for an early application in the light quark sector): the integral in Eq. (4) can then be straightforwardly carried out and compared to accurate lQCD results for Euclidean correlation functions. The first comparison of finite- T potential models with lQCD correlation functions for charmonia has been conducted in Ref. [48]. For the bound-state part a Schrödinger equation was solved using a screened Cornell potential, Eq. (11), as well as lQCD internal energies, with fixed heavy-quark masses, while the continuum was modeled by a non-interacting perturbative form,

$$\sigma_\alpha(E; T) = \sum_i 2M_i F_i^2 \delta(E^2 - M_i^2) + \frac{3}{8\pi^2} E^2 \Theta(E - s_0) f_\alpha(E, s_0) , \quad (15)$$

with a temperature dependent threshold $s_0 = s_0(T)$ and coefficients f_α depending on the meson channel α . While some trends of the lattice correlators were reproduced, a comprehensive agreement could not be achieved; similar results have been obtained in Ref. [49]. In Ref. [50] the T -matrix approach introduced in Ref. [46] has been further developed for a systematic analysis of heavy quarkonium correlators. Starting from the covariant Bethe-Salpeter equation for two-body scattering, one can apply standard reduction schemes to obtain the 3-dimensional Lippmann-Schwinger equation. After a partial-wave expansion, the latter becomes a 1-dimensional integral equation for the T -matrix which for vanishing total 3-momentum ($p=0$) takes the form

$$T_l(E; q', q) = V_l(q', q) + \frac{2}{\pi} \int_0^\infty dk k^2 V_l(q', k) G_{\bar{Q}Q}(E; k) T_l(E; k, q) \hat{f}^Q(\omega_k) ; \quad (16)$$

here, $G_{\bar{Q}Q}(E, k)$ denotes the intermediate heavy quark-antiquark propagator, $\hat{f}^Q = 1 - f^Q - f^{\bar{Q}}$ with $f^{Q, \bar{Q}}$ HQ Fermi distributions, and q, q', k are the (off-shell) 3-momenta of the quarks in the initial, final and intermediate state. The in-medium T -matrix equation can be derived from a finite-temperature Green’s function approach [51] and constitutes a consistent many-body framework to compute in-medium 1- and 2-particle correlations (it has been widely applied, e.g., in nuclear many-body theory [52], as well as in the analysis of electromagnetic plasmas, as will be discussed in Sec. 2.5). It is particularly suited for the problem at hand since the potentials can be directly identified with the ones extracted from the lattice (after Fourier transformation and partial-wave expansion with angular-momentum quantum number l). It treats bound and scattering states on the same footing, which is mandatory for situations where bound states gradually dissolve into a continuum. At the same time, rescattering effects in the continuum, including possible resonance formation, are accounted for by a full resummation of the

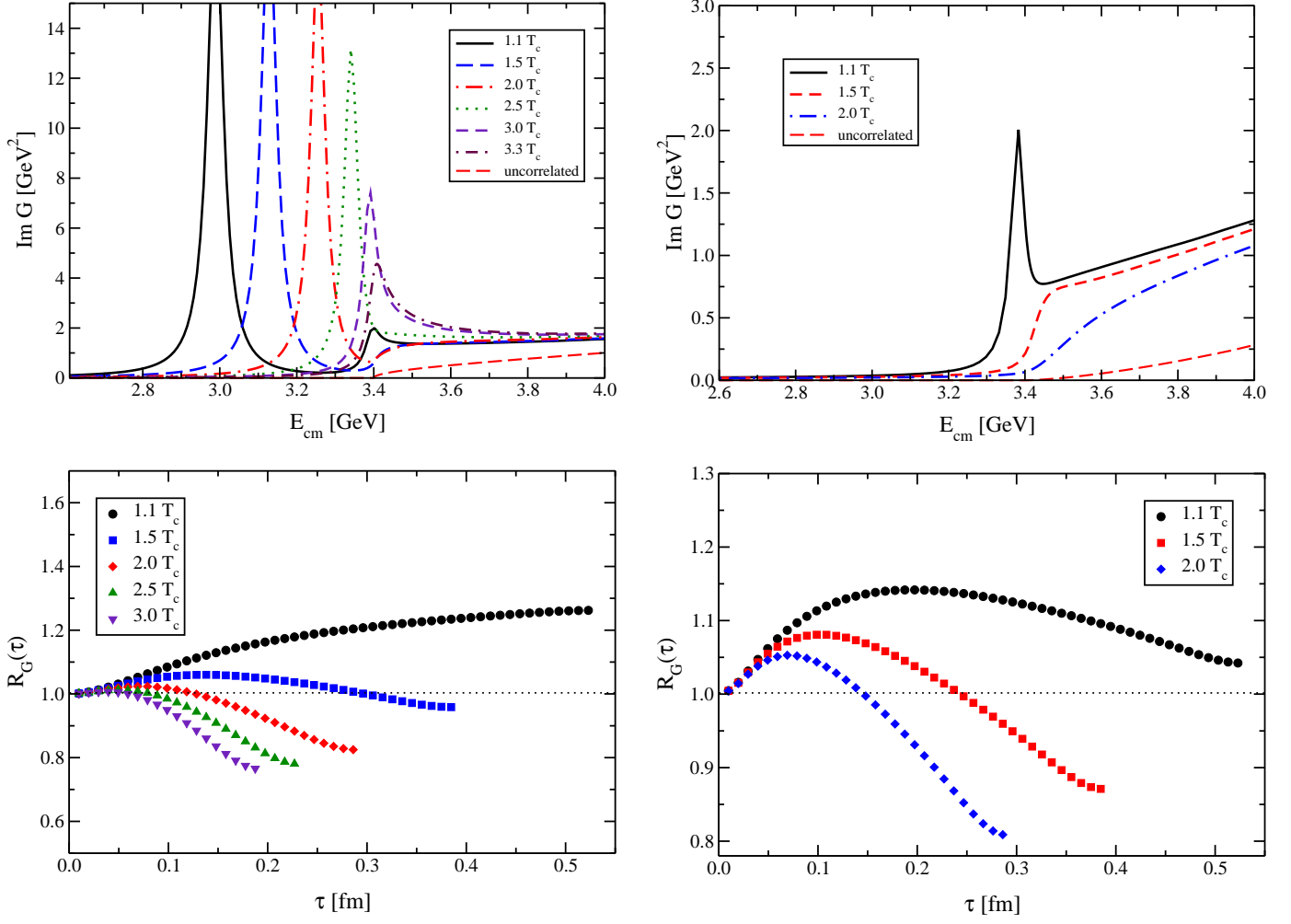


Figure 12: Charmonium spectral functions as a function of energy, $E_{\text{cm}} \equiv E$ (upper panels) and pertinent Euclidean-time (τ) correlator ratios (lower panels, using the calculated vacuum spectral function for the reconstructed correlator) computed in the T -matrix approach of Ref. [50]. The left panels represent S -wave states (J/ψ , η_c) while the right ones correspond to P -waves (χ_{c0} , χ_{c1}). The charm-quark mass has been fixed at $m_c = 1.7$ GeV, while a small width of 20 MeV has been introduced in the Q and \bar{Q} propagator for better display of the bound state regime.

potential, without the need for matching procedures. Furthermore, the 2-particle propagator allows for well-defined implementation of medium effects on the heavy quarks via (complex) single-particle selfenergies encoding mass changes (real part) and finite widths (imaginary part). Charmonia widths are important for phenomenological applications in heavy-ion reactions and thus are an essential ingredient to correlator analyses. The T -matrix is directly related to the correlation function in momentum space by a double folding over external vertices, schematically given by

$$G = G^0 + G^0 T G^0 \equiv G^0 + \Delta G, \quad (17)$$

and illustrated in Fig. 11. Performing a partial wave expansion and keeping the leading terms in $1/m_Q$ the explicit form of the correlator becomes

$$G_l^0(E) = \frac{2N_c}{\pi} \int k^2 dk a_l(k, k) G_{Q\bar{Q}}(E; k) \hat{f}^Q(\omega_k) \quad (18)$$

$$\Delta G_l(E) = \frac{N_c}{\pi^3} \int k^2 dk G_{Q\bar{Q}}(E; k) \hat{f}^Q(\omega_k) \int k'^2 dk' G_{Q\bar{Q}}(E; k') \hat{f}^Q(\omega_{k'}) a_l(k, k') T_l(E, k, k'), \quad (19)$$

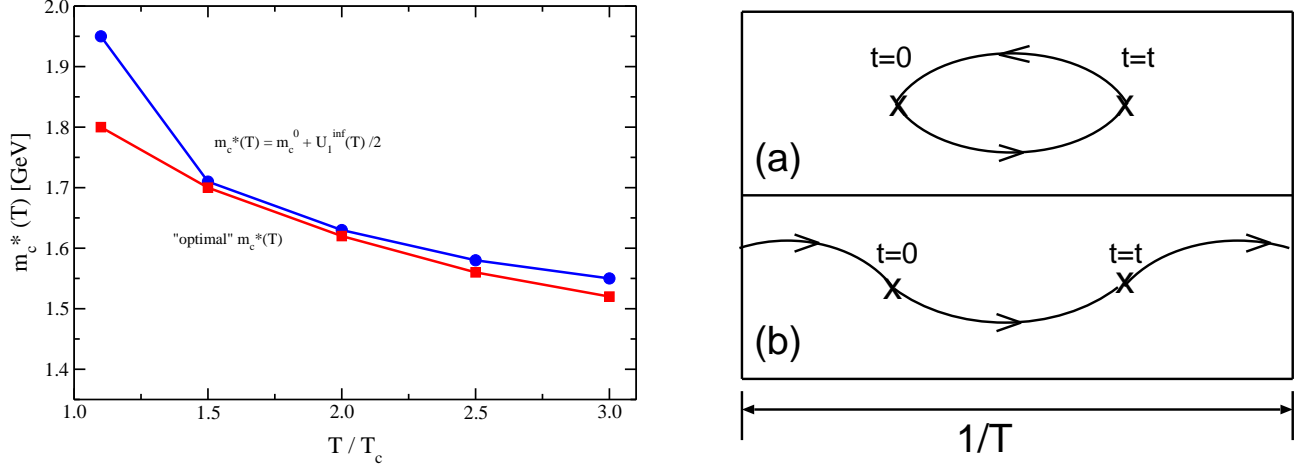


Figure 13: Two effects relevant to quarkonium correlators. Left panel: in-medium charm-quark mass following from the asymptotic value of the internal energy (upper curve) [38, 50] and as inferred from a “fit” to the η_c correlator [56] as shown in the upper right of Fig. 15. Right panel: contributions to temporal correlation function computed in finite-temperature lattice QCD [54]. In addition to the standard mesonic point-to-point correlator (upper panel), the periodic boundary conditions in τ direction allow for the presence of a quark scattering diagram (lower panel).

with coefficients $a_{0,1}(k, k') = 2, 2kk'/m_Q^2$ in the S - and P -wave channels, respectively. The imaginary part of the correlator is just the spectral function (up to a constant factor). To leading order in $1/m_Q$, HQ spin symmetry implies degeneracy of different spin states within a partial wave (i.e., for S -waves η_s and J/ψ , as well as for the P -wave χ_c states). Results of the T -matrix approach for spectral and correlation functions are shown in Fig. 12 for a constant c -quark mass ($m_c = 1.7$ GeV) and a small width (~ 20 MeV) in the quark propagators. For the potential the (subtracted) $N_f = 3$ internal energy of Ref. [38] has been employed; the J/ψ (or η_c) is found to dissolve around $\sim 3 T_c$ ($\sim 2.5 T_c$ when using the internal energy of Ref. [53]), while the χ_c states melt at a much lower temperature of $\sim 1.3 T_c$. We note that these values should be considered as upper limits, since larger finite widths will lead to a melting at smaller temperatures. The continuum part of the spectral functions in both S - and P -waves exhibits a large enhancement over the non-interacting case; this effect cannot be neglected in quantitative applications to correlation functions. While the pertinent temporal correlator ratios in the S -wave are roughly reminiscent to the ones in lQCD, the P -waves are quite different in both magnitude and temperature dependence, cf. Fig. 8. In particular, the decreasing trend at large τ indicates that the spectral functions are increasingly missing low-energy strength with increasing temperature. In the η_c channel, this problem is largely overcome when the in-medium charm-quark mass, as following from the asymptotic value of the internal energy, is included, i.e., $m_c^*(T) = m_c^0 + U_\infty^{(1)}(T)/2$, cf. the left panel of Fig. 13. While this stabilizes the η_c correlator ratio [50], it is not enough to quantitatively improve on the agreement with the lQCD J/ψ and χ_c correlators. An essential part of this puzzle has been identified in Ref. [54], in terms of an energy-independent contribution to the correlators which arises due to the periodic boundary conditions in the (finite) τ direction at finite temperature. This term may be interpreted as a scattering contribution which generates a low-energy peak in the spectral functions that can be related to susceptibility term in the lattice QCD correlators [55]. These contributions have been readily implemented into potential model analyses and are found to largely resolve the discrepancies with the lQCD correlators [57, 58, 56]. However, significant discrepancies between the model approaches and their respective conclusions remain. In Ref. [57], a screened Cornell potential implemented into a nonrelativistic Green’s function approach which has been supplemented by, and

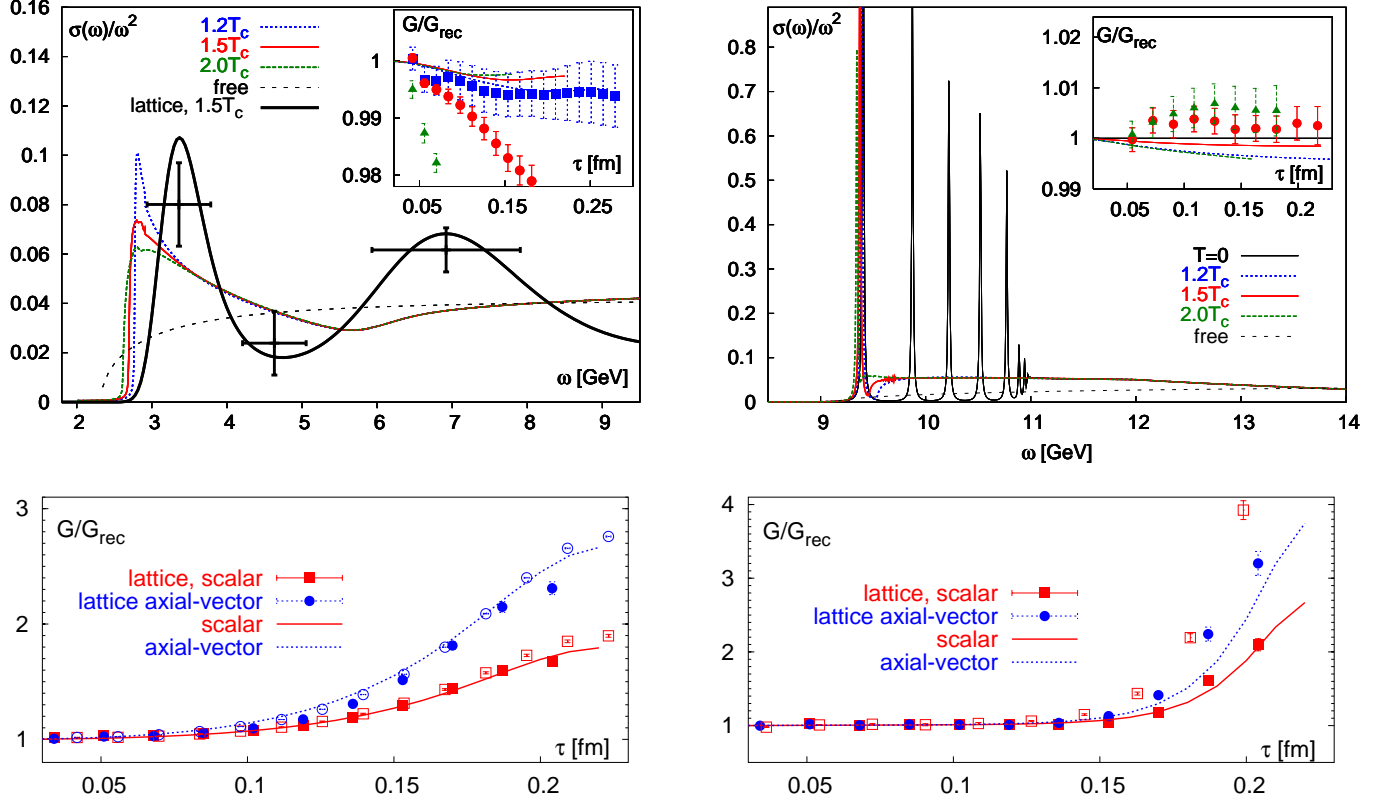


Figure 14: Charmonium and bottomonium spectral and correlation functions in a Gluon Plasma in the potential model of Ref. [57], supplemented with a perturbative QCD continuum (with K factor at high energies). Upper panels: spectral and correlation functions (insets) for S -wave charmonium (η_c , left) and bottomonium (η_b , right) at various temperatures; the lattice results are for quenched QCD [30]. Lower panels: Euclidean correlator ratios for P -wave charmonia (left) and bottomonia (right) at $1.5 T_c$; closed and open symbols are quenched lQCD results from Refs. [30, 28, 59].

matched to, a perturbative continuum at high energies including a K factor. The S -wave charmonium and bottomonium spectral functions show appreciable modifications with temperature, cf. upper panels in Fig. 14. Even though the η_c state melts at a temperature as low as $T \simeq 1.3T_c$ the corresponding S -wave correlator changes little with temperature. It was therefore concluded that the lQCD correlators are consistent with a melting of all charmonium states at temperatures below $1.3 T_c$. Essential to this argument is a strong reduction of the in-medium charm-anticharm quark threshold to $2m_c \simeq 2.7$ GeV together with a nonperturbative threshold enhancement in the spectral function, as first emphasized in the T -matrix approach of Ref. [50]. In Ref. [58] the in-medium HQ potential was taken as a linear combination of $F^{(1)}$ and $U^{(1)}$ (as advocated in Ref. [60]), in connection with a constant HQ mass and a noninteracting perturbative continuum, corresponding to a spectral function as in Eq. (15). Here, the (semi-) quantitative description of the lQCD correlators (see left panels of Fig. 15) goes along with a J/ψ melting at $\sim 1.6 T_c$. The right panels of Fig. 15 depict S - and P -wave charmonium correlator ratios within the T -matrix approach based on the spectral functions in the upper panels of Fig. 12, where the HQ potential is taken as the (subtracted) internal energy. The in-medium charm-quark mass has been calculated including the asymptotic value of the internal energy, $m_c^0 + U_\infty^{(1)}(T)/2$ (except for close to T_c where the large entropy contribution, $TS_\infty^{(1)}$ is problematic, cf. Fig. 13). As in Refs. [57, 58], a (semi-) quantitative reproduction of the lQCD correlator ratios emerges, only that in this approach the dissolution temperature of the J/ψ is now close to $3 T_c$. While the pseudoscalar (η_Q) correlators appear to be free of the zero-mode (scattering) contributions (also the J/ψ seems to be only mildly affected),

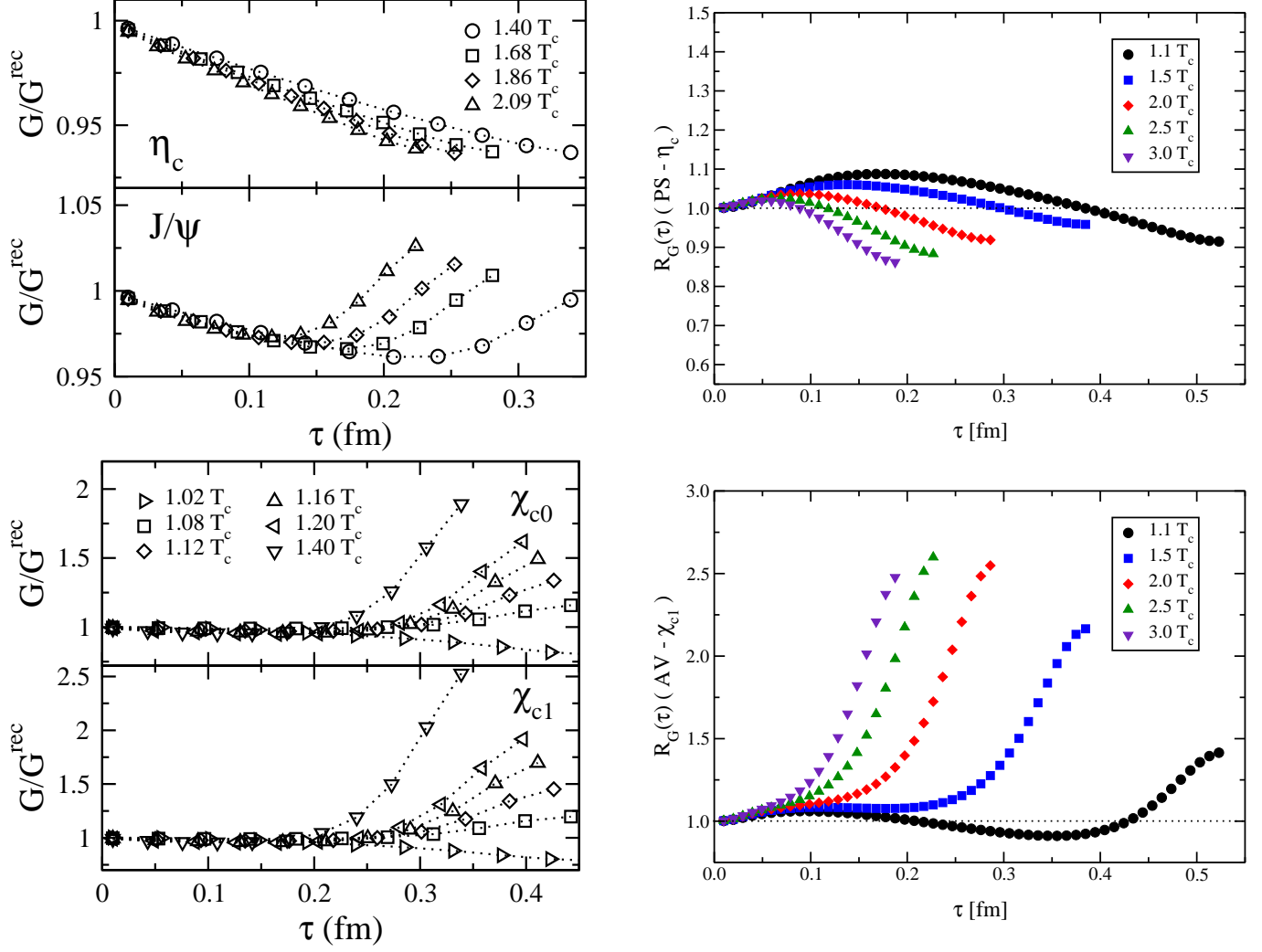


Figure 15: Temporal charmonium correlator ratios in above T_c , including zero-mode contributions. Left panels: S - and P -waves (upper and lower left, respectively) in the Schrödinger-equation approach of Ref. [58] based on a combination [60] of free and internal energy as HQ potential. Right panels: η_{c0} and χ_{c1} (upper and lower right, respectively) in the T -matrix approach of Refs. [50, 56] (using the calculated vacuum spectral function for the reconstructed correlator and including an in-medium charm-quark mass according to the left panel of Fig. 13).

the P -wave correlators in the QGP are modified appreciably. The extra low-energy strength in the spectral functions may be approximated by an extra term $\sim \chi_\alpha E \delta(E)$. When implementing these into the correlation functions and evaluating the susceptibilities, χ_α , for a free gas, the description of the P -wave correlators is much improved [57, 58, 56] (see lower panels in Figs. 14 and 15) compared to the lQCD results displayed in Fig. 8.

The current status of potential model approaches to lQCD correlators is thus not yet conclusive. In particular, a quantitative determination of the in-medium HQ mass will be important to make further progress. Another ingredient that has not received much attention in the context of correlators is the (inelastic) width of the charmonium spectral function, which is a very relevant quantity for heavy-ion phenomenology. This is the topic of the following Section.

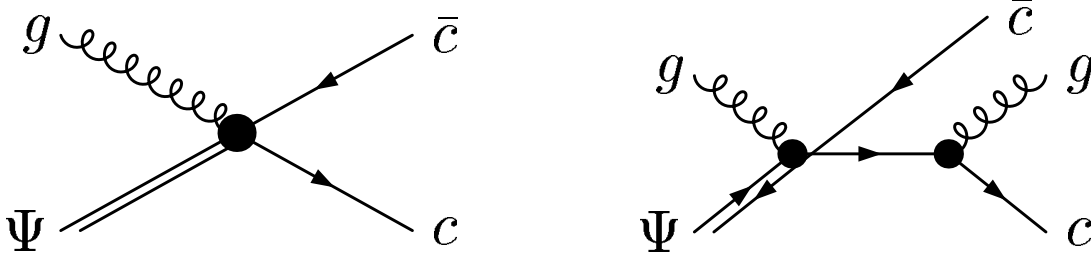


Figure 16: Charmonium dissociation reactions via parton impact; left panel: gluon-dissociation [61, 62] representing the leading-order QCD process; right panel: quasifree dissociation [23] representing a next-to-leading order process.

2.3 Charmonium Dissociation Reactions in the QGP

The survival of a charmonium (bound or resonance) state in the QGP does not imply that it is protected from suppression, since it can be dissociated by inelastic collisions with the surrounding partons. By detailed balance the inverse of these reactions is operative in charmonium formation, and therefore the pertinent inelastic width, $\Gamma_\Psi = (\tau_\Psi)^{-1}$, is directly related to the relaxation time, τ_Ψ , of the charmonium abundance toward its thermal equilibrium number, N_Ψ^{eq} . This is immediately borne out of the pertinent kinetic rate equation for the time evolution of the charmonium number $N_\Psi(\tau)$, which for a spatially homogeneous system takes the simple form

$$\frac{dN_\Psi}{d\tau} = -\Gamma_\Psi(N_\Psi - N_\Psi^{\text{eq}}) \quad (20)$$

(its solutions in a thermal fireball background suitable for heavy-ion collisions will be discussed in detail in Sec. 3.1 below). In general, the dissociation of a composite particle in a medium can be classified into the following processes: (1) direct decays, $\Psi \rightarrow c + \bar{c}$ (or $\Psi \rightarrow c + \bar{c} + g$), (2) inelastic collisions with partons, most notably (2i) $\Psi + g \rightarrow c + \bar{c}$ (cf. left panel in Fig. 16), or (2ii) $\Psi + i \rightarrow c + \bar{c} + i$, with $i = g, q, \bar{q}$ (cf. right panel in Fig. 16). Note that the distinction between a bound and a resonance state from the point of view of the rate equation (20) is immaterial; it matters, however, for quantitative assessments of the dominant contributions to the inelastic width. E.g., if a Ψ state moves into the continuum, i.e., above the $c\bar{c}$ threshold at a certain temperature, the opening of the direct decay usually renders it the dominant process. In this sense the dissolution of a state due to screening corresponds to the $\Gamma_\Psi \rightarrow \infty$ limit of direct decays. The potential-model calculations discussed in the previous section indeed suggest that once a charmonium state becomes unbound, resonance states can no longer be supported. On the other hand, for binding energies of the order of 100 MeV, inelastic widths of a similar magnitude could induce a “premature” melting of the state (the dissociation temperature quoted above are therefore to be considered as upper limits).

A standard approach to compute inelastic reaction rates in a thermal medium is to first calculate the cross section for a given dissociation reaction and fold it over the thermal distribution of the (on-shell) medium particles,

$$\Gamma_\Psi = \int \frac{d^3k}{(2\pi)^3} f^{q,g}(\omega_k, T) v_{\text{rel}} \sigma_\Psi^{\text{diss}}(s) \quad (21)$$

(v_{rel} : relative velocity of the incoming particles in the center of mass of the collision; $s = (p + k)^2$: center-of-mass energy squared of the parton- Ψ collision). The cross section for gluon dissociation, $g + J/\psi \rightarrow c + \bar{c}$, has first been evaluated in Refs. [61, 62], using hydrogen-like wave functions (this is expected to be a good approximation as long as the Coulombic part of the Cornell potential dominates the $Q\bar{Q}$ bound-state properties; as noted in Refs. [61, 62] this approximation is, strictly speaking, not

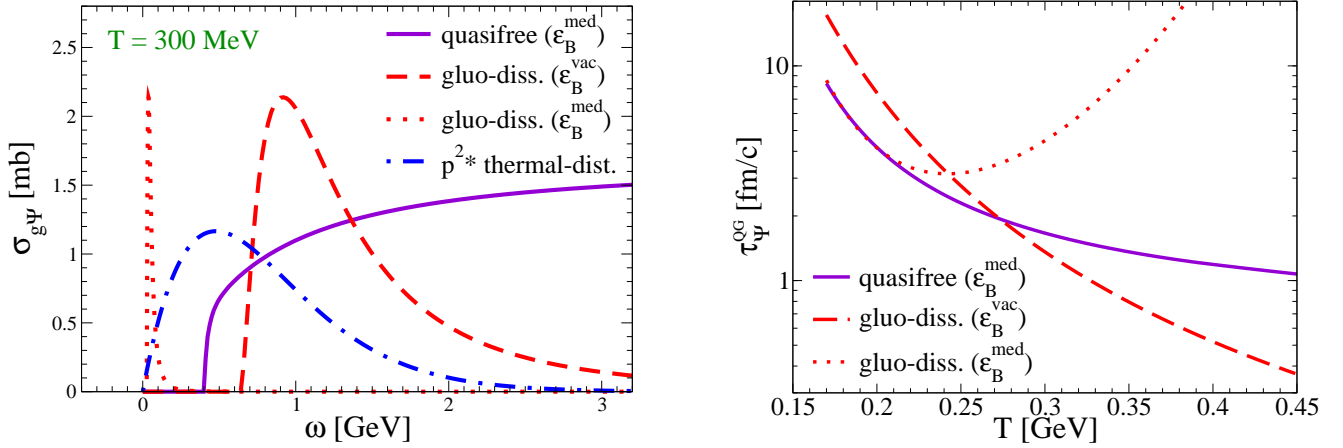


Figure 17: Total cross sections (left panel) and pertinent dissociation times (right panel) for J/ψ dissociation reactions in the QGP: gluo-dissociation, $g + J/\psi \rightarrow c + \bar{c}$, according to Eq. (22) with vacuum ($\epsilon_B=640$ MeV, dashed line) and in-medium ($\epsilon_B \simeq 30$ MeV, dotted line) binding energies (the pertinent phase distribution, $p^2 f^B(p; T)$, for massless gluons is illustrated by the dash-dotted line); parton-induced quasifree dissociation, $i + J/\psi \rightarrow c + \bar{c} + i$, using an in-medium binding energy, $\mu_D = gT$ and thermal parton masses $m_i \propto gT$ [23, 65].

(marginally) satisfied for the J/ψ (Υ) with vacuum binding energies of $\sim 0.6(1.0)$ GeV). For massless gluons of energy ω incident on a ground-state quarkonium one finds

$$\begin{aligned} \sigma_{g\psi}(\omega) &= \frac{2\pi}{3} \left(\frac{32}{3}\right)^2 \left(\frac{m_Q}{\epsilon_B}\right)^{1/2} \frac{1}{m_Q^2} \frac{(\omega/\epsilon_B - 1)^{3/2}}{(\omega/\epsilon_B)^5} \\ &= 2\pi \left(\frac{16}{3}\right)^2 \alpha_s a_0^2 \frac{(\omega/\epsilon_B - 1)^{3/2}}{(\omega/\epsilon_B)^5}, \end{aligned} \quad (22)$$

where ϵ_B denotes the quarkonium binding energy and m_Q the effective heavy-quark mass. The second line has been obtained by using the Coulomb-potential expressions for binding energy, $\epsilon_B = (\frac{3}{4}\alpha_s)^2 m_Q$, and Bohr radius, $a_0 = 4/(3\alpha_s m_Q)$, and illustrates the leading-order (LO) character ($\mathcal{O}(\alpha_s)$) character of the cross section, being proportional to the “geometric” size of the bound state. The cross section has a threshold at $\omega_{\text{thr}} = \epsilon_B$ and acquires its maximum at $\omega_{\text{max}} = \frac{7}{5}\epsilon_B$, cf. right panel of Fig. 17. For QGP temperatures of 200-300 MeV, typical for SPS and RHIC energies, the average thermal gluon energy of $3T$ amounts to 600-900 MeV, providing good overlap with the vacuum gluo-dissociation cross section and resulting in dissociation rates of $\Gamma_{J/\psi} \simeq 30 - 200$ MeV, see left panel of Fig. 17. However, if the binding energy decreases with temperature, the available phase space of the gluon dissociation shrinks substantially. E.g., in the screened potential model of Ref. [40], corresponding to Eq. (11), a moderate screening mass of $\mu_D \simeq gT$ with $\alpha_s \simeq 0.25$ ($g \simeq 1.75$), yields a J/ψ binding energy of only about 200(30) MeV at $T=180(300)$ MeV, reaching zero at around 360 MeV. As a consequence, the gluo-dissociation rate decreases with increasing temperature for $T \geq 250$ MeV, cf. dotted line in the left panel of Fig. 17, which is obviously a rather unphysical behavior (see also Refs. [44, 63, 64]). For the same reason, the gluo-dissociation process cannot provide a realistic description for the dissociation of excited charmonia whose binding energies are small even in the vacuum.

An early nonperturbative approach to compute heavy quarkonium break-up from quark impact (corresponding to the category (2ii) of the above classification) has been suggested in Ref. [66] in analogy to electron-induced atom ionization; the pertinent effective “thermal activation” cross section,

$$\sigma(T) = \pi r_{Q\bar{Q}}^2 e^{-E_{\text{diss}}/T}, \quad (23)$$

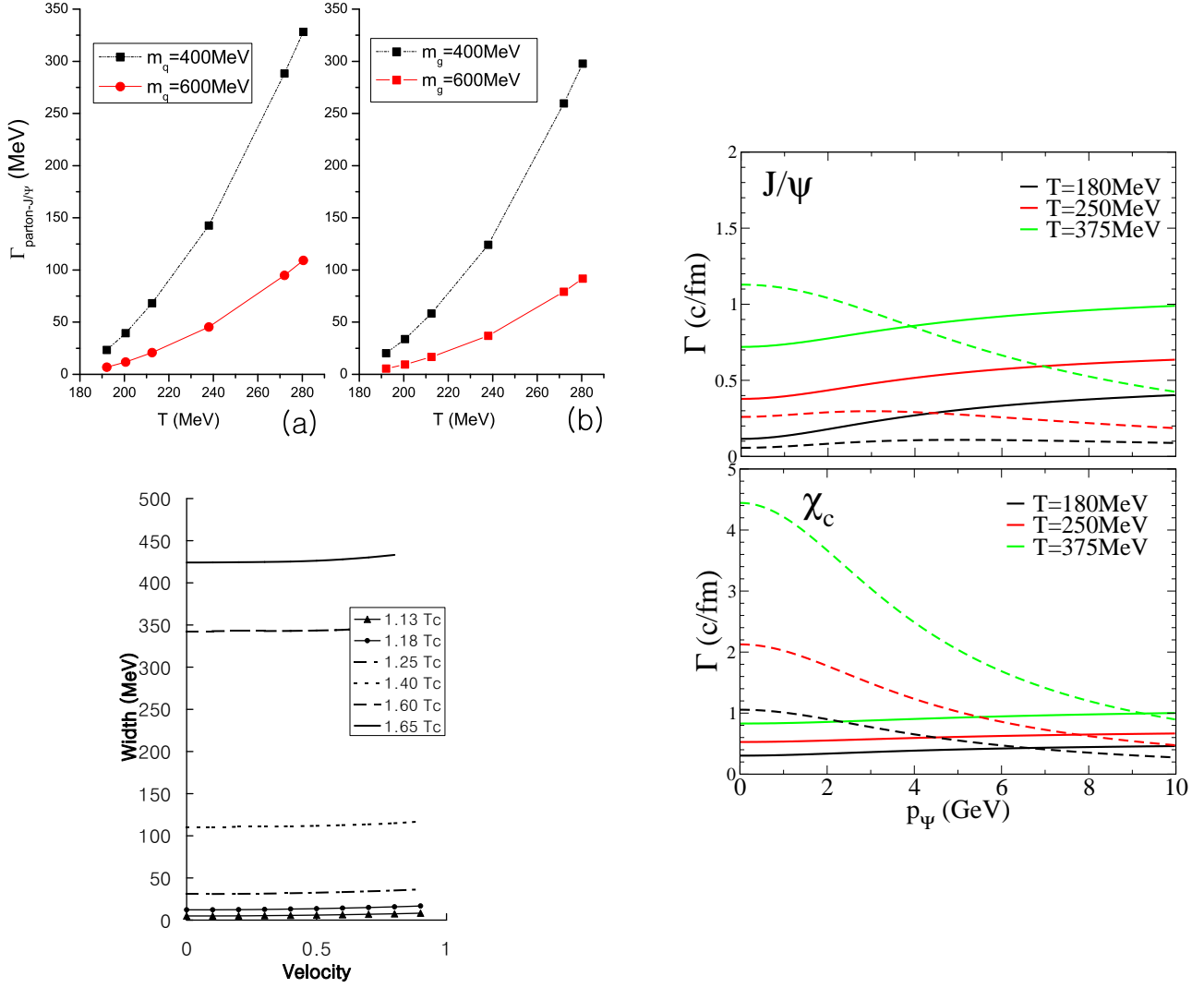


Figure 18: Parton-induced J/ψ dissociation rates in the QGP. Left panels: NLO results using in-medium binding energies ranging from ~ 40 MeV to ~ 0 for $T = 190 \rightarrow 280$ MeV (upper left: T dependence of $\Gamma_{J/\psi}(k=0)$ for (a) quark- and (b) gluon-induced reactions for two constant values of the thermal parton masses [68]; lower left: $\Gamma_{J/\psi}$ as a function of the J/ψ velocity relative to the heat bath for different temperatures using T -dependent parton masses [69]). Right panels: comparison of the 3-momentum dependence of J/ψ (upper right) and χ_c (lower right) dissociation rates at 3 different temperatures using either gluo-dissociation with vacuum binding energies [61, 62] (dashed lines) or quasifree destruction with in-medium binding energies [23, 70] (solid lines).

is characterized by a temperature dependent dissociation energy, $E_{\text{diss}} \equiv \varepsilon_B$, while the coefficient has been estimated by the “geometric” transverse size of the bound state, $\pi r_{Q\bar{Q}}^2$ (cf. Ref. [67] for an alternative derivation of a similar result, which was shown to apply to sufficiently large dissociation energies, $E_{\text{diss}} \gg T$). To obtain more quantitative results, microscopic approaches are required.

In Refs. [23, 65] the dissociation reactions of weakly bound charmonia have been treated within a quasifree approximation for parton impact on either one of the heavy quarks within the bound state, $i + J/\psi \rightarrow c + \bar{c} + i$. The basic process is (quasi-) elastic $i + c \rightarrow i + c$ scattering [71], including the proper dissociation kinematics (i.e., finite ε_B and 4-momentum conservation), as well as thermal parton and Debye masses (the latter are essential to render the dominant t -channel gluon-exchange contributions finite). While these reactions are formally of next-to-leading order (NLO) compared to

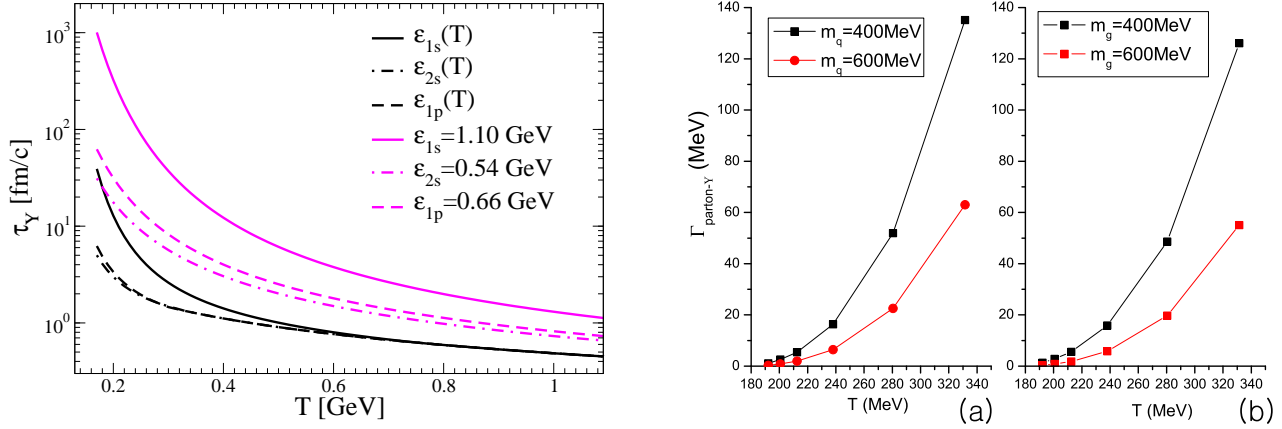


Figure 19: Bottomonium dissociation rates in the QGP. Left panel: quasifree calculation [72], $\Upsilon + i \rightarrow b + \bar{b} + i$ ($i=q, \bar{q}, g$), using $\alpha_s \simeq 0.25$ with vacuum (upper curves) and in-medium (lower curves) binding energies for Υ , χ_b and Υ' (the in-medium binding energies are based on Ref. [40], with $\varepsilon_B^{\Upsilon} \simeq 550(200)$ MeV at $T=180(350)$ MeV). Right panels: NLO calculations for quark- and gluon-induced break-up of Υ [68] (left and right sub-panel, respectively, including $\Upsilon + g \rightarrow b + \bar{b}$ and $\Upsilon + i \rightarrow b + \bar{b} + i$) with in-medium binding energies, $\alpha_s=0.5$ and two different values for thermal parton masses.

LO gluo-dissociation, the available phase space in the cross section is substantially increased (see solid line in the left panel of Fig. 17) leading to significantly larger dissociation rates at temperatures where the charmonium binding is weak (see solid line in the right panel of Fig. 17). A complete NLO calculation has recently been performed in Ref. [68] confirming the prevalence of $i + J/\psi \rightarrow c + \bar{c} + i$ over $g + J/\psi \rightarrow c + \bar{c}$ processes. For $\alpha_s=0.5$, $T=250$ MeV and thermal parton (Debye) masses $m_{q,g} = 400$ MeV, the total dissociation width of a weakly bound J/ψ has been found to be $\Gamma_{J/\psi} \simeq 350$ MeV, in good agreement with Refs. [23, 65] where $\Gamma_{J/\psi}(T=250\text{MeV}) \simeq 100$ MeV using $\alpha_s \simeq 0.25$ (the NLO rate is proportional to α_s^2 , modulo screening-mass corrections in t -channel gluon exchange diagrams for forward scattering; at $T=250$ MeV, the Debye mass in Refs. [23, 65] is $\mu_D=440$ MeV). For a constant Debye mass, the NLO results of Refs. [68] exhibit a rather strong increase of $\Gamma_{J/\psi}$ with temperature (upper left panel in Fig. 18), which is, however, tamed if a perturbative temperature dependence, $\mu_D \propto g(T)T$, were included. The dependence of the NLO rate on the 3-momentum, p , of the J/ψ is rather flat, see lower left panel in Fig. 18 [69]. This is quite different to the LO gluo-dissociation process whose rate drops substantially with p (even more so for weak binding for which the cross section is concentrated at small gluon energies), see dashed lines in the right panels of Fig. 18. The 3-momentum dependence following from the quasifree dissociation rate [70] (solid lines in the right panels of Fig. 18) is quite reminiscent to the full NLO calculation (recall that α_s differs by a factor of ~ 2 in these two calculations).

Inelastic collision rates of the ground-state Υ are compiled in Fig. 19. As for charmonia, in-medium reduced binding energies render the NLO (quasifree) process dominant over gluodissociation [72]², which has recently been confirmed in a complete NLO calculation [68]. Since the vacuum binding energy of the Υ is quite large ($\varepsilon_Y^0 \simeq 1.1$ GeV) compared to typical temperatures at RHIC ($T \simeq 0.3$ GeV), its dissociation rates are rather sensitive to the in-medium screening mechanism (which has important consequences for Υ suppression in heavy-ion collisions), e.g., ~ 30 fm/c for $\varepsilon_Y^0 \simeq 1.1$ GeV vs. ~ 2.5 fm/c for $\varepsilon_Y^{med} \simeq 0.25$ GeV at $T=0.3$ GeV. For comparable values of the parameters (strong coupling constant, binding energy as well as Debye and thermal masses), the results of the quasifree calculation [72] (left panel of Fig. 19) are again in reasonable agreement with the NLO analysis [68] (right panel of Fig. 19).

²For the vacuum binding energy, the gluo-dissociation rate of Υ is comparable to the quasifree one.

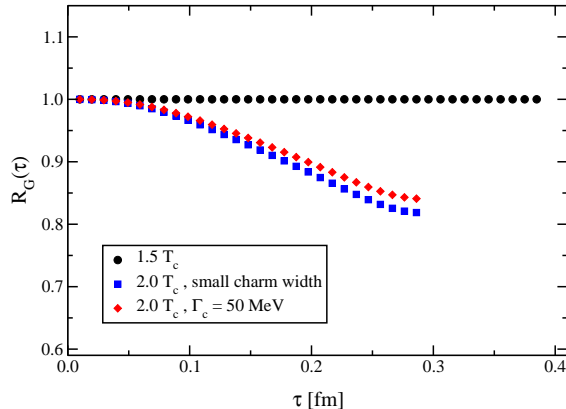


Figure 20: S -wave charmonium correlator ratios obtained within the T -matrix approach [50] using 2 different values for the in-medium charm-quark width corresponding to total η_c (or J/ψ) widths of 40 MeV (lower squares) and 100 MeV (diamonds); the reconstructed correlator used for normalization is the one at $1.5 T_c$, and the charm-quark mass has been held fixed at $m_c=1.7$ GeV (no susceptibility contributions are included).

Finally, let us briefly address the impact of finite-width effects on the charmonium correlators discussed in the previous Section. In the T -matrix approach of Ref. [50], a J/ψ width has been implemented via a charm-quark width in the two-particle propagator, $G_{\bar{Q}Q}$, figuring into the Lippmann Schwinger Eq. (16). This is in the spirit of the quasifree dissociation mechanism where the “hard” interaction of the thermal particles essentially occurs with one of the heavy quarks within the bound state. Using $\Gamma_c = \Gamma_{\bar{c}} = 50$ MeV, the J/ψ spectral function acquires a width of about 100 MeV, and the corresponding correlator ratio with this width is compared to the calculations shown in Fig. 12 (corresponding to a total J/ψ width of ~ 40 MeV), using the correlator at $1.5 T_c$ as the reconstructed one. One finds that the moderate increase of the J/ψ width increases the large- τ regime of the correlator ratio by only a few percent, due to the slight increase of strength in the low-energy regime of the spectral function caused by the broadening. More systematic investigations of width effects, especially close to the “melting” temperature, remain to be carried out, e.g., by implementing microscopic dissociation width calculations into the T -matrix approach.

2.4 Effective Models in Hadronic Matter

Calculations of charmonium dissociation reactions in hadronic matter can be generally divided into two categories, based on hadronic or quark degrees of freedom. We will primarily review and compare the studies of processes in a mesonic medium (predominantly composed of pions and rho mesons) within both approaches, including a discussion of in-medium effects.

Historically, a first calculation of the quark-exchange reaction, $J/\psi + \pi \rightarrow D + \bar{D}^* + c.c.$, was performed in a nonrelativistic quark model [73] based on applications of the diagrammatic technique developed by Barnes and Swanson [74] for meson-meson scattering, see also Ref. [75]. This calculation showed a strong energy dependence of the cross section with a peak value of about 6 mb at threshold and a fast decrease due to a momentum mismatch in the overlap integrals between the meson wave functions. The thermally averaged cross section, which is the relevant quantity for estimating the J/ψ dissociation rate, was below 1 mb, roughly in accordance with phenomenological expectations based on the observed suppression in heavy-ion reactions at the SPS. These calculations were extended to other light mesons and excited charmonia in Refs. [76, 77], where also more realistic quark-interaction potentials have been used. In Fig. 21 we show the diagrams for quark-exchange processes at first

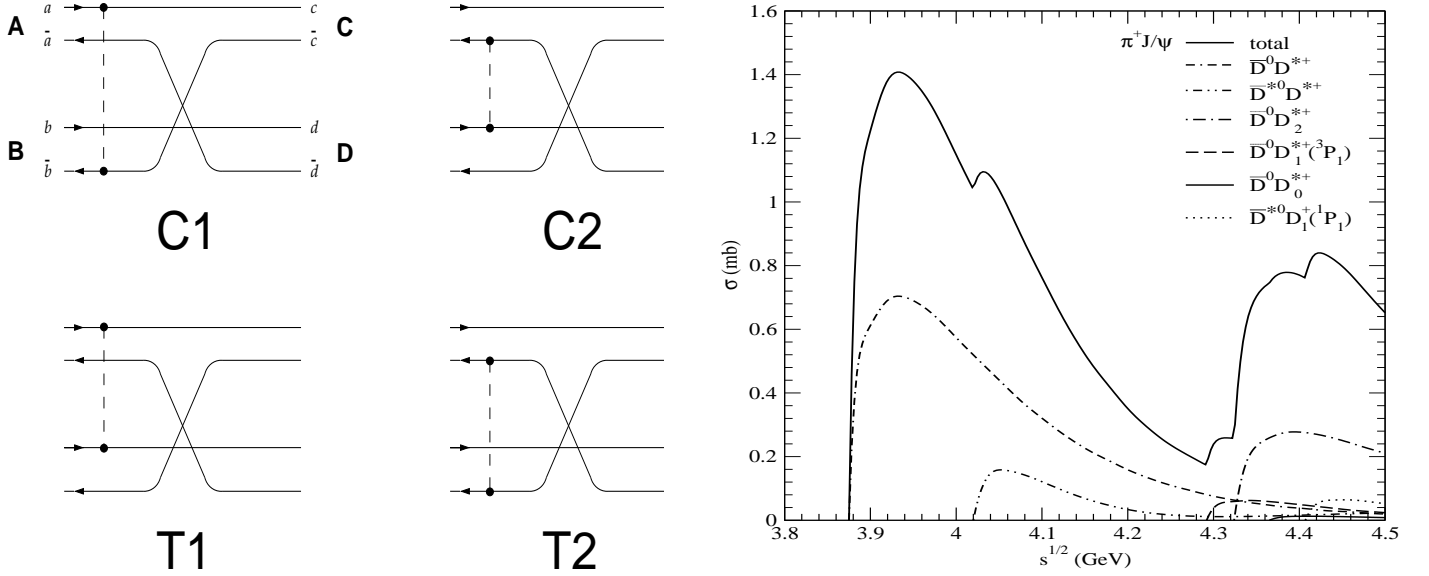


Figure 21: Born diagrams for quark-exchange processes contributing to heavy quarkonium dissociation by meson impact (left panels) and the corresponding cross section for J/ψ breakup by pion impact (right panel); from Refs. [76, 77].

Born order, which are classified as “capture” (C) and “transfer” (T) diagrams depending on whether the quark interaction can be absorbed into the external meson lines; the latter are to be understood as a resummation of ladder-type quark-antiquark interactions. There are cancellations among the contributions of the different diagrams due to the small color dipole of the charmonium state. These cancellations reduce the peak value of the cross section to about 1 mb, as also illustrated in Fig. 21. An open question in this approach is whether the double nature of the pion – a Goldstone boson of the broken chiral symmetry and a strongly bound quark-antiquark – has a strong influence on these results. In the nonrelativistic approach the pion emerges due to a large hyperfine splitting in the Fermi-Breit Hamiltonian (as opposed to, e.g., instanton-induced interactions), which is not a robust interpretation. Another question concerns the applicability of the truncation of the transfer diagram contributions at the first Born order. Ladder-type resummations would lead to s - and t -channel D -meson exchange processes, which are disregarded in the nonrelativistic quark exchange. Finally, these models are beset with the “post-prior” problem due to the ambiguity in the ordering of quark exchange and interaction lines.

These problems can be resolved within relativistic quark models developed on the basis of Dyson-Schwinger equations [78] for applications to the charmonium dissociation problem [79, 80]. In this approach, the meson-meson interactions are represented by quark-loop diagrams with three (triangle) and four (box) meson legs. The appearance of meson-exchange processes can be understood as a ladder resummation of quark interaction diagrams in s - and t -channels, see Fig. 22. The results for the J/ψ dissociation cross section by pion impact within the relativistic quark model [80], shown in Fig. 22, basically confirm those of the nonrelativistic approaches [73, 76, 77]; residual differences may be traced back to the treatment of the transfer-type diagrams.

Already in 1998, Matinyan and Müller [81] pioneered an alternative approach to charmonium absorption by light mesons on the basis of an effective meson Lagrangian, with a local $U(4)$ flavor symmetry strongly broken by the pseudoscalar and vector meson mass matrices. This initial version of the chiral Lagrangian approach gave rather small cross sections, $\sigma_{\pi\psi} \approx 0.3$ mb at threshold. It turned out [82, 83] that triple vector-meson couplings and contact terms, not included in Ref. [81], result in an increase of the breakup cross section by up two orders of magnitude, with a rising energy dependence. A problem for the chiral Lagrangian approaches is the treatment of hadrons as pointlike objects, which, as

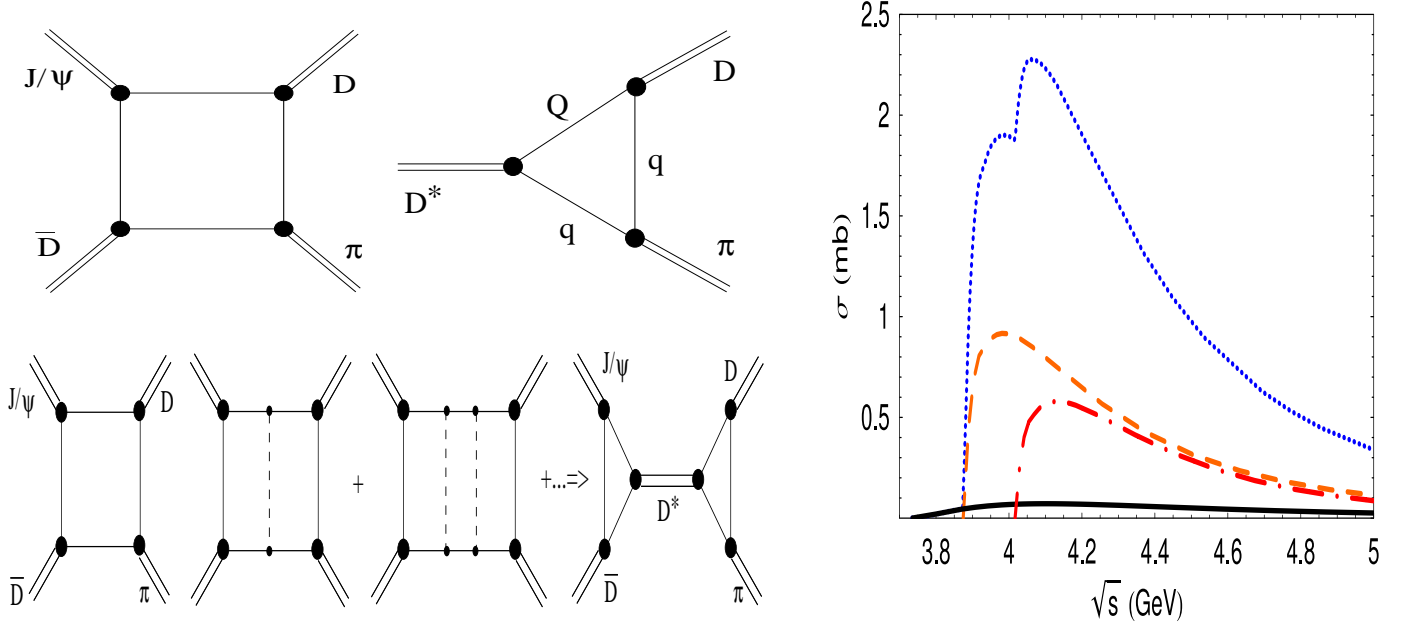


Figure 22: Left panel: box and triangle diagrams for meson-meson interaction vertices contributing to J/ψ breakup by meson impact in the relativistic quark model [79] (upper part), and the origin of D -meson exchange from ladder-type resummation (lower part). Right panel: cross section for pion induced J/ψ dissociation into open-charm mesons (dotted line) composed of subprocesses with different final-state D -meson pairs: $D + \bar{D}$ (solid), $D + \bar{D}^*$ (dashed), $D^* + \bar{D}^*$ (dash-dotted); from Ref. [80].

usual for an effective theory, becomes unreliable at high momentum transfers (due to quark-exchange substructure effects). The composite nature of hadrons can be accounted for in an approximate way by vertex form factors [83, 84], which reduce the magnitude, and affect the energy dependence, of the cross sections, see Fig. 23. The choice of the cutoff parameters in the form factors has a large effect on

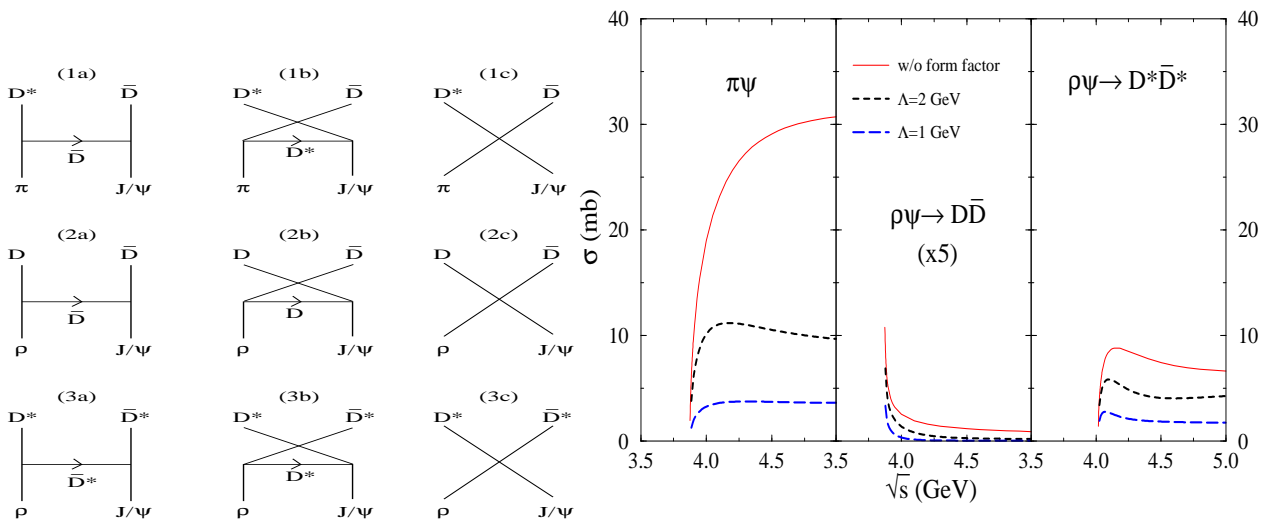


Figure 23: Feynman diagrams for J/ψ breakup by meson impact in the chiral Lagrangian approach (left) and the resulting cross sections for pion- and rho-meson induced processes (right), from Ref. [83, 85]. Note the role of the form factor at the meson-meson interaction vertices for the energy dependence and magnitude of the cross sections.

the charmonium breakup cross sections and remains a matter of debate [86, 87, 88, 89]. Progress may

be made by calibrating the form factors with microscopic approaches as, e.g., the nonrelativistic or the relativistic quark models. While the calculations with the relativistic quark model are very cumbersome, the chiral Lagrangian models offer a very effective tool to assess many other dissociation processes required for phenomenology, once the formfactor question is settled. In particular, these applications include dissociation processes by nucleon impact [90, 91] and bottomonium dissociation [92].

The energy dependent cross sections for heavy quarkonia dissociation by hadron impact enable to evaluate the temperature- (and density-) dependent dissociation rates in hadronic matter. Assuming the (short-distance) vertex functions not to be altered by the surrounding medium, there remains the issue of mass and widths changes of open-charm hadrons with temperature and density. These, in particular, imply modifications of the thresholds for the breakup processes [93, 94, 95, 96, 17, 97]. In Fig. 24 we show the quark-exchange diagram for the J/ψ selfenergy which develops an imaginary part (determining its width or inverse lifetime) due to the coupling to open-charm mesons. The right panel illustrates the effect of the spectral broadening of D -mesons at the chiral phase transition due to the opening of the decay channel into their quark constituents (Mott effect). These effects have been discussed as a possible mechanism underlying the threshold-like anomalous suppression pattern of J/ψ 's observed by the NA50 experiment [98, 95].

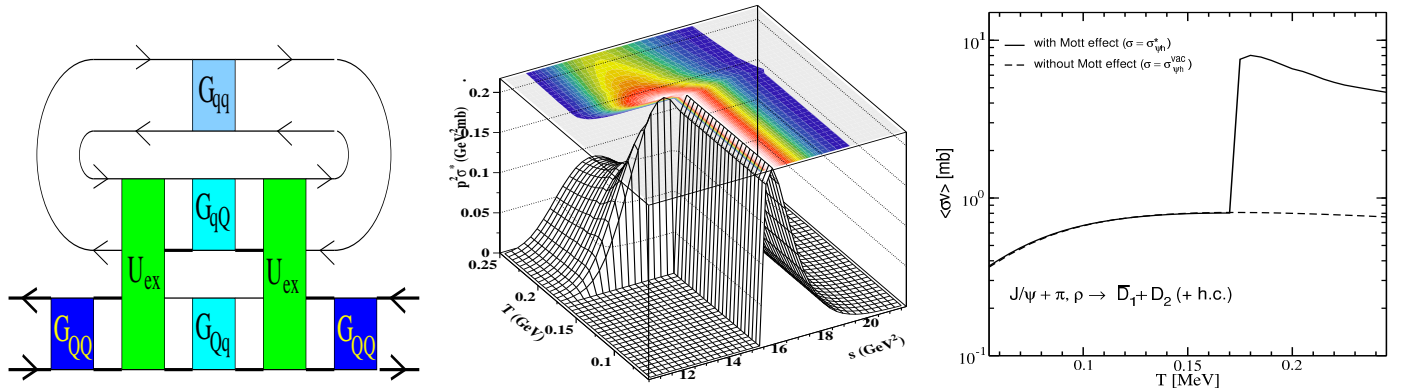


Figure 24: Left panel: quark-exchange process contributing to heavy quarkonia dissociation in a mesonic medium; middle panel: energy and temperature dependence of the cross section for J/ψ breakup by ρ -meson impact; right panel: temperature dependence of the thermally averaged J/ψ breakup cross section in a π - ρ meson gas; the calculation with vacuum D -mesons (dashed line) is compared to one with an in-medium broadening of the D -meson spectral function (due to the Mott effect at the chiral phase transition) which exhibits a steplike enhancement (solid line) caused by the effective lowering of the breakup threshold; from Ref. [99].

2.5 Insights from Plasma Physics

In developing a theoretical approach to heavy quarkonia as messengers of the deconfinement/ hadronization transition of a quark-gluon plasma formed in a heavy-ion collision, we should finally aim at a unifying description where hadrons appear as bound states (clusters) of quarks and gluons. The situation is analogous to the problem of two-particle states in QED plasmas where a well-developed theory in the framework of the Green function technique exists. These methods have been widely developed for the case of the hydrogen plasma, where the electrons and protons as the elementary constituents can form hydrogen atoms as bound states of the attractive Coulomb interaction. The problem is tractable analytically for the isolated two-particle system, with a discrete energy spectrum of bound states and a continuous spectrum of scattering states. Higher complexes, such as molecular hydrogen can also be formed.

In a many-particle system, the problem of bound state formation needs to account for medium effects. They give contributions to a plasma Hamiltonian

$$H^{\text{pl}} = H^{\text{Hartree}} + H^{\text{Fock}} + H^{\text{Pauli}} + H^{\text{MW}} + H^{\text{Debye}} + H^{\text{polpot}} + H^{\text{vdW}} + \dots, \quad (24)$$

where the first three effects, the Hartree-Fock energies of one-particle states and the Pauli blocking for the two-particle states, are of first order with respect to the interaction and determine the mean-field approximation. The following two terms of the plasma Hamiltonian are the Montroll-Ward term giving the dynamical screening of the interaction in the self-energy, and the dynamical screening (Debye) of the interaction between the bound particles. These contributions are related to the polarization function and are of particular interest for plasmas due to the long-range character of the Coulomb interaction. In a consistent description, both terms should be treated simultaneously. The last two contributions to the plasma Hamiltonian are of second order with respect to the interaction: the polarization potential, describing the interaction of a bound state with free charge carriers, and the van der Waals interaction, accounting for the influence of other bound states on the two-particle system under consideration, see [51, 4].

Approximations to medium effects in the self-energy and the effective interaction kernel have to be made in a consistent way, resulting in predictions for the modification of one-particle and two-particle states. On this basis, the kinetics of bound state formation and breakup processes can be described, establishing the ionization equilibrium under given thermodynamical conditions [100]. Coulomb systems similar to the hydrogen plasma are electron-hole plasmas in semiconductors [101], where excitons and biexcitons play the role of the atoms and molecules. Other systems which have been widely studied are expanded fluids like alkali plasmas or noble gas plasmas, see [4] and references therein. Applications of the plasma physics concepts for cluster formation and Mott effect to the rather short-ranged strong interactions have been given, e.g., in [102, 103] for nuclear matter and in [104, 105].

In this subsection, we want to discuss basic insights from these investigations of bound state formation in plasmas, as far as they can concern our discussion of heavy quarkonia formation in hot and dense matter. Before going more into the details, let us mention them. Due to a partial compensation of self-energy and interaction effects for bound states in lowest order of density and temperature, these remain rather inert to changes of the medium. Also, the smaller size of the bound states matters in this respect. The compensation does not hold for continuum states, being influenced by self-energy effects only, so that a lowering of the in-medium ionization threshold must occur which leads to a strong enhancement of the rate coefficients for bound-free transitions and to a sequential “melting” of different bound state excitation levels into the continuum of scattering states at corresponding critical plasma parameters (Mott effect [3]), until even the ground state becomes unbound.

The theory of strongly coupled plasmas has been developed also for strong nonideality, where the formation of clusters in the medium need to be taken into account. This situation is similar to that of a hadronizing quark-gluon plasma and we will therefore refer to cluster expansion techniques as the theoretical basis.

Bethe-Salpeter equation and plasma Hamiltonian The most systematic approach to the description of bound states in plasmas uses the Bethe-Salpeter equation (BSE) for the thermodynamic (Matsubara-) two-particle Green function

$$G_2 = G_2^0 + G_2^0 K G_2 = G_2^0 + G_2^0 T_2 G_2^0, \quad (25)$$

which is equivalent to the use of the two-particle T-matrix T_2 and has to be solved in conjunction with the Dyson equation for the full one-particle Green function,

$$G_1 = G_1^0 + G_1^0 \Sigma G_1, \quad (26)$$



Figure 25: The two-particle problem in the medium. Dyson equation (left) and Bethe-Salpeter equation (right) need to be solved in consistent (conserving) approximations for self-energy (Σ) and interaction kernel (K).

defined by the dynamical self-energy $\Sigma(\mathbf{p}, \omega_\nu)$ and the free one-particle Green function $G_1^0(\mathbf{p}, \omega_\nu) = [\omega_\nu - \varepsilon(\mathbf{p})]^{-1}$, see Fig. 2.5. The BSE contains all information about the spectrum of two-particle bound as well as scattering states in the plasma. In the context of plasma physics, the in-medium effects contained in (25) have been singled out in the definition of a plasma Hamiltonian, containing all modifications beyond the two-body problem in free space [51, 101]. As the proper formulation of the plasma effects on the two-particle spectrum is essential to understand why bound and scattering states are influenced in a different way by the surrounding medium, leading to the Mott-effect for bound states, we give here the essence of a detailed discussion in Ref.[51].

The BSE (25) can be given a symmetric Hermitean form resulting in

$$\{H_{ab}^{(0)} - \Omega_\lambda\} \bar{G}_2(\Omega_\lambda) + H_{ab}^{pl}(\Omega_\lambda) \bar{G}_2(\Omega_\lambda) = i, \quad (27)$$

where $H_{ab}^{(0)}$ is the Hamiltonian of the isolated two-particle system with the matrix elements

$$\langle p_1 p_2 | H_{ab}^{(0)} | p'_1 p'_2 \rangle = \{\varepsilon_a(p_1) + \varepsilon_b(p_2)\} \delta_{p_1 p'_1} \delta_{p_2 p'_2} + V(p_1 p_2, p'_1 p'_2), \quad (28)$$

with $\varepsilon_a(p) = \sqrt{m_a^2 + p^2} \approx m_a + p^2/(2m_a)$ being the dispersion relation for species a and V the bare two-particle interaction potential. The effects of the surrounding plasma on the two-particle state are absorbed into the plasma Hamiltonian H_{ab}^{pl} with the matrix elements

$$\langle p_1 p_2 | H_{ab}^{pl} | p'_1 p'_2 \rangle = \Delta_{ab}^{\text{eff}}(p_1 p_2, \Omega_\lambda) \delta_{p_1 p'_1} \delta_{p_2 p'_2} + N_{ab}^{1/2} V_{ab}^{\text{eff}}(p_1 p_2, p'_1 p'_2, \Omega_\lambda) N_{ab}^{1/2} - V(p_1 p_2, p'_1 p'_2). \quad (29)$$

The phase space occupation (Pauli-blocking) factors N_{ab} stem from a Matsubara summation

$$N_{ab}(p_1 p_2) = T \sum_\nu [G_a(p_1, \omega_\nu) + G_b(p_2, \Omega_\lambda - \omega_\nu)] \approx 1 - f_a(p_1) - f_b(p_2). \quad (30)$$

They were absorbed into the definition of the two-particle Green function

$$\bar{G}_2(p_1 p_2, p'_1 p'_2, \Omega_\lambda) = G_2(p_1 p_2, p'_1 p'_2, \Omega_\lambda) N_{ab}^{-1/2}(p_1 p_2) N_{ab}^{-1/2}(p'_1 p'_2). \quad (31)$$

Note that in general both, the effective self energy

$$\Delta_{ab}^{\text{eff}}(p_1 p_2, \Omega_\lambda) = N_{ab}^{-1}(p_1 p_2) \sum_\nu [\Sigma_a(p_1, \omega_\nu) + \Sigma_b(p_2, \Omega_\lambda - \omega_\nu)] [G_a(p_1, \omega_\nu) + G_b(p_2, \Omega_\lambda - \omega_\nu)] \quad (32)$$

and the effective interaction

$$\begin{aligned} V_{ab}^{\text{eff}}(p_1 p_2, p'_1 p'_2, \Omega_\lambda) &= T^2 \sum_{\nu \nu'} [G_a(p_1, \omega_\nu) + G_b(p_2, \Omega_\lambda - \omega_\nu)] N_{ab}^{-1}(p'_1 p'_2) \\ &\quad \times K(p_1 p_2, p'_1 p'_2, \omega_\nu, \Omega_\lambda - \omega_\nu, \omega_{\nu'}) [G_a(p'_1, \omega_{\nu'}) + G_b(p'_2, \Omega_\lambda - \omega_{\nu'})] \\ &\approx K(p_1 p_2, p'_1 p'_2, \Omega_\lambda) N_{ab}(p_1 p_2) \end{aligned} \quad (33)$$

are frequency-dependent due to their dynamical character and closely related to each other. In the screened potential (V_S)-approximation, when the interaction kernel gets replaced by $V_S(p_1 p_2, p'_1 p'_2, \Omega_\lambda) = V_S(q, \Omega_\lambda) \delta_{p_1 + p_2, p'_1 + p'_2} \delta_{q, p_1 - p_2}$ with

$$V_S(q, \Omega_\lambda) = V(q) + V(q) \Pi(q, \Omega_\lambda) V_S(q, \Omega_\lambda) = V(q) [1 - \Pi(q, \Omega_\lambda) V(q)]^{-1}, \quad (34)$$

the effective interaction and the one-particle shifts are related by

$$\Delta_{ab}^{\text{eff}}(p_1 p_2, \Omega_\lambda) = \sum_{p'_1 p'_2} \left[V_{ab}^{\text{eff}}(p_1 p_2, p'_1 p'_2, \Omega_\lambda) N_{ab}(p'_1 p'_2) - V(p_1 p_2, p'_1 p'_2) \right]. \quad (35)$$

Most frequently used approximation for the polarization function $\Pi(q, z)$ introduced here, or for the equivalent dielectric function $\varepsilon(q, z) = 1 - \Pi(q, z)V(q)$, is the random phase approximation (RPA). In the next subsections we discuss the RPA and its generalization for a clustered medium.

Using the spectral representation for H_{ab}^{pl}

$$H_{ab}^{pl}(\Omega_\lambda) = \bar{H}_{ab}^{pl} + \int \frac{d\omega}{\pi} \frac{\text{Im} H_{ab}^{pl}(\omega + i0)}{\Omega_\lambda - \omega}, \quad (36)$$

with \bar{H}_{ab}^{pl} being the frequency independent part of H_{ab}^{pl} , and subsequent analytical continuation to the complex Ω -plane, the BSE takes the form

$$\left\{ H_{ab}^{\text{eff}} - (\omega \pm i0) \right\} \bar{G}_2(\omega \pm i0) \pm i \text{Im} H_{ab}^{pl}(\omega - i0) \bar{G}_2(\omega \pm i0) = i, \quad (37)$$

with the effective Hamiltonian

$$H_{ab}^{\text{eff}}(\omega) = H_{ab}^{(0)} + \bar{H}_{ab}^{pl} + \mathcal{P} \int \frac{d\bar{\omega}}{\pi} \frac{\text{Im} H_{ab}^{pl}(\bar{\omega} - i0)}{\omega - \bar{\omega}}, \quad (38)$$

depending on the frequency ω as a real parameter. In order to solve the spectral properties of two-particle states in a plasma, one should use as a basis the complete set of orthonormal eigenstates to H_{ab}^{eff}

$$H_{ab}^{\text{eff}}(\omega) |nP, \omega\rangle = E_{nP}(\omega) |nP, \omega\rangle, \quad (39)$$

depending on ω , and introduce a wave function $\langle p' P' | nP, \omega \rangle = \delta_{PP'} \Psi_n(p', P, \omega)$. Solving (39) by perturbative methods, one finds for the bound state spectrum

$$\tilde{E}_{nP} \approx E_{nP}^{(0)} + \langle Pn | \bar{H}_{ab}^{pl} + \mathcal{P} \int \frac{d\bar{\omega}}{\pi} \frac{\text{Im} H_{ab}^{pl}(\bar{\omega} - i0)}{E_{nP}^{(0)} - \bar{\omega}} | nP \rangle, \quad (40)$$

and for the scattering part

$$\tilde{E}_{pP} \approx E_{pP}^{(0)} + \text{Re} \Delta_{ab}^{\text{eff}}(p, P, E_{pP}^{(0)}), \quad (41)$$

where the free two-particle spectrum is given by $E_{pP}^{(0)} = M_{ab} + \frac{p^2}{2m_{ab}} + \frac{P^2}{2M_{ab}}$, with the reduced mass $m_{ab} = m_a m_b / M_{ab}$ and the total mass $M_{ab} = m_a + m_b$ of the two-particle system. Here we observe the essential point of our discussion: the different behavior of bound and scattering state energies which leads to a decrease in the ionization energy and its vanishing at the Mott effect. The different behaviour of bound and scattering states can also be discussed from the homogeneous wave equation associated with the BSE (37) [101]

$$\begin{aligned} & [\varepsilon_a(p_1) + \varepsilon_b(p_2) - z] \psi_{ab}(p_1 p_2, z) - \sum_q V(q) \psi_{ab}(p_1 + q, p_2 - q, z) \\ &= \sum_q V(q) [N_{ab}(p_1 p_2) - 1] \psi_{ab}(p_1 + q, p_2 - q, z) \quad (\text{i}) \\ &- \sum_q V(q) [N_{ab}(p_1 + q, p_2 - q) - 1] \psi_{ab}(p_1, p_2, z) \quad (\text{ii}) \\ &+ \sum_q \Delta V_{ab}^{\text{eff}}(p_1, p_2, q, z) N_{ab}(p_1 p_2) \psi_{ab}(p_1 + q, p_2 - q) \quad (\text{iii}) \\ &- \sum_q \Delta V_{ab}^{\text{eff}}(p_1, p_2, q, z) N_{ab}(p_1 + q, p_2 - q) \psi_{ab}(p_1, p_2, z) \quad (\text{iv}), \end{aligned} \quad (42)$$

where (29) has been used and $\Delta V_{ab}^{\text{eff}} = V_{ab}^{\text{eff}} - V_{ab}$. This equation is a generalization of the two-particle Schrödinger equation, where on the left-hand side the isolated two-particle problem is described while many-body effects due to the surrounding medium are given on the right-hand side. These are

- (i) Phase space occupation (statistical correlation, Pauli-blocking)
- (ii) Exchange self-energy
- (iii) Dynamically screened effective potential
- (iv) Dynamical self-energy .

When applying to heavy quarkonia in a medium where heavy quarks (either free or bound in heavy hadrons) are rare, then $N_{ab} = 1$ so that both, (i) and (ii) can be safely neglected. The effects (iii) and (iv) stem from the dynamical coupling of the constituents of the two-particle state to collective excitations (plasmons) in the medium. Due to the large mass in the heavy quarkonium case, one may use the argument of a Born-Oppenheimer expansion to replace these effects by their static (and long-wavelength) limits.

Example: statically screened Coulomb potential The systematic account of the modification of the interaction potential between charged particles a and b by polarization of the medium is taken into account in the dynamical polarization function $\Pi_{ab}(q, z)$, which in RPA reads

$$\Pi_{ab}^{\text{RPA}}(q, z) = 2\delta_{ab} \sum_a \int \frac{d\mathbf{p}}{(2\pi)^3} \frac{f_a(E_{\mathbf{p}}^a) - f_a(E_{\mathbf{p}-q}^a)}{E_{\mathbf{p}}^a - E_{\mathbf{p}-q}^a - z} . \quad (43)$$

For the Coulomb interaction, corresponding to the exchange of a massless vector boson, the potential is obtained from the longitudinal propagator in the Coulomb gauge (see, e.g., [106, 39] for a recent discussion in the context of heavy quark correlators and potentials) $V_{ab}(q) = e_a e_b / q^2$. The corresponding RPA dielectric function $\varepsilon^{\text{RPA}}(q, \omega)$ becomes in the static, long wavelength limit for a nondegenerate (Boltzmann) system

$$\lim_{q \rightarrow 0} [\varepsilon^{\text{RPA}}(q, 0) - 1] = \frac{\mu_D^2}{q^2} , \quad \mu_D^2 = \frac{1}{T} \sum_a e_a^2 n_a(T) . \quad (44)$$

The screened Coulomb potential is therefore $V_{ab}^S(q) = e_a e_b / (q^2 + \mu_D^2)$. In this “classical” example of the statically screened Coulomb interaction, the contribution to the plasma Hamiltonian is real and in coordinate representation is given by

$$\Delta V_{ab}^{\text{eff}}(r) = -\frac{\alpha}{r} (e^{-\mu_D r} - 1) \approx \alpha \mu_D - \frac{\alpha}{2} \mu_D^2 r . \quad (45)$$

The corresponding energy shift of the two-particle continuum states is

$$\Delta_{ab}^{\text{eff}} \approx \alpha \mu_D = \mathcal{O}(\sqrt{n a_{\text{B},0}^3}) , \quad (46)$$

whereas for the bound states this self-energy shift of the constituents gets compensated to lowest order in the density by the constant term in (45), so that [51, 107]

$$\Delta E_{\text{nl}} \approx -\frac{\alpha}{2} \mu_D^2 \langle r \rangle_{\text{nl}} = \mathcal{O}(n a_{\text{B},0}^3) , \quad (47)$$

where $\alpha = e^2/(4\pi)$ is the fine structure constant and $a_{\text{B},0} = 1/(\alpha m)$ is the Bohr radius. The Debye mass μ_D , equivalent to the inverse of the Debye radius r_D characterizing the effective range of the interaction, depends on the square root of the density $n(T)$ of charge carriers. It is this different response of bound

states and scattering continuum to an increase of density and temperature in the medium which leads to the Mott effect (see, e.g., Refs. in [3] and [4]) for electrons in an insulator: bound states of the Debye potential can only exist when the Debye radius is larger than [108]

$$r_{D,Mott} = 0.84 a_{B,0} . \quad (48)$$

This entails that above a certain density even the ground state electrons become unbound and form a conduction band, resulting in an insulator-metal transition also called Mott-transition.

In complete analogy to this electronic Mott effect it is expected that in hadronic matter under compression the hadrons as bound states of quarks undergo a Mott transition which results in a phase transition from the color insulating phase of hadronic matter to a color conducting or even color superconducting phase of deconfined quark matter. This applies to light hadrons as well as to heavy quarkonia, whereby due to the different scales of Bohr radii the Mott dissociation of heavy quarkonia occurs at higher densities than for light hadrons.

In most approaches the quark self energy effects are neglected and one is left with the only medium effect due to a statically screened potential. This has the consequence that in such a picture the continuum edge of the scattering states remains unshifted and due to the lack of compensation the effective interaction leads to a strong medium dependence of the bound state energies (masses). For the electron-hole plasma in highly excited semiconductors it could be shown experimentally, however, that the compensation picture is correct and the bound state energies remain almost unshifted [109].

One may of course absorb the self-energy effects into a redefinition of the effective interaction, by adding a homogeneous mean-field contribution. This is equivalent to the use of the Ecker-Weitzel potential [110]

$$V_{\text{Ecker-Weitzel}}(r) = -\frac{\alpha}{r} e^{-\mu_D r} - \alpha \mu_D . \quad (49)$$

It is interesting to note that recent investigations of the screening problem in the context of Debye-Hückel theory [111] and $Q\bar{Q}$ correlators [106, 39] have obtained this continuum shift ($-\alpha\mu_D$) as a homogeneous background field contribution. According to the above lesson from plasma physics, however, this contribution should rather be attributed to the selfenergy of the constituents rather than to the interaction kernel, since it determines the shift of the continuum edge.

For the development of a comprehensive approach to heavy quarkonia in hadronizing hot, dense QCD matter, two more insights from plasma physics may be of relevance and will be discussed next: (1) the effect of strong correlations (bound states) in the medium and (2) the effect of collisions on two-particle states.

Two-particle states in the medium: cluster expansion In the vicinity of the plasma phase transition, correlations play an important role and their proper accounting requires rather sophisticated theoretical methods such as cluster expansion techniques. For the problem of charmonium in dense hadronic matter at the deconfinement transition, i.e. in the strong coupling case, we suggest a systematic Born series expansion of collisions with free and bound states in the surrounding matter so that all terms linear in the density of free particles and bound states are taken into account.

We describe the cluster expansion here in terms of their diagrammatic expressions for the interaction kernel and the corresponding self-energy in Fig. 26.

The 1st Born approximation diagrams of this expansion are given in Fig. 27, see also the monograph [51]. They do not contribute to the charmonium spectrum as long as the densities of the charmed quarks and of charmed hadrons in the medium are negligible. This is the situation expected for the rather low-energy CBM experiment. For the discussion of charmonium production at RHIC and at LHC the inclusion of these terms has to be invoked.

At the 2nd Born order, we distinguish two classes of collisions with light clusters (hadrons) that can give rise to spectral broadening of the charmonia, see Fig. 28: (a) impact without quark rearrangement

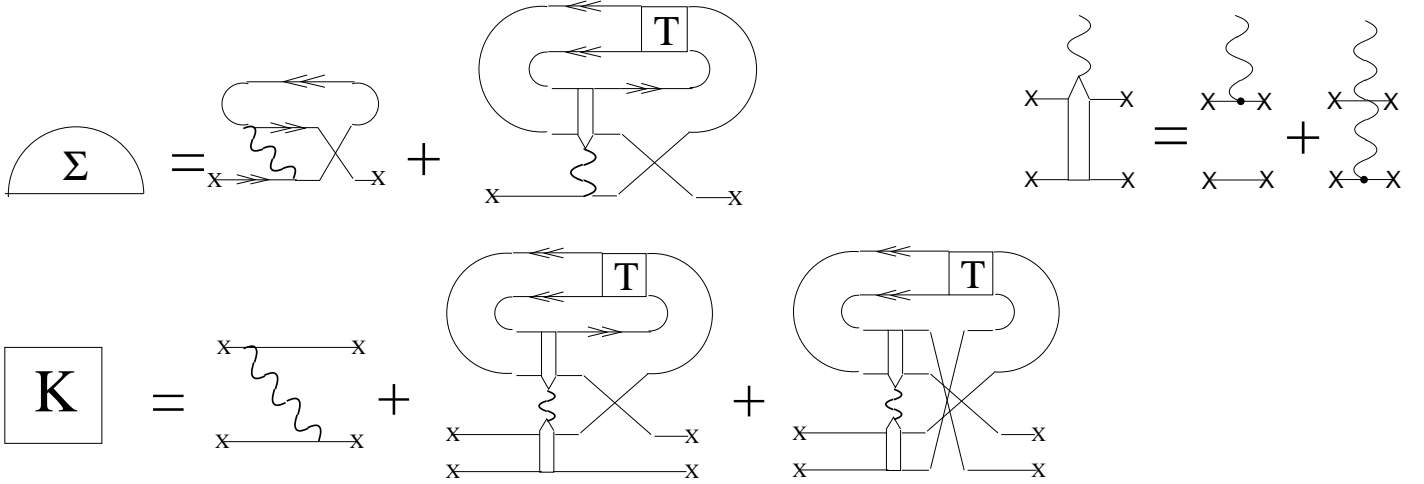


Figure 26: The cluster expansion for self-energy (upper left equation) with a dipole ansatz for the vertex (upper right equation) and interaction kernel (lower diagram equation) for the two-particle problem in a strongly correlated medium.

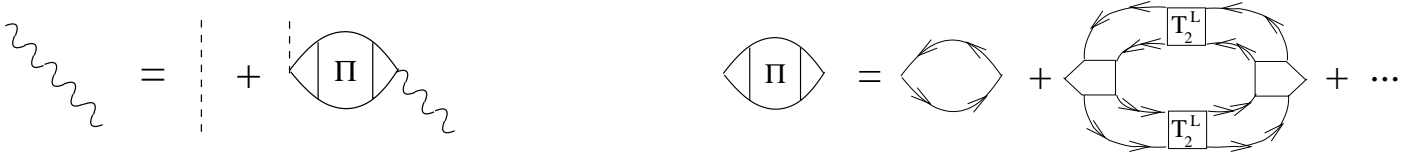


Figure 27: The dynamically screened interaction potential V_s (left diagram equation) and the generalized (cluster-) RPA for the polarization function $\Pi(\omega, q)$ (right diagram equation).

inducing transitions to excited states, and (b) impact with quark rearrangement inducing transitions to open charm hadrons. While the former collisions just result in a deformation of the spectrum under conservation of the spectral weight integrated over all charmonia, the latter processes are responsible for the suppression of charmonia, as indicated in Fig. 28.

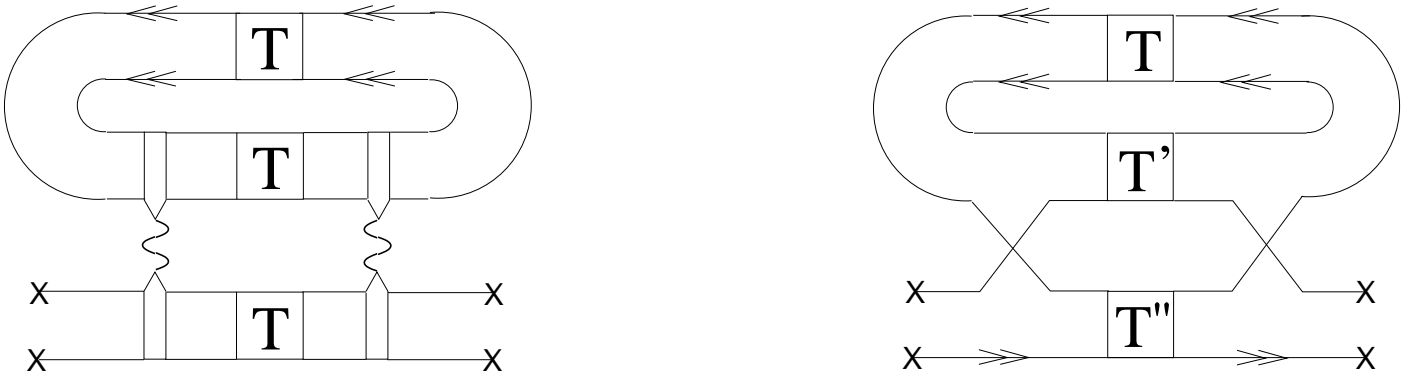


Figure 28: Contributions to the dynamical self-energy of a two-particle system in a correlated medium at 2^{nd} Born order: (a) impact by two-particle states without constituent exchange (left diagram) and (b) constituent-rearrangement collisions (right diagram).

Beyond the 2^{nd} Born approximation, one may follow a ladder-type resummation of the quark exchange (string-flip) matrix elements given in Fig. 29 which result in a coupled channel problem for the charmonium-hadron system, with possible molecular 4-quark states as solutions. Such a molecular state is discussed as an explanation of the X(3872) state of the charmonium spectrum which has recently been found, see [112] and references therein.

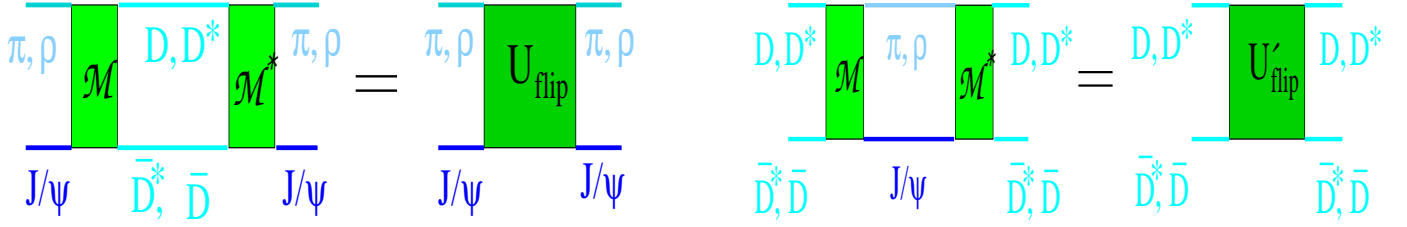


Figure 29: Effective potential for the coupling of the charmonium to the open charm channel (left) and vice versa (right).

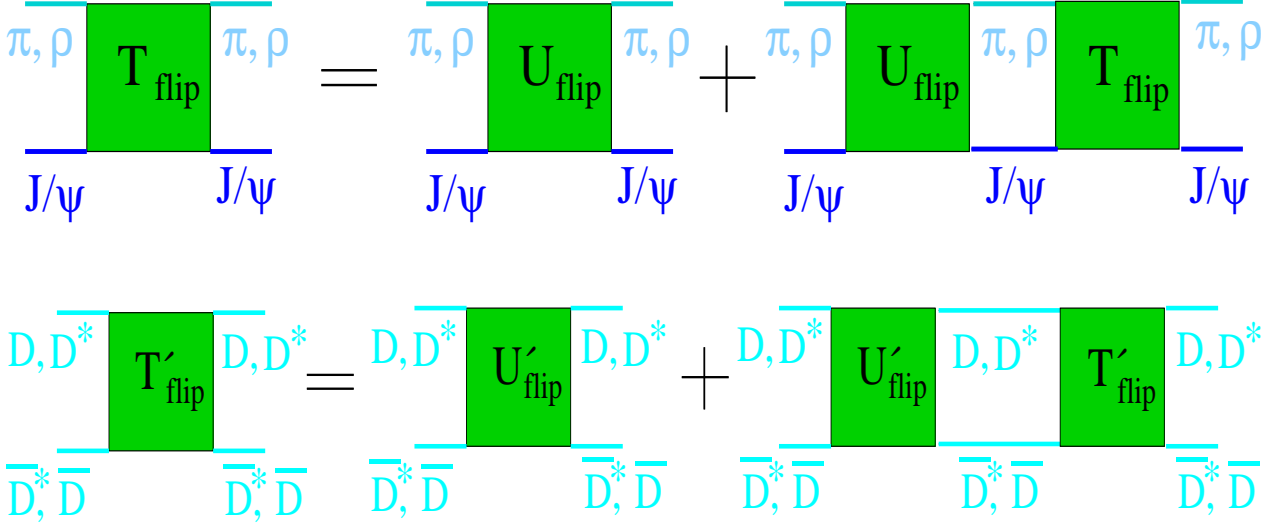


Figure 30: Bethe-Salpeter equation for molecular states which can be expected close to the threshold, in particular in a dense medium when the channel coupling can become resonant. Similar process exists for charm exchange with baryons.

It is outlined that close to the critical temperatures and/or densities where binding energies tend to zero, the thermal activation and quark rearrangement processes have to be taken into account when extracting spectral properties. In strongly correlated matter close to the deconfinement phase transition, this requires to take into account higher order correlations and to develop approaches for describing charmonium in a correlated medium.

One striking feature of such a description is the coupling to open charm channels which turn out to be more sensitive to changes of the medium properties than the charmonium ground states (J/ψ and η_c). It is possible that in the situation close to their dissociation threshold charmonia states become degenerate with the formation of molecular states of open charm hadrons. This would result in strong modifications of the effective quark-antiquark potential and also in new features for the spectroscopy of charmed hadrons and their decays due to catalysis in the medium.

3 Quarkonia in Heavy-Ion Collisions

Utilizing heavy quarkonia as a probe of the medium created in heavy-ion reactions has to rely on the analysis of their final number and spectra. Since the equilibration of quarkonia is generally not warranted, the interface between their in-medium properties and observables is usually based on transport approaches (Sec. 3.1). If the bulk medium is in local thermal equilibrium, the in-medium properties (as elaborated in the previous Section) enter in the form of relaxation times (dissociation rates) and asymptotic limits (equilibrium abundancies). With realistic initial conditions, usually inferred from p -A

collisions (Sec. 3.2), a broad investigation over a wide range of energies can be performed (Sec. 3.3).

3.1 Charmonium Transport

The evolution of the abundance and spectrum of a quarkonium state, Ψ , in a hot and dense fireball can be tracked via its phase space distribution, f_Ψ , satisfying a transport equation of the form

$$p^\mu \partial_\mu f_\Psi(\vec{r}, t; \vec{p}) = -E_\Psi \Gamma_\Psi(\vec{r}, t; \vec{p}) f_\Psi(\vec{r}, t; \vec{p}) + E_\Psi \beta_\Psi(\vec{r}, t; \vec{p}) \quad (50)$$

(mean-field terms have been neglected which is justified if mass corrections are small). The right-hand-side of this equation is the collision term which accounts for both dissociation and formation reactions (possibly including transitions between different charmonium states). Detailed balance (and the correct equilibrium limit) requires that both terms include the same reaction mechanisms.

Let us first discuss the situation where the gain term in the transport equation can be neglected; this can be realized in scenarios (or evolution phases) where either no charmonium states are present and/or the actual charmonium number is much larger than the equilibrium abundance in connection with relatively small reaction rates. Under these circumstances, the evolution of the charmonium number is given by a sequence of suppression stages for which the solution of the rate equation may be schematically written in terms of a (3-momentum dependent) survival probability (or suppression factor)

$$\begin{aligned} S_\Psi &= S_{\text{HG}} S_{\text{QGP}} S_{\text{nuc}} \\ &\simeq \exp \left(- \int_{T_c}^{T_{fo}} \Gamma_{\text{HG}}(T) \frac{dT}{T} \right) \exp \left(- \int_{T_c}^{T_0} \Gamma_{\text{QGP}}(T) \frac{dT}{T} \right) \exp(-n_N \sigma_{\text{abs}} L) . \end{aligned} \quad (51)$$

In this approximation the key ingredients are the inelastic reaction rates in hadron gas (HG) and QGP phases, as well as primordial nuclear absorption (which will be discussed in more detail in the following Section, 3.2). If the latter can be accurately determined from p -A data, and if the hadronic suppression is small, S_Ψ provides direct information on the (temperature-dependent) inelastic reaction rate in the QGP (recall that the complete melting of a charmonium state (e.g. due to color screening) maybe be considered as the $\Gamma_\Psi \rightarrow \infty$ limit). As discussed in the introduction, the suppression approach has been widely applied in the interpretation of SPS data on charmonium production in light- and heavy-ion reactions, encompassing a wide range of models for both the charmonium dissociation mechanisms (hadronic comovers [113, 8, 9, 114, 115], screening-based models [1, 12, 116], as well as thermal dissociation rate calculations) and the evolution of the medium (transport, fireball and hydrodynamic simulations). An updated account of the state-of-affairs in this enterprise will be given in Sec. 3.3 below. The suppression factor, Eq. (51), encodes no notion of the charmonium masses, of their equilibrium number, nor of any coupling to the open-charm content in the system. These aspects, however, become essential upon inclusion of regeneration processes, i.e., the gain term in Eq. (50), as we will now discuss.

Early evaluations of secondary charmonium production in heavy-ion collisions were focusing on hadronic regeneration reactions in the hadronic [117] and mixed phases [118] under LHC conditions. In Refs. [119, 21, 120] (see, e.g., Ref. [121] for a recent update) the statistical hadronization model has been invoked assuming that charmonia thermally equilibrate (and diffuse into a homogeneous distribution) upon completion of the hadronization phase transition (on the hadronic side), without further modifications in their abundances in the subsequent hadronic phase. In terms of the rate equation (50) this implies that the thermal relaxation time (or inelastic width) of charmonia changes rather rapidly across the phase transition, which is supported by the microscopic calculations discussed in the previous two Sections (at least for the J/ψ). It also implies that the open charm states forming the charmonia have kinetically equilibrated. This assumption is less certain, with current estimates of the thermal relaxation time of charm quarks of around $\tau_c \simeq 5\text{-}7 \text{ fm}/c$ [122]. However, it is presently an open

question by how much the J/ψ regeneration yield is affected by deviations of charm-quark distributions from thermal equilibrium. E.g., when comparing the limiting cases of either primordial spectra or a thermal source (+flow), a factor of ~ 3 difference in the J/ψ yield in central Au–Au at RHIC has been found in the coalescence model of Ref. [123], while the variations in the transport model of Ref. [124] are much smaller. In Ref. [119] it was additionally assumed that charm equilibrated chemically with the surrounding medium, so that the charmonium density is determined solely by its mass and the ambient temperature. With a hadronization temperature of $T_c = 175$ MeV, a surprisingly good description of the J/ψ -over-pion ratio at the SPS was found. In Ref. [21] the assumption of chemical equilibration of charm-quarks was relaxed based on theoretical expectations [125] that $c\bar{c}$ pair production is restricted to primordial N - N collisions and frozen thereafter (available experimental data at RHIC [126] and SPS [127] support this assertion). Under these conditions, charmonium production at the hadronization transition corresponds to a coalescence of available charm and anticharm quarks. In thermal equilibrium, this leads to a charmonium density

$$n_\Psi^{\text{eq}}(m_\Psi; T, \gamma_c) = d_\Psi \gamma_c^2 \int \frac{d^3p}{(2\pi)^3} f_\Psi(\omega_p; T) , \quad (52)$$

where $\gamma_{\bar{c}} = \gamma_c$ denote a (anti-) charm-quark fugacity. In *relative* chemical equilibrium, the latter is determined by matching to the total number, $N_{c\bar{c}}$, of $c\bar{c}$ pairs in the system,

$$N_{c\bar{c}} = \frac{1}{2} N_{op} \frac{I_1(N_{op})}{I_0(N_{op})} + V_{FB} \gamma_c^2 \sum_{\eta_c, J/\psi, \dots} n_\Psi^{\text{eq}}(T) , \quad (53)$$

where N_{op} denotes the number of all open-charm states in a fireball of volume V_{FB} . In a QGP, where the charm-quark number is carried by deconfined c -quarks, one has $N_{op} = V_{FB} \gamma_c 2n_c^{\text{eq}}(m_c^*, T)$, whereas in the HG, $N_{op} = V_{FB} \gamma_c \sum_\alpha n_\alpha^{\text{eq}}(T, \mu_B)$ with α running over all known charmed hadrons ($D, \bar{D}, \Lambda_c, \dots$; note that for a finite baryon chemical potential $N_{\Lambda_c} \neq N_{\bar{\Lambda}_c}$ implying $N_D \neq N_{\bar{D}}$, etc.). The ratio of modified Bessel functions, I_1/I_0 , in Eq. (53) approaches one for large N_{op} , but goes to $0.5N_{op}$ for $N_{op} \ll 1$, representing the probability of producing an extra (anti-) charm state, i.e., it enforces exact charm conservation in the canonical ensemble (c and \bar{c} can only be produced together) [120]. Note that the charmonium equilibrium limit does not depend on nuclear absorption or pre-equilibrium effects. The QGP evolution prior to hadronization is, however, imprinted on the collective properties of the statistically produced charmonia, i.e., their p_t spectra and elliptic flow [128, 123, 124]. In fact, if the c - \bar{c} coalescence does not occur in equilibrium, the pertinent charmonium spectra reflect on the collective properties of the charm quarks, which, in turn, may serve as an additional means to identify a coalescence component in the spectra [123, 129]. In Refs. [23, 65], a 2-component model has been proposed where statistical production at hadronization is combined with primordially produced charmonia subject to suppression in the QGP, followed by hadronic suppression of both components.

Solutions of the transport equation (50) for J/ψ production in heavy-ion collisions under inclusion of the gain have first been evaluated in Ref. [22]; neglecting spatial dependencies in the temperature profile as well as in the J/ψ and open-charm densities, a simplified rate equation of the form

$$\frac{dN_{J/\psi}}{d\tau} = \lambda_F N_c n_{\bar{c}} - \lambda_D N_{J/\psi} n_g , \quad (54)$$

has been employed, very similar to Eq. (20). The reactivity $\lambda_D = \langle v_{\text{rel}} \sigma_D \rangle$ is given in terms of the J/ψ dissociation cross section, for which the gluo-dissociation process, Eq. (22), has been used (and detailed balance for the formation reactivity, λ_F). As emphasized in Ref. [22] (as well as in the statistical models with charm conservation [21, 120]), the J/ψ formation rate depends quadratically on the number, $N_{\bar{c}c}$, of (anti-) charm quarks in the system, rendering an accurate knowledge of the charm-production cross section an essential ingredient for reliable predictions of charmonium regeneration. In the equilibrium

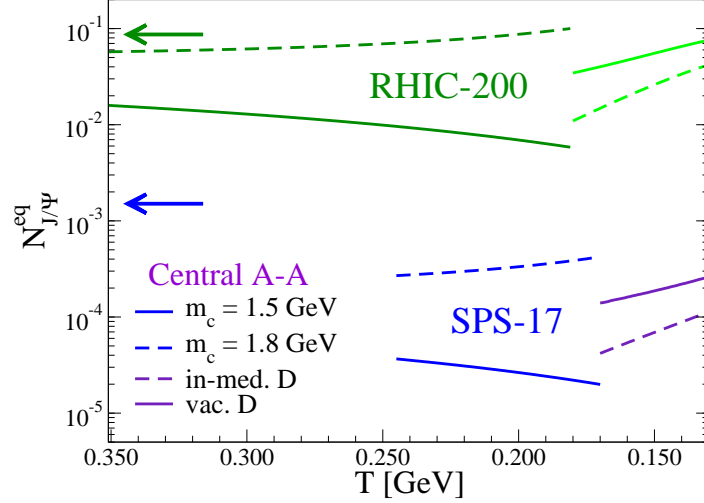


Figure 31: Equilibrium abundance of J/ψ mesons as a function of temperature in an isotropic fireball representative for central Pb–Pb and Au–Au collisions at SPS and RHIC, respectively [17]. While the variation in temperature is comparatively moderate, a large sensitivity of the equilibrium numbers with respect to even moderate variations in the charm-quark (charm-hadron) masses in the QGP (hadron gas) is found. The absolute numbers are obtained using open-charm cross sections as measured in pp collisions ($\sigma_{pp}^{c\bar{c}}=5.5, 570 \mu\text{b}$ at SPS, RHIC), extrapolated to central A–A reactions using binary-collision scaling, and for a rapidity interval of 3.6 units around midrapidity (corresponding to 2 thermal fireballs). The arrows to the left indicate the J/ψ abundance from primordial (hard) production.

limit, the quadratic dependence is encoded in the squared fugacity factor in the charmonium densities, Eq. (52). As elaborated in Refs. [130, 17], the equilibrium limit of the J/ψ abundance is rather sensitive to the masses of both open- and hidden-charm states (cf. also Ref. [131]). E.g., for fixed charmonium masses, a reduced charm-quark mass in the QGP (or reduced charm-hadron masses in the HG) implies a reduced γ_c for fixed $N_{c\bar{c}}$, which in turn leads to a smaller N_{ψ}^{eq} ; in other words, reduced (increased) open-charm masses make it thermodynamically more (less) favorable to allocate a given number of $c\bar{c}$ pairs into open-charm states rather than into charmonia, see Fig. 31. This interplay has been quantitatively worked out in Ref. [17] based on the rate equation (20) with in-medium charm-quark and -hadron masses in QGP and HG phases, respectively. In particular, $m_c^*(T_c) \simeq 1.6 - 1.7 \text{ GeV}$ on the QGP side has been chosen to provide a continuous transition of γ_c into the hadronic phase at the (pseudo-) critical temperature (note that this range of c -quark masses is somewhat below the value of $m_c^*(T_c) \simeq 1.8 \text{ GeV}$ as inferred from the lattice correlator analysis using the internal energy as the heavy-quark potential, recall Fig. 13). As discussed in Sec. 2.2, the screening of lattice-based potentials leads to reduced binding energies, while the in-medium change in the J/ψ mass is expected to be rather small. The latter is then stabilized by a decrease in the in-medium charm-quark mass m_c^* , as seems to be required in potential-model analyses of lattice QCD correlators. In Ref. [70], the rate equation approach of Ref. [17], which was restricted to inclusive charmonium production (i.e., for $p=0$), has been extended to finite 3-momentum. The suppression part has been treated explicitly (including spatial dependencies, such as leakage effects) in an expanding fireball background, whereas the momentum dependence of the regeneration part was approximated with a blast wave model (within the same fireball), implying that the underlying charm-quark spectra are thermalized, at least in the relevant regime of low momentum [122, 132].

A more advanced treatment of the gain term in the rate equation (50) within a hydrodynamically evolving background medium was carried out in Ref. [124] (see also Ref. [133]). Assuming the prevalence

of the $2 \leftrightarrow 2$ dissociation rates from gluodissociation, $g + \Psi \leftrightarrow c + \bar{c}$, the gain term takes the form

$$\beta_{\Psi}(\vec{p}_t; \vec{r}_t, \tau) = \frac{1}{2E_{\Psi}} \int \frac{d^3k}{(2\pi)^3 2\omega_k} \frac{d^3p_c}{(2\pi)^3 2\omega_{p_c}} \frac{d^3p_{\bar{c}}}{(2\pi)^3 2\omega_{p_{\bar{c}}}} f^c(\vec{p}_c; \vec{r}_t, \tau) f^{\bar{c}}(\vec{p}_{\bar{c}}; \vec{r}_t, \tau) W_{c\bar{c}}^{g\Psi}(s) \Theta(T(\vec{r}_t, \tau) - T_c) \times (2\pi)^4 \delta^{(4)}(p + k - p_c - p_{\bar{c}}), \quad (55)$$

where the charmonium phase space has been restricted to the transverse plane at central rapidity ($p_z=0$). With $W_{g\Psi}^{c\bar{c}}(s) = \sigma_{g\Psi}^{\text{diss}} v_{\text{rel}}(2\omega_k 2E_{\Psi})$ representing the Ψ dissociation probability, the formation probability, $W_{c\bar{c}}^{g\Psi}(s)$, is inferred from detailed balance. ω_k , E_{Ψ} , ω_{p_c} and $\omega_{p_{\bar{c}}}$ denote the on-shell energies of gluon, charmonium, charm and anticharm quark, respectively, with charm(onium) masses of $m_c=1.87$ GeV and $m_{J/\psi}=3.1$ GeV. The $\Theta(T - T_c)$ function in Eq. (55) restricts the inelastic processes to the QGP phase, with $T_c=165$ MeV in Ref. [124]. Note that an explicit treatment of NLO dissociation processes in the regeneration term would require the evaluation of a 3-body initial state. The initial conditions for the charmonium distribution function, $f^{\Psi}(\vec{p}; \vec{r}, \tau_0)$, for their evolution in the thermally evolving medium are typically taken from a Glauber collision profile for production in primordial N - N collisions, plus the effects of nuclear absorption. In the “pre-equilibrium” phase, i.e., for times earlier than the thermalization time, τ_0 , of the fireball, the gain term is switched off. While the production of a $c\bar{c}$ is expected to occur on short time scale, $\tau_{c\bar{c}} \sim 1/2m_c \simeq 0.1$ fm/ c , the development of the charmonium wave function in its rest frame requires a time duration on the order of its inverse binding energy, $\tau_{\Psi} \sim 1/\varepsilon_B \simeq 0.35$ fm/ c . For a slowly moving J/ψ , this time is comparable or smaller to commonly assumed thermalization times of 0.3-1 fm/ c . However, for J/ψ 's at large transverse momentum, the formation time in the fireball frame is time-dilated by the (transverse) Lorentz factor $\gamma_t = m_t/m$, and therefore may well reach into the QGP phase, presumably reducing the suppression effects [134, 135, 136, 138, 139, 115] (in a naive picture, the $c\bar{c}$ wave package is of smaller size than a fully formed bound state, thus reducing dissociation cross sections with thermal partons). The interplay of charmonium-formation and fireball-thermalization time scales will be further pronounced for in-medium reduced binding energies, as well as for excited charmonia (which even in vacuum have rather small binding energies).

An alternative approach to thermal descriptions of the bulk medium are microscopic transport models where the evolution of essentially all particle distributions is treated by numerical simulations of the Boltzmann equation. On the one hand, transport models have the important advantage that no explicit assumption on equilibration is required, which in particular eliminates the introduction of thermalization and freezeout times (or conditions)³. On the other hand, the treatment of phase transitions is much more problematic than in thermal models, where the pertinent aspects are readily encoded in the equation of state (EoS). The main input for charmonium interactions are $2 \leftrightarrow 2$ dissociation reactions (plus detailed balance), i.e., gluo-dissociation ($g + \Psi \rightarrow c + \bar{c}$) in the partonic phase and meson dissociation ($M + \Psi \rightarrow D + \bar{D}$ with $M=\pi, K, \rho, \dots$) in the hadronic phase (sometimes augmented with elastic cross section). Especially hadronic cross sections at low energy, as relevant for the typical reactions in the hadronic phase (corresponding to temperatures $T < 200$ MeV), are currently beset with rather large theoretical uncertainties (and, in the case of meson dissociation, not accessible experimentally), recall Sec. 2.4. This problem is, of course, germane to both transport and thermal descriptions of the expanding medium. Systematic comparisons of charmonium observables within complementary descriptions of the bulk medium are thus a valuable means to extract robust information on charmonium properties in heavy-ion collisions. Recent calculations of charmonium production within transport models, including regeneration reactions, can be found in Ref. [140, 141, 142], and will be reiterated in the context of heavy-ion data in Sec. 3.3. E.g., in Ref. [140], it was found that an increase in the masses of open-charm states (c -quarks and D -mesons in the partonic and hadronic phase, respectively) entails an enhanced J/ψ production, which is consistent with the systematics of the thermal model as illustrated in Fig. 31.

³Much like for charmonia, primordial particle production in hadronic transport models account for a formation time, $\tau_F^h \simeq 1/\Lambda_{\text{QCD}} \simeq 0.5 - 1$ fm/ c , in the rest frame of the hadron.

In Ref. [143], the uncertainty in meson-induced dissociation reactions was circumvented by introducing a single matrix element for the all dissociation reactions, augmented by spin-isospin factors and phase space factors (subsequently used in Refs. [141, 142]). In a similar spirit, the hadronic comover model [113] has recently been extended to include regeneration reactions [144].

3.2 Nuclear Absorption and Pre-Equilibrium Effects

A strategy to isolate cold nuclear matter (CNM) effects, encoded in the suppression factor S_{nuc} in Eq. (51), on the production of heavy quarkonia in heavy-ion collisions is to study the A -dependence of these processes in p - A collisions relative to pp collisions. The presence of CNM affects quarkonium formation during three different stages: (1) *initial state* prior to $Q\bar{Q}$ production by gluon fusion due to the modification of the gluon distribution function, (2) *formation stage* of the quarkonium spectrum from the initial $Q\bar{Q}$ pair and (3) *final state* inelastic interactions leading to quarkonia absorption in the CNM of the target. It is at present an open problem how to disentangle these three CNM effects from the experimental results for the A -dependence measured in p - A collisions. To obtain a baseline for predictions, it is assumed that absorption is the dominant process and may be analyzed according to the Glauber model as

$$\sigma_{pA \rightarrow \psi} = \sigma_{pp \rightarrow \psi} \int d^2b \int_{-\infty}^{\infty} dz \rho_A(b, z) \exp \left\{ - \int_z^{\infty} dz' \rho_A(b, z') \sigma_{\text{abs}}(z' - z) \right\}, \quad (56)$$

where b is the impact parameter and $\rho_A(b, z)$ is the nuclear density profile. The exponential factor measures the probability for the $c\bar{c}$ pair to escape nuclear absorption and to form a J/ψ where σ_{abs} is a “convoluted” J/ψ absorption cross section parametrizing the combined result of all CNM effects.

Taking as an example a spherical nucleus with $\rho_A(b, z) = 3/(4\pi r_0^3) \Theta(r_0 - \sqrt{b^2 + z^2})$, let us illustrate [2] how the nuclear absorption cross section can be extracted from experimental data for the A -dependence of J/ψ production, starting from a commonly employed parameterization of the form

$$\sigma_{pA \rightarrow \psi} = \sigma_{pp \rightarrow \psi} A^\alpha. \quad (57)$$

Expanding the exponential in (56), keeping only linear terms in σ_{abs} , integrating over the nuclear volume and then reexponentiating, one obtains

$$\frac{\sigma_{pA \rightarrow \psi}}{\sigma_{pp \rightarrow \psi}} \approx \exp \left\{ - \frac{9\sigma_{\text{abs}} A^{1/3}}{16\pi r_0^2} \right\} \equiv \exp(-\eta A^{1/3}). \quad (58)$$

For targets with $A > 50$, one has $A^{1/3} \approx \ln A$, and in this case the relationship between σ_{abs} and α is

$$\sigma_{\text{abs}} = \frac{16\pi r_0^2}{9} (1 - \alpha). \quad (59)$$

Recent experimental analyses at fixed target energies result in $\sigma_{\text{abs}} = 4.0 \pm 1.6$ mb deduced from a range of $\alpha = 0.95 \pm 0.02$, see left panel of Fig. 32. The values of α at $x_F \approx 0$ (relevant for heavy-ion collision experiments) increase with collision energy. Since the scaling of α with p_T (middle panel of Fig. 32) is independent of energy, the increase might originate from the increase of the average p_T with collision energy, see right panel of Fig. 32. From three different NA50 data sets [147] a Glauber model fit gave a convoluted nuclear absorption cross section $\sigma_{\text{abs}} = 4.2 \pm 0.5$ mb (left panel of Fig. 33). However, one has to keep in mind that only about 60% of the observed J/ψ mesons are directly produced, while about 30% (10%) come from χ_c (ψ') feeddown. If one calculates $\sigma_{\psi N}$ geometrically, as πr^2 , with $r_{J/\psi} = 0.25$ fm, $r_{\psi'} = 2 \times r_{J/\psi}$ and $r_{\chi} = 0.25 = 1.5 r_{J/\psi}$, and redo the Glauber-model calculation, an equally acceptable description of the A -dependence is obtained, see the right panel of Fig. 33. This reasoning would point to smaller absorption cross section for the J/ψ on nucleons, on the order of 2 mb. Within a quantum

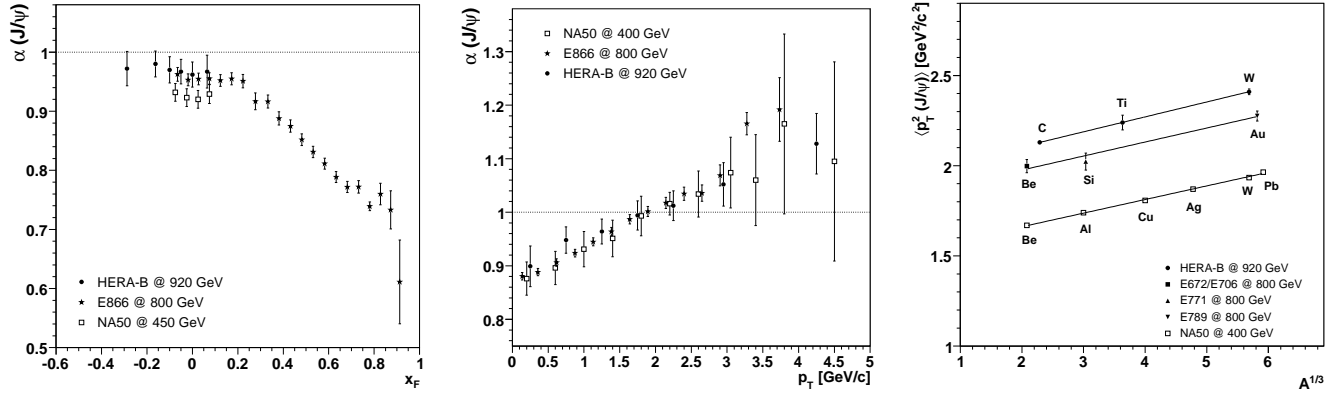


Figure 32: The nuclear-dependence parameter α as a function of x_F (left) and of p_T (middle), for J/ψ mesons measured at three different collision energies, in p-A collisions. The measure for p_T broadening (Cronin effect), $\langle p_T^2 \rangle$, increases with nuclear target size and with collision energy (right); from Refs. [145, 146, 147, 148].

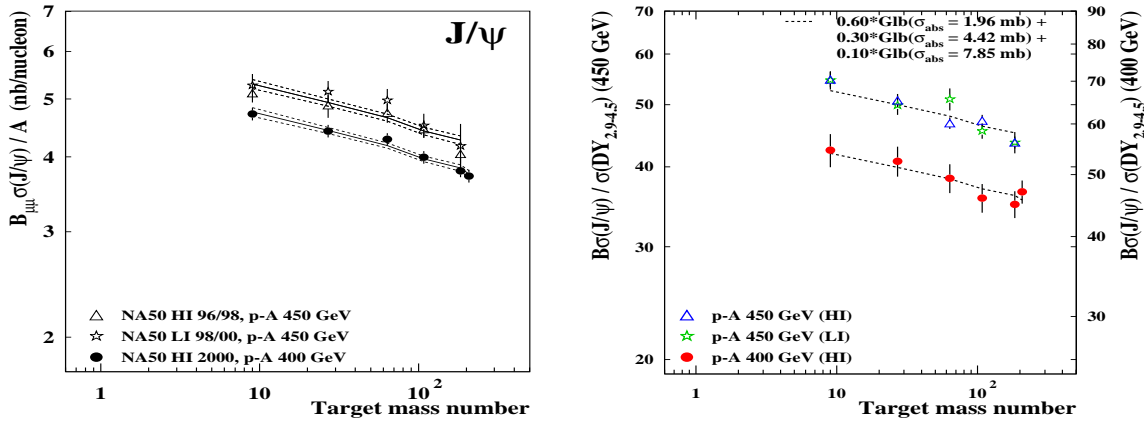


Figure 33: Left panel: J/ψ cross section in p-A collisions from three different NA50 data sets [147] together with a Glauber fit of a convoluted nuclear absorption cross section $\sigma_{\text{abs}} = 4.2 \pm 0.5$ mb; right panel: A-dependence of the J/ψ over DY cross section ratio, compared to a Glauber model calculation taking into account feed-down from higher $c\bar{c}$ states [149].

mechanical description of the formation of charmonia from an initially small-sized “pre-meson” state, the authors of Ref. [150] have derived an energy and time-dependent cross section of ~ 3 mb for the pre-meson at $\sqrt{s} = 10$ GeV in the initial state. For asymptotic times, at $t \rightarrow \infty$, they deduce total cross sections of $\sigma_{J/\psi N} = 2.8 \pm 0.3$ mb and $\sigma_{\psi' N} = 10.5 \pm 3.6$ mb from E866 data, in accordance with the geometric scaling, thus resolving the puzzle of an apparent discrepancy between the σ_{abs} values extracted from hadro- and photoproduction data. A characteristic feature of the quantum mechanical treatment of charmonium formation in p -A (also applicable to AA) collisions [151, 152, 153, 154] is the possibility for an oscillatory behavior of the survival probability with time, most pronounced for the ψ' . This is different from the classical picture of a $c\bar{c}$ state expanding in time [155, 156, 157, 158] and could eventually be tested via detailed kinematic (e.g. x_F) dependencies of production cross sections [154].

Let us now turn to the discussion of CNM effects in parton distribution functions (PDFs), $f_i^A(x, Q^2)$, characterized by the ratio

$$R_i^A(x, Q^2) = f_i^A(x, Q^2)/f_i^p(x, Q^2), \quad (60)$$

see, e.g., Ref. [161]. The left panel of Fig. 34 shows this ratio for a lead nucleus within the EKS 98 parametrization [159, 160], for two values of the momentum transfer, $Q^2 = 4(50)$ GeV², appropriate for

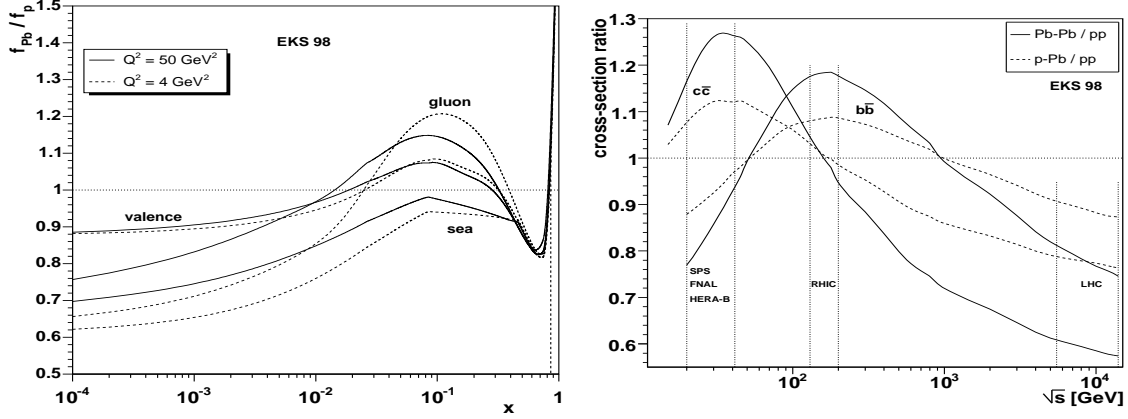


Figure 34: Left panel: Nuclear modifications of gluon PDFs for a Pb nucleus, according to the EKS 98 [159, 160] weight functions; right panel: changes of the $c\bar{c}$ and $b\bar{b}$ cross sections induced by the nuclear modifications of the PDFs, at mid-rapidity.

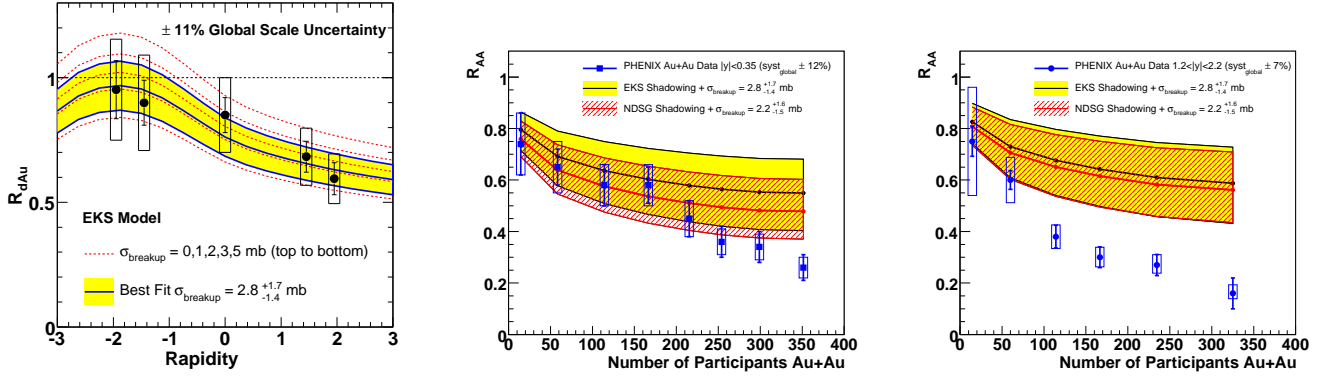


Figure 35: Left panel: PHENIX data for the nuclear modification factor R_{dAu} as a function of rapidity compared to theoretical curves using the EKS shadowing model [159, 160] for different values of the nuclear absorption cross section σ_{abs} ($\sigma_{breakup}$). Best fit from these data is $\sigma_{abs} = 2.8^{+1.7}_{-1.4}$ mb. Middle panel: R_{AA} for Au+Au collisions at mid-rapidity compared to projections of cold nuclear matter effects extrapolated from the d+Au data, for the EKS and the NDSG [162] shadowing. Right panel: R_{AA} at forward rapidity; from Ref. [163]

$c\bar{c}$ ($b\bar{b}$) production. Relevant values for the Bjorken variable, $x = M e^y / \sqrt{s}$, at central rapidity ($y = 0$) and for charm (bottom) production, $M = 1.5(5)$ GeV, are in the range of $0.01 < x < 0.5$ from SPS to Fermilab energies ($200 < E_{lab} < 920$ GeV), corresponding to $\sqrt{s} = 20 - 40$ GeV. Of particular interest are gluons, which are expected to dominate the production cross section for $Q\bar{Q}$ pairs via the two-gluon fusion process (except for close to the production threshold). Typical nuclear effects are: (a) shadowing at low x , where $R^A(x, Q^2) < 1$, (b) anti-shadowing at intermediate x , where $R^A(x, Q^2) > 1$, (c) EMC effect at $0.25 < x < 0.8$, where $R^A(x, Q^2) < 1$, and (d) Fermi motion at $x \approx 1$, where $R^A(x, Q^2) > 1$. The right panel of Fig. 34 indicates a 10% $c\bar{c}$ production cross section enhancement at midrapidity for SPS energies, while there is no effect at RHIC. On the other hand, d-Au collisions at backward rapidities ($y = -2.0$) at RHIC, a 15% antishadowing is predicted, compared to 20% shadowing at forward rapidities ($y = 2.0$, in the direction of the Au beam). Based on EKS 98 PDFs, a best fit to PHENIX data for the y dependence of the nuclear modification factor, R_{dAu} , results in a nuclear absorption cross section of $\sigma_{abs} = 2.8^{+1.7}_{-1.4}$ mb, see left panel of Fig. 35. Although the error bars are still quite large, the mean value agrees nicely with the absorption cross section of the premeson state in the

quantum mechanical approach of Ref. [150] and a recent systematic study of J/ψ suppression in CNM [164].

The extrapolation of the CNM effects analyzed in d-Au collisions to Au-Au collisions is shown in Fig. 35 for midrapidity (middle panel) and forward rapidity (right panel) in comparison to PHENIX data [163]. While at forward rapidity the onset of non-CNM effects appears at $N_{\text{part}} \approx 70$, in rough agreement with the onset of anomalous suppression in the NA50 experiment, there is almost no deviation from the CNM extrapolation at midrapidity, even for the most central collisions. This counter-intuitive result points to the existence of an additional J/ψ production process which is predominantly operative in the central rapidity region. In the previous Subsection, charm recombination in the medium has been discussed as a gain processes in the kinetic equation for charmonium production. Its role in the interpretation of present and future experiment will be discussed quantitatively in the following Subsection.

3.3 Applications at SPS, RHIC and LHC

In this section we attempt to convert the recent theoretical and phenomenological developments described above (charmonium equilibrium properties as well as implementations into transport approaches) into interpretations of available data from ultrarelativistic heavy-ion collisions (URHICs) at SPS and RHIC. As a rough guideline, let us start by recalling some of the basic relations which have been proposed to associate different observables with key properties of charmonia in medium.

- (A) Centrality dependence of J/ψ production, which is typically normalized to the expected yield in the absence of any medium effects, $R_{AA}(N_{\text{part}})$ – based on an increasing matter density with centrality (i.e., decreasing impact parameter), this is the classic observable to search for an anomalous suppression of charmonia possibly linked with the onset of QGP formation.
- (B) Transverse-momentum (p_t) spectra, normalized to the expected spectra without medium effects (i.e., in pp collisions), $R_{AA}(p_t)$ – here, the original objective is the extraction of the p_t dependence of the charmonium dissociation rates. However, in the presence of regeneration contributions, p_t -spectra are expected to be softer than the primordial power-law spectra, which provides a particularly valuable handle to disentangle secondary and direct production. The discrimination power is further augmented in the elliptic flow, $v_2(p_t)$.
- (C) Excitation function – the suppression effect of primordial charmonia is expected to increase with increasing collision energy, providing complementary information on the temperature and density dependence of charmonium disintegration (in addition to centrality dependencies at fixed energy). However, the possibly largest virtue of an excitation function is the substantially stronger increase in charm-quark production compared to light particles, leading to a large variation in the charm-quark densities in the fireball which (quadratically) enhances regeneration mechanisms with increasing energy. The excitation function thus promises to be a prime observable to study the interplay of suppression and regeneration mechanisms.
- (D) Rapidity dependence – the idea behind this observable is reminiscent to (C) in that light- and charm-quark production are characterized by different rapidity distributions (narrower for heavy quarks); regeneration, being proportional to $N_{c\bar{c}}^2$ (at least in the grand-canonical limit), should thus lead to a narrowing of the charmonium distributions compared to pp collisions.
- (E) Excited charmonia (χ_c , ψ') – different binding energies, dissociation rates and dissolution temperatures are hoped to provide a systematic suppression/production pattern that can serve as a “thermometer” upon varying control parameters such as centrality, system size and collision energy (all of the J/ψ observables listed under (A)-(D) apply here).

- (F) Bottomonia – due to stronger binding energies, bottomonium suppression could provide a more sensitive measure of color screening and an associated increase in dissociation rates. This hope is further fueled by the much smaller open-bottom cross section which presumably suppresses bottomonium regeneration.

It is furthermore important to realize that feeddown contributions via the decays of excited charmonia into lower lying ones need to be considered, especially for the J/ψ : about 1/3 of its inclusive production yield in pp collisions arises from decays of originally produced χ_c states [165], and $\sim 7\text{--}8\%$ from ψ' states [166]. Such a large fraction cannot be neglected in quantitative calculations of J/ψ observables in heavy-ion reactions, rendering a simultaneous and consistent treatment of medium effects on χ_c (and possibly ψ') production mandatory. At high $p_t > 5$ GeV, relevant for collider energies, the inclusive J/ψ yield is expected to receive additional feeddown contributions from B -meson decays, on the order of 20–40% [167].

In the remainder of this Section we discuss the 6 classes of observables in the order given above, focusing on the most recent status and developments, and with preference for approaches which have been applied at both SPS and RHIC energies.

3.3.1 Centrality Dependence

Let us start our discussion with the inclusive centrality dependence of J/ψ production at SPS energies, specifically with implementations of the J/ψ transport equation into a thermally expanding background medium.

In Ref. [168] the gluo-dissociation rates for J/ψ and χ_c (using vacuum binding energies) have been folded over 2+1 hydrodynamic evolution of Pb(158 AGeV)–Pb collisions, employing an EoS consisting of a 2+1 flavor QGP and a hadron resonance gas (connected via a mixed phase at $T_c \simeq 165$ MeV). Hadronic suppression of the J/ψ and regeneration effects (expected to be small at SPS energies due to small open charm production) have been neglected. The primordial nuclear absorption cross section has been fixed at $\sigma_{\text{abs}} = 4.3$ mb in line with the most recent p –A data. The overall magnitude of the suppression in the NA50 data has been reproduced by introducing a minimal initial entropy density of $s_{\text{min}} \simeq 32 \text{ fm}^{-3}$, below which the matter is assumed to decouple instantaneously (i.e., not to become part of the thermally evolving medium); with a formation time of $\tau_0 = 0.8 \text{ fm}/c$, the centrality dependence of the J/ψ yield (upper left panel of Fig. 36), as well as its average momentum squared (lower left panel), are well reproduced. Within a similar spirit, but adopting a slightly different approach, solutions of the rate equation (20) have been evaluated in Refs. [17, 70]. The thermal evolution of the medium has been treated in a more simplistic isotropic fireball expansion, parametrized to resemble hydrodynamic models and employing an EoS with QGP-mixed-hadronic phases at $T_c = 170(180)$ MeV at SPS (RHIC), similar to Ref. [168]. The inelastic charmonium reactions in the QGP include an in-medium reduction of the binding energies, incorporated using the quasifree dissociation process [23] (rather than gluo-dissociation, recall Fig. 16), corresponding to the rates displayed in the right panel of Fig. 17. The dissociation rates in the hadronic phase have been estimated based on $SU(4)$ effective theory, leading to rather small effects in particular on the J/ψ (somewhat more significant for χ_c and ψ'). Fixing $\sigma_{\text{abs}} = 4.4$ mb and $\tau_0 = 1 \text{ fm}/c$ (translating into $\bar{T}_0 \simeq 210$ MeV in central Pb–Pb), the coupling constant in the quasifree process has been adjusted to $\alpha_s \simeq 0.25$ to fit the suppression in central Pb–Pb. Also here the centrality dependence of inclusive J/ψ production and its mean $\langle p_t^2 \rangle$ are well described. The contribution from regeneration turns out to be small.

Hadronic comover-interaction [113] and transport [169] models have also been rather successful in describing the J/ψ suppression pattern observed by NA50. With a typical comover dissociation cross section of 0.65–1 mb, the required comover energy densities in central Pb–Pb are rather large, (well) above the typical value of 1 GeV/fm³ associated with the phase transition. The comover interaction is thus to be understood to be at least partially of partonic origin (as is, in fact, suggested by the rather

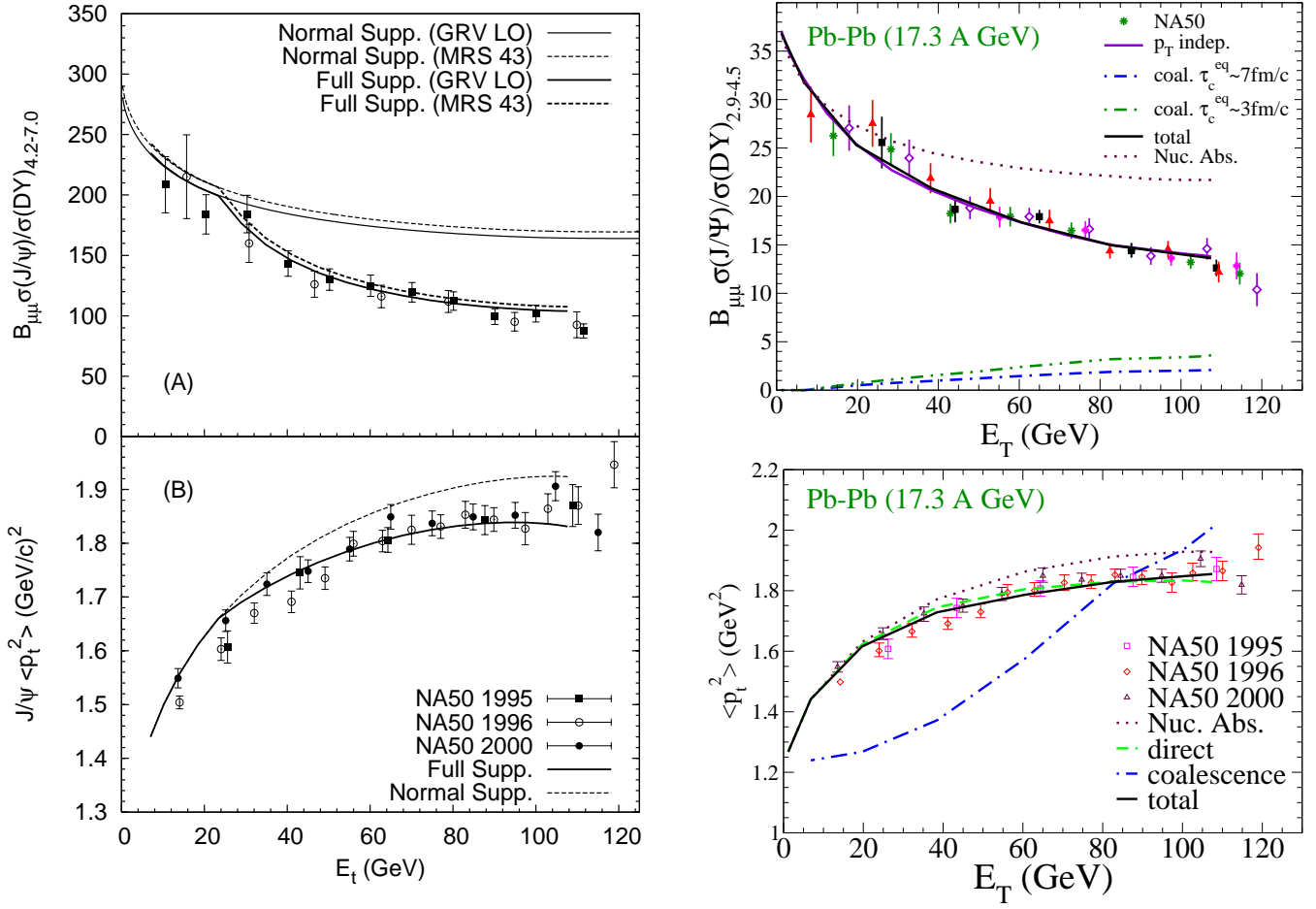


Figure 36: J/ψ production in Pb–Pb collisions at SPS employing the rate equation (50) within a hydrodynamic evolution with gluon dissociation in the QGP (left panels, gain term neglected) [168] or an expanding thermal fireball with quasifree dissociation in the QGP and meson-induced break-up in the hadronic phase (right panels) [17, 70]. Upper panels: nuclear modification factor as function of centrality quantified by the measured transverse energy, E_T , of produced particles; lower panels: centrality dependence of the average transverse momentum squared of the J/ψ spectra.

small value of the dissociation cross section). In the hadronic transport calculations of Ref. [169], the hadronic comover interactions are significantly larger (a few millibarns for baryon-induced dissociation, and 2/3 of that for mesons), but “pre-hadronic” degrees of freedom still play a role.

An often discussed issue in the interpretation of the NA50 data is the (non-) presence of a threshold behavior in mid-central Pb–Pb collisions, around $E_T \simeq 30 - 40$ GeV. To address this question experimentally, the successor experiment NA60 has measured J/ψ production for an intermediate-size system, i.e., In–In collisions. The pertinent data are compared theoretical *predictions* in the left panel of Fig. 37, all 3 of which are in reasonable agreement with the Pb–Pb data. While the comover model [172] and the threshold-melting scenario [170] do not reproduce the data, the thermal rate equation approach in QGP + hadronic phase [17, 171] shows a fair agreement (except for central collisions where the data suggest a reduced suppression). The suppression pattern at SPS energies has been revisited within the Hadron String Dynamics (HSD) transport model in Ref. [141], where charmonium suppression was studied within the QGP threshold-melting scenario (middle panel of Fig. 37) and a comover-interaction model (right panel of Fig. 37). The former is characterized by critical energy densities above which the

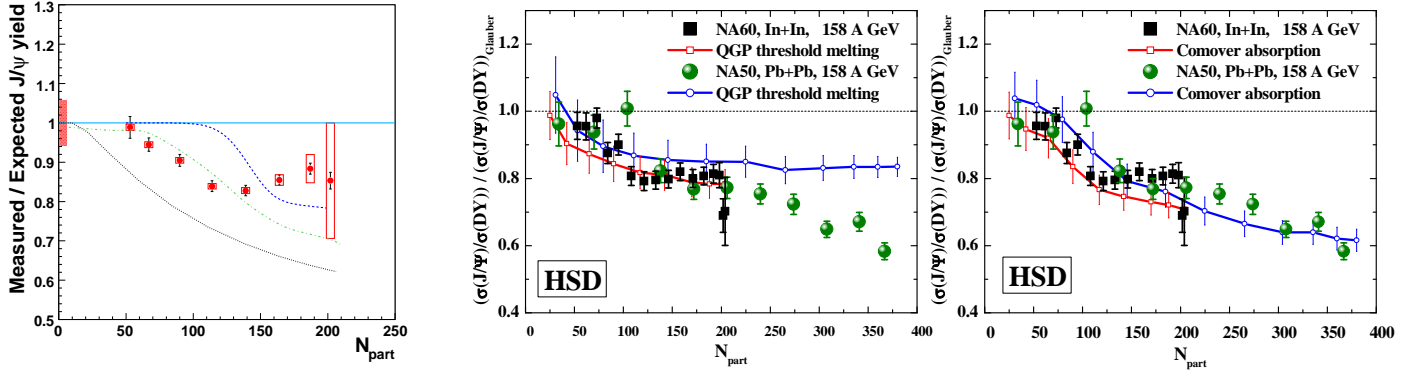


Figure 37: Left panel: NA60 data for J/ψ production in In(158 A GeV)–In collisions at SPS energies [176] compared to theoretical predictions based on (a) QGP threshold-suppression scenario [170] (upper dashed line), (b) QGP and hadronic suppression in a thermal fireball [171] (middle dashed-dotted line), and (c) comover model [172] (lower dotted line); all models are in fair agreement with NA50 data in Pb–Pb collisions. Middle and right panels: postdictions for Pb–Pb [173] and In–In [174] data computed in the HSD transport model [141] using either a QGP threshold-melting scenario (middle panel) or comover model (right panel); note that the NA60 data are the preliminary ones from Ref. [174].

corresponding state does not form⁴, while the latter has been implemented via a single matrix element for all charmonium states (including phase space and spin effects). It has been concluded that the SPS data compare well with comover scenario, while the threshold-melting scenario does not allow for a consistent description. Note that the level of agreement of the HSD+comover scenario with NA60 data is quite comparable to the thermal rate-equation prediction [17, 171] in the left panel of Fig. 37 (in the literature [175, 141, 176] the latter is often interpreted as not reproducing the NA60 data).

Let us now turn to RHIC energies, focusing on the approaches discussed above in the SPS context. The hydrodynamic model with gluo-dissociation has been extended to include regeneration reactions, $c + \bar{c} \rightarrow g + \Psi$ in Ref. [124]. The charm-quark distributions figuring into the gain term, eq. (55), have been approximated by two limiting scenarios: (a) primordial spectra in pp given by perturbative QCD (pQCD), or (b) fully thermalized spectra including the collective flow of the hydrodynamic background. The corresponding difference in the inclusive J/ψ yields turns out to be rather small, cf. the upper left-hand panels in Fig. 38. With an underlying open-charm production cross section of $\sigma_{pp}^{c\bar{c}} = 622 \pm 57 \mu\text{b}$ (as measured by PHENIX [126], and scaled by the number of binary N - N collision at given impact parameter), the overall magnitude of the (preliminary) PHENIX data [177] is reasonably well described. The contribution from regeneration is moderate but significant, reaching up to 50% of the total yield in central Au–Au. The upper right panel of Fig. 38 shows updated calculations of the thermal rate-equation approach [17], extended to include the finite 3-momentum dependence of the inelastic charmonium reaction rates [70]. Here, the impact of incomplete charm-quark thermalization has been schematically modeled by a “thermal relaxation time” factor, $\mathcal{R}(\tau) = 1 - e^{-\tau/\tau_c}$, multiplying the charmonium equilibrium abundance, N_{Ψ}^{eq} , which figures into the gain term of the rate equation (21). This implementation leads to a stronger dependence of the regeneration yield on charm-quark equilibration than in Ref. [124]; the original predictions of Ref. [17] were done with $\tau_c = 3 \text{ fm}/c$ (and $\sigma_{pp}^{c\bar{c}} = 570 \mu\text{b}$ [65], in line with recent PHENIX data [195]), which somewhat overestimates the J/ψ yield in central Au–Au as compared to the most recent PHENIX measurement [20] (cf. dashed double-dotted line in the upper right panel of Fig. 38). Using $\tau_c = 5\text{--}7 \text{ fm}/c$ [70] improves the agreement leading to results which are quite consistent with the ones shown in the left upper panels [124]. HSD calculations at RHIC based on suppression-only scenarios (comover or threshold melting) [142] underpredict existing

⁴It may be thought of as a sudden transition of the quarkonium width from zero to infinity.

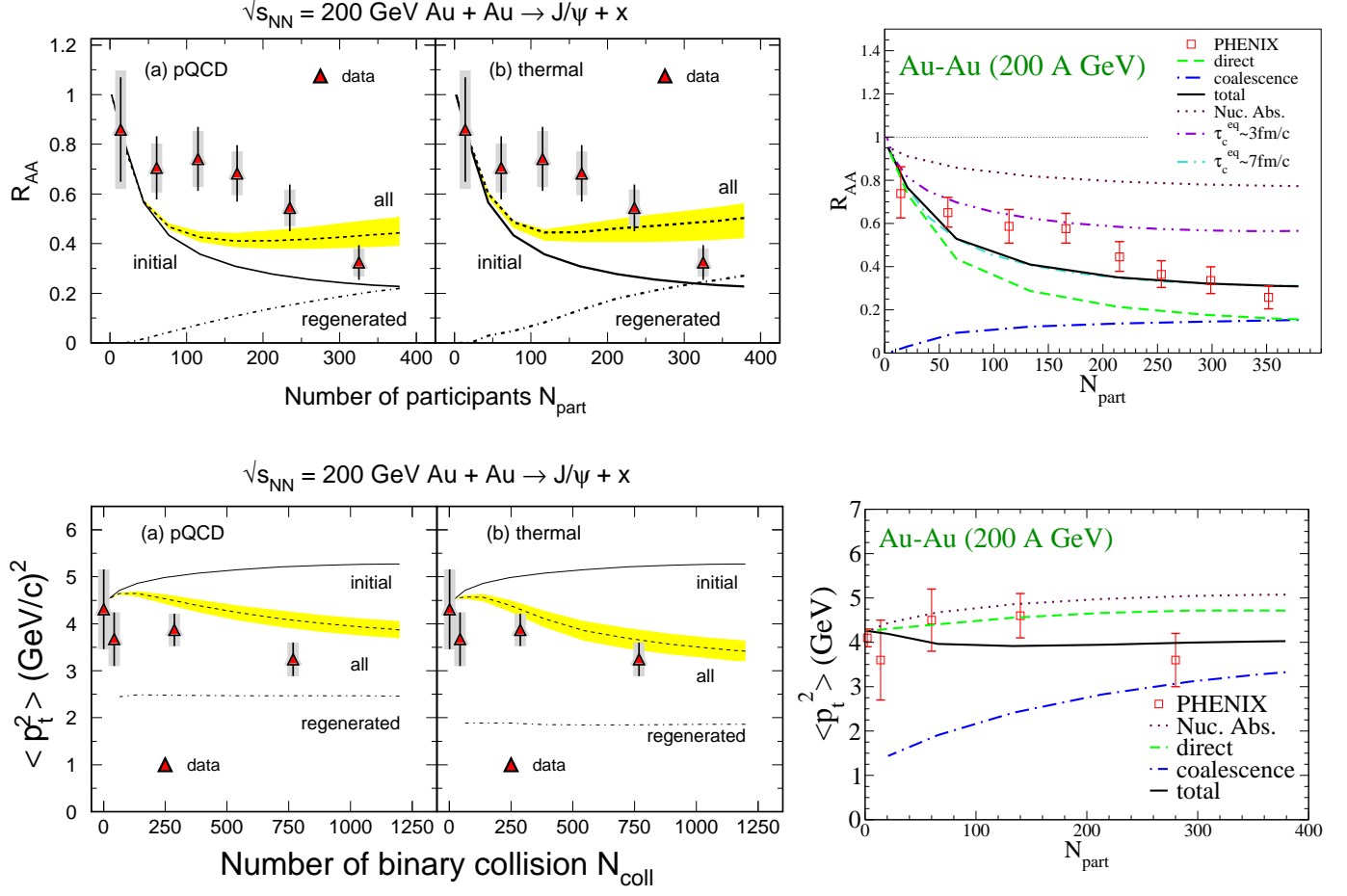


Figure 38: J/ψ production in Au–Au collisions at RHIC computed within kinetic rate equations in a thermally evolving background medium, corresponding to the approaches confronted with SPS data in Fig. 36 (left panels: gluo-dissociation with vacuum binding energies in a hydrodynamic simulation [168, 124], right panels: quasifree dissociation with in-medium binding energies in a thermal fireball expansion [17, 70]). The upper panels show the nuclear modification factor, $R_{AA}^{J/\psi}(N_{part})$ vs. centrality for inclusive J/ψ yields, while the lower panels display the centrality dependence of the J/ψ 's average momentum squared. The (preliminary) data in the right (left) panel are from Ref. [20] ([177]).

PHENIX data, thus supporting the presence of a regeneration component.

It is important to realize that the J/ψ regeneration yield is rather sensitive to the open-charm content of the system. First and foremost, this pertains to the number of charm-anticharm pairs, $N_{c\bar{c}}$, in the system. In the grand-canonical limit, $N_{op} \gg 1$, the charmonium equilibrium number depends quadratically on $N_{c\bar{c}}$. But even at SPS energies, where charm-quark production is small and the canonical limit applies (implying that N_{Ψ}^{eq} depends linearly on $N_{c\bar{c}}$), the present uncertainties in the open-charm cross sections are such that the (semi-) central NA50 data can be accounted for by statistical production alone, see Ref. [121]. It furthermore matters over what range in rapidity the statistical model is applied: in the canonical limit, it follows from eqs. (52) and (53) that $N_{\Psi} \propto 1/V_{FB}(N_{part})$. On the one hand, this roughly gives rise to the observed centrality dependence, but, on the other hand, it also affects the total yield significantly depending on the width of the rapidity window considered. Finally, recalling Fig. 31, even for fixed $N_{c\bar{c}}$, the charm-quark fugacity, and thus the equilibrium charmonium numbers, are sensitive to the underlying open-charm spectrum (medium effects in charmed hadrons and/or quarks, recall Fig. 31).

3.3.2 Transverse-Momentum Spectra and Elliptic Flow

As indicated above, charmonium p_t spectra are hoped to shed more light on the underlying suppression mechanism (in particular, its momentum dependence, recall Fig. 18), as well as to disentangle direct and regenerated production components. Since latter are expected to follow an exponential shape (plus effects from collective flow), vs. the power-law spectra of direct production, regeneration is expected to primarily show up at low momentum (where the open-charm phase space density is the largest). The p -dependence of suppression may thus be more directly studied toward higher momenta, unless regeneration is absent (or small) altogether, as is expected at lower collision energies. In fact, at high momenta, additional effects may lead to a reduction in charmonium suppression, e.g., escape from the fireball (“leakage effect”) [135, 134, 66, 178], delayed formation time due to Lorentz time dilation [134, 179, 156] (leading to, e.g., smaller dissociation cross sections during the build-up of the charmonium wave package [180]), or the well-known Cronin effect [181, 182, 183].

In lower panels of Fig. 36 the centrality dependence of the J/ψ ’s average p_t^2 in the hydro+gluo-dissociation (left) and fireball+quasifree dissociation (right) calculations is compared to NA50 data. Most of the observed increase with centrality is accounted for by the Cronin effect which in both calculations is implemented using the average initial gluon path length, $\langle l \rangle(b)$, prior to charmonium production, $\langle p_t^2 \rangle_{ini}(b) = \langle p_t^2 \rangle_{pp} + a_{gN} \cdot \langle l \rangle(b)$ with $a_{gN} = 0.76 \text{ GeV}^2/\text{fm}$ as extracted from p -A data [184]. The reduction of $\langle p_t^2 \rangle$ toward central collisions in the lower right panel of Fig. 36 [70] is mostly caused by the 3-momentum dependence of the quasifree dissociation rate (cf. right panels in Fig. 18), leading to larger suppression for higher momentum charmonia (the smallness of the regeneration yield, evaluated in blast wave approximation at T_c , renders its impact on $\langle p_t^2 \rangle$ practically negligible). A similar effect is observed in the lower left panel of Fig. 36 [168], despite the decrease of the underlying dissociation rate with 3-momentum. In Ref. [185], the J/ψ and ψ' spectra in central Pb(158 AGeV)–Pb collisions have been analyzed using a blast wave description; the extracted temperature ($T \simeq 170 \text{ MeV}$) and collective expansion velocity ($\bar{v} \simeq 0.2c$) are consistent with the charmonia forming at the hadronization transition (quite similar to the regeneration component in the lower left panel of Fig. 36). However, at high $p_t > 3 \text{ GeV}$ and toward more peripheral collisions, this description most likely needs to be supplemented by non-thermal (primordial) contributions.

At RHIC energies, the regeneration component in both the hydro+gluo-dissociation and the fireball+quasifree dissociation calculations predicts a significant softening of $\langle p_t^2 \rangle$ with centrality, relative to the Cronin enhanced initial production, see the lower panels of Fig. 38. Current PHENIX data support this scenario, but one should note that the Cronin effect is not yet well constrained from available d -A data. The analysis of J/ψ p_t -spectra in terms of a blast wave description does not yet allow for a quantitative identification of the temperature and transverse flow associated with the kinetic decoupling of charmonia. However, the current PHENIX data suggest that a decoupling at the phase boundary results in spectra which are too soft [121], especially for noncentral collisions. This is illustrated more explicitly in Fig. 39, where the J/ψ $R_{AA}(p_t)$ is displayed in 4 centrality bins and compared to the fireball+quasifree dissociation approach [70]. The rather soft regeneration spectra (corresponding to decoupling at T_c with a flow velocity increasing for more central collisions), together with the much harder primordial spectra (including suppression), result in a rather flat $R_{AA}(p_t)$, suggesting that a proper decomposition of the inclusive yields is essential to understand the underlying p_t dependence. Note the significance of the leakage effect at momenta $p_t > 3 \text{ GeV}$. Very recent measurements of high-momentum J/ψ ’s in Cu-Cu($\sqrt{s_{NN}} = 200 \text{ GeV}$) have found that $R_{AA}(p_t > 5 \text{ GeV})$ is compatible with one [187]. At first sight, and in view of the strong suppression of other measured hadrons thus far ($R_{AA}^{\pi, \eta} \simeq 0.25$), this appears as somewhat of a surprise. However, estimates of bottom feeddown ($B \rightarrow J/\psi + X$) and formation time effects (e.g., via a reduced absorption cross section at early times), indicate that this observation may be understood in the framework of the rate-equation approach [188]. Formation time effects coupled with threshold suppression scenarios [134, 135] have indeed predicted an $R_{AA}^{\Psi} \rightarrow 1$ at

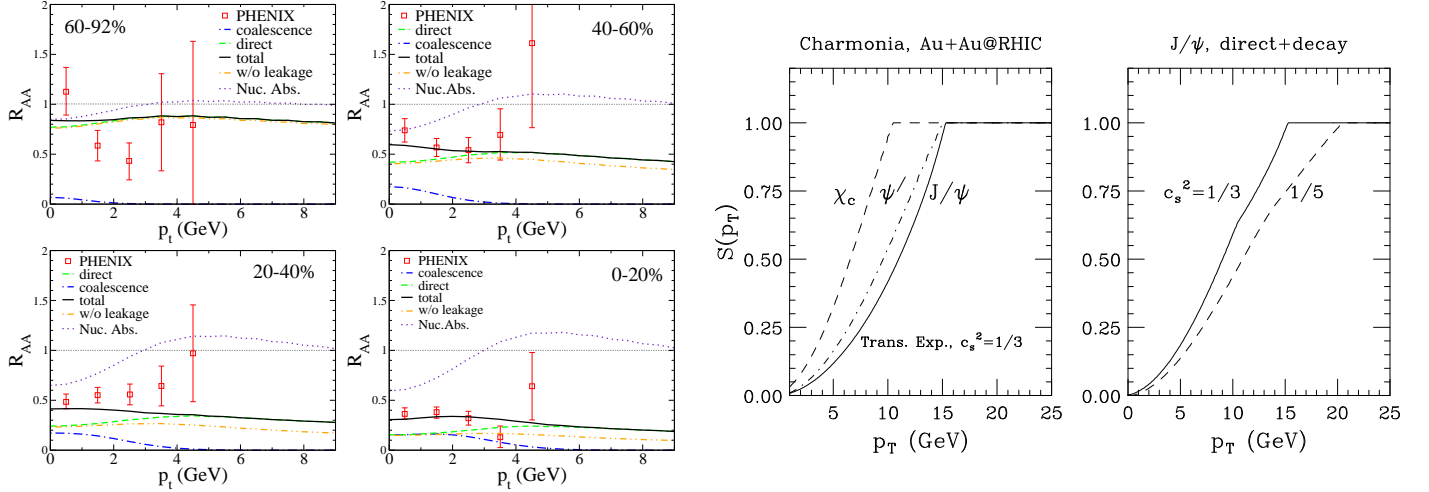


Figure 39: J/ψ nuclear modification factor as a function of transverse momentum in Au–Au($\sqrt{s_{NN}}=200$ GeV) collisions. Left panels: PHENIX data [20] compared to calculations in a fireball+quasifree dissociation model (including regeneration) [70] in various centrality classes (dotted lines: primordial production including Cronin effect and nuclear suppression, dashed line: primordial production after QGP and hadronic suppression, dash-double-dotted line: primordial suppressed production without leakage effect, dash-dotted line: regeneration yield in blast-wave approximation, full line: total). Right panels: suppression of direct charmonium states (second from right) and inclusive J/ψ (far right; including feeddown as well as the sensitivity to the speed of sound employed in the hydrodynamical expansion) within a hydrodynamic model employing the QGP threshold-melting scenario supplemented by formation time effects [186];

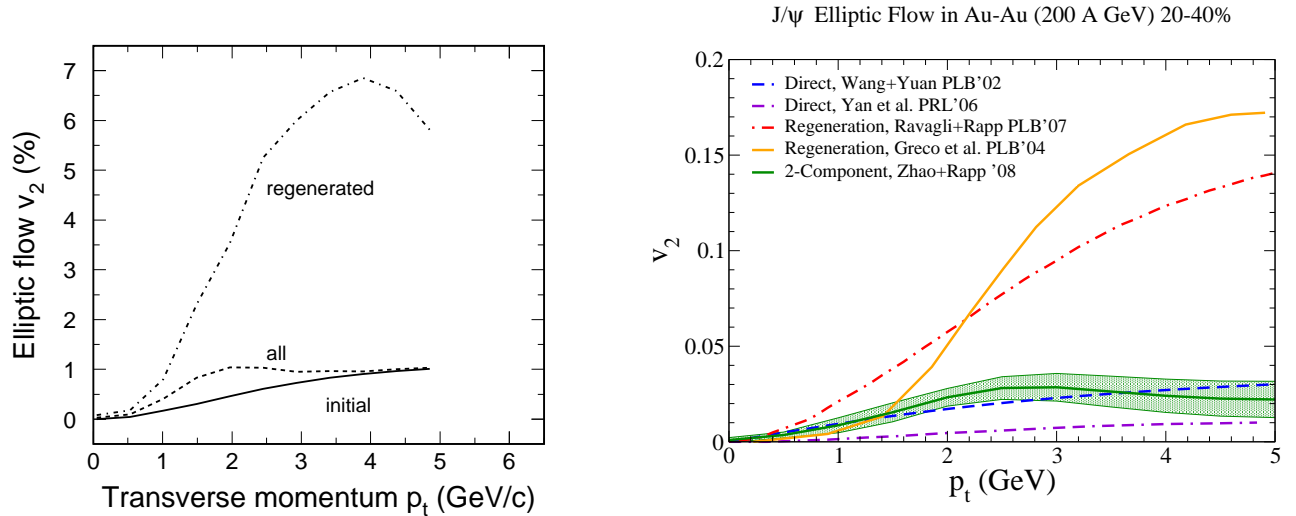


Figure 40: Theoretical predictions for elliptic flow of J/ψ mesons in 20-40% central Au–Au($\sqrt{s_{NN}}=200$ GeV) collisions (corresponding to an average impact parameter of $b \approx 7.8$ fm). Left panel: transport calculations in the hydro+gluo-dissociation approach [124]; right panel: weighted average of coalescence model and suppression calculations using the p_t -dependent weights computed in the fireball+quasifree dissociation approach [70, 188].

high p_t , cf. right panel of Fig. 39 [186]. A rather unique signature of this effect is a stronger suppression of J/ψ relative to χ_c , which is opposite to both conventional suppression and statistical hadronization scenarios.

A particularly promising observable to discriminate suppressed primordial production from regeneration is believed to be the azimuthal asymmetry of the J/ψ 's in the transverse plane, quantified by the second Fourier coefficient, $v_2(p_t)$, in the azimuthal angle, ϕ , relative to the direction of the impact parameter vector (commonly identified with the positive x -axis),

$$\frac{dN_\Psi}{d^2p_t} = \frac{dN_\Psi}{p_t dp_t} (1 + 2v_2(p_t) \cos(2\phi) + \dots) . \quad (61)$$

This hope is based on a large difference between the v_2 associated with direct and regenerated charmonia. For the former, the azimuthal asymmetry is solely due to the different path lengths of the J/ψ traversing the almond-shaped overlap zone in a noncentral nuclear collision: a shorter path length along the “short” (x -) axis of the almond implies less suppression, while there is larger suppression along the “long” (y -) axis. Calculations typically predict a corresponding v_2 of up to 1-3 % [189, 124], see Fig. 40. On the contrary, if charmonia are regenerated from $c\bar{c}$ coalescence, their v_2 is largely determined by the underlying charm-quark elliptic flow, $v_2^{c\bar{c}}$, and expected to approximately “scale” as $v_2^\Psi(p_t) \simeq 2v_2^c(p_t/2)$ (assuming $v_2^c = v_2^{\bar{c}}$)⁵. Such an approximate scaling has been observed at RHIC for light and strange mesons and baryons, with the inferred light-quark v_2 reaching up to ~ 7 -8%. If the charm-quark v_2 reaches similar values (as indeed suggested by theoretical predictions [190] for semileptonic electron-decay spectra [191]), the elliptic flow of regenerated J/ψ 's may reach up to $\sim 15\%$ [123, 192] (see right panel of Fig. 40), about an order of magnitude larger than in suppressed primordial production. In a two-component picture, the combined (total) is then simply given by the weighted sum, $v_2^{\text{tot}}(p_t) = f^{\text{dir}}(p_t) v_2^{\text{dir}}(p_t) + f^{\text{reg}}(p_t) v_2^{\text{reg}}(p_t)$, with $f^{\text{dir}}(p_t) + f^{\text{reg}}(p_t) = 1$ at each value of p_t . The left panel of Fig. 40 displays the results of the hydro+gluo-dissociation transport model (employing thermal c -quark distributions) [124]. While the v_2 of the regenerated component is large, it carries a small weight (decreasing toward higher p_t), leading to a total v_2 of around 1%. This will be very difficult to detect experimentally. In the right panel of Fig. 40, the total J/ψ v_2 (represented by the band) has been estimated by combining blast-wave results for the regenerated component [123, 192] with the suppression calculations of Refs. [189, 124], using the weighting following from the fireball+quasifree dissociation model [70]. The maximum value for the total v_2 of $\sim 3 \pm 1\%$ is somewhat larger than in Ref. [124], mostly due to the larger v_2 in the coalescence component. Most of the difference in the v_2 of the regenerated component in Refs. [124] and [188] is presumably due to the fact that the former accounts for continuous regeneration throughout the QGP while the latter approximates the production at T_c . Another difference could be due to the underlying formation reaction, which is $c + \bar{c} \rightarrow J/\psi + g$ in Ref. [124] compared to $c + \bar{c} + p \rightarrow J/\psi + p$ ($p = q, \bar{q}$ or g) in Ref. [70]. The main point, however, is the overall smallness of the J/ψ elliptic flow in both approaches; note that for semicentral collisions ($N_{\text{part}} \simeq 150$), for which the v_2 is evaluated, both calculations underestimate the inclusive yield (cf. upper panels of Fig. 38), leaving room for extra regeneration and thus somewhat larger elliptic flow.

3.3.3 Rapidity Distributions

The large mass of charm and bottom quarks implies their rapidity distributions in hadronic (and nuclear) collisions to be significantly narrower than those of light and strange quarks (hadrons). Since the latter essentially determine the volume of the fireball at a given temperature (e.g., T_c), the charm-quark fugacity and thus the equilibrium number of charmonia will be narrower than that from primordial production (in the grand-canonical limit, $N_\Psi = N_{c\bar{c}}^2/V_{FB}$). This is to be contrasted with the suppression of direct production, which is expected to become weaker with decreasing light-particle production (matter density), entailing a broader rapidity distribution than the primordial one. The rapidity dis-

⁵More precisely, the Q -value of the reaction should be small, i.e., the meson mass should be close to the quark-antiquark threshold; this may be a good approximation for loosely bound J/ψ 's.

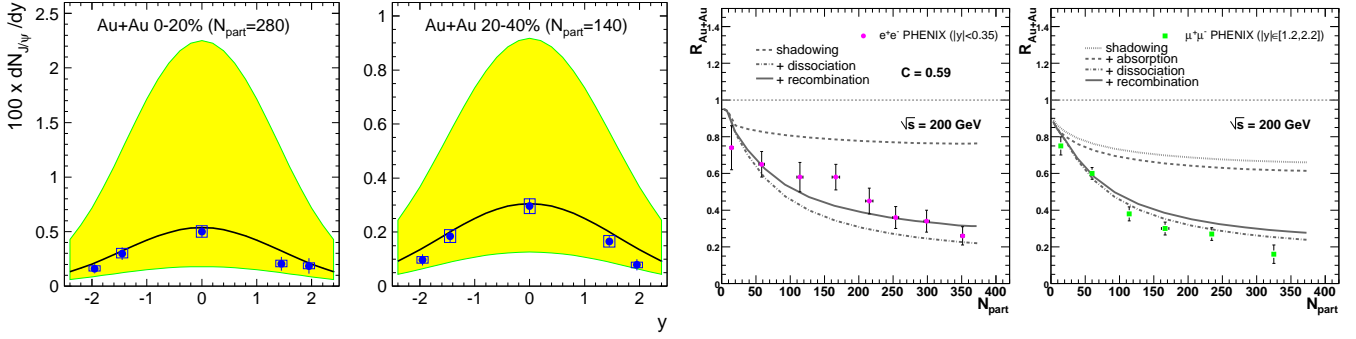


Figure 41: Rapidity dependence of J/ψ production in Au–Au($\sqrt{s_{NN}}=200$ GeV) collisions at RHIC. Left panels: calculations for the rapidity density in central (first left) and semicentral (second left) Au–Au within the statistical hadronization model [121], compared to PHENIX data [20]. The central lines (and shaded error bands) correspond to (the uncertainty in) pQCD charm cross sections, $\sigma_{pp}^{c\bar{c}}=256^{+400}_{-146}$ μb [193]. Right panels: calculations for $R_{AA}(N_{part})$ within the comover-interaction model (including regeneration) at mid- (second from right) and forward (far right) rapidity [144], compared to PHENIX di-electron and di-muon data [20].

tributions of the PHENIX J/ψ data in Au–Au exhibit a narrowing relative to pp collisions which is quite consistent with regeneration only, as demonstrated by calculations in the statistical hadronization model [121], cf. the two left panels in Fig. 41. Alternatively, the rapidity dependence has been evaluated in the comover-interaction model in Ref. [144] (two right panels in Fig. 41). Including shadowing and comover dissociation on the direct component, the total suppression of the latter is about equal at mid and forward rapidity (larger comover density around $y=0$ is essentially compensated by larger shadowing at $y=1.2-2.2$). Only upon inclusion of a gain term does the J/ψ production at mid-rapidity slightly exceed the one at forward y .

3.3.4 Excitation Function

The possibly most sensitive observable to identify the interplay of direct (suppressed) and secondary charmonium suppression is an excitation function. This is due to the much stronger increase of charm-compared to light-quark production over a large range in energy. Original predictions of a 2-component model [23] for central A - A collisions envisaged a transition from a suppression-dominated regime at SPS to a largely regeneration-dominated one at top RHIC energy, cf. left panel of Fig. 42. While the more recent theoretical analyses (upper panels of Fig. 38) suggest that the current RHIC data contain a smaller fraction of regeneration than originally predicted, it is important to realize the following (experimental) uncertainty pertaining to secondary production in the commonly used nuclear modification factor: For a hadron h , the latter is generically defined as the yield (or spectrum) in A - A normalized to the binary-collision scaled yield in pp , $R_{AA}^h = N_{AA}^h / (N_{coll} N_{pp}^h)$. For (suppressed) primordial J/ψ production, the dependence on the initial production thus drops out (to the extent that primordial production follows binary collision scaling). This is, however, *not* the case for the (absolutely normalized) regeneration component, which in R_{AA} plots is therefore beset with additional uncertainty due to the input cross section from pp collisions (at RHIC the pertinent experimental uncertainty currently amounts to $\sim 20\text{-}25\%$ [194]). The right panel of Fig. 42 shows calculations of the statistical hadronization model (augmented by direct production from a corona region) for the centrality dependence of J/ψ over open-charm numbers at midrapidity for top SPS, RHIC and LHC energies (using pQCD values for the open-charm production cross section and assuming a fixed value of $N_{J/\psi}/N_{c\bar{c}}=1\%$ in pp). The

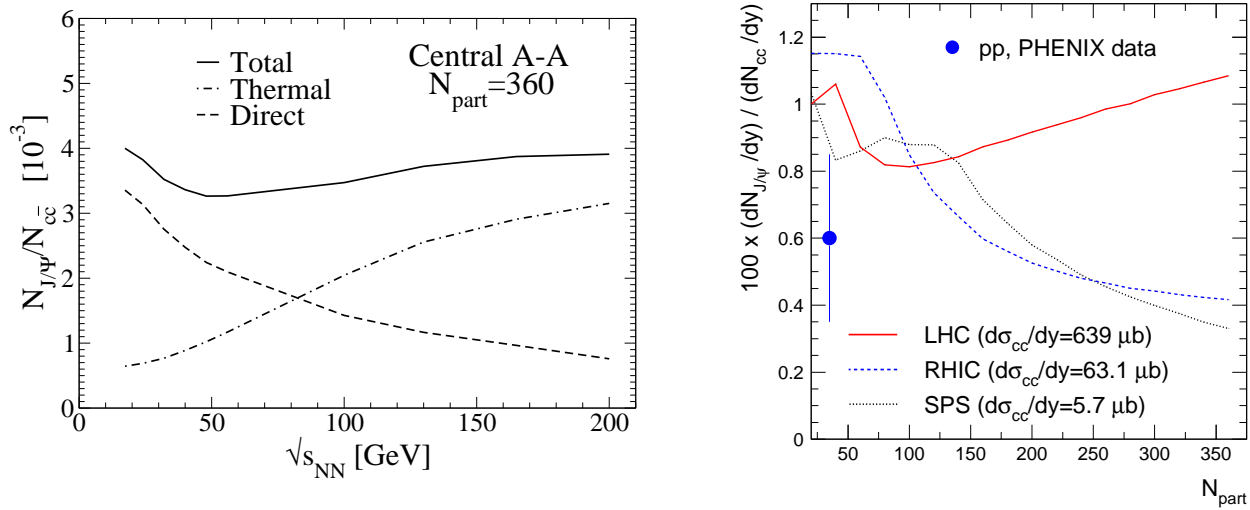


Figure 42: Collision-energy dependence of J/ψ production, normalized to the number of $c\bar{c}$ pairs, in ultrarelativistic heavy-ion collisions. Left panel: original predictions of the 2-component model [23, 65] for central A - A collisions from SPS to RHIC energies. Right panel: predictions within the statistical hadronization model for the centrality dependence at SPS, RHIC and LHC including corona effects for direct production [121]; the data point is obtained from PHENIX pp measurements [194, 195].

increasing trend toward more peripheral collisions at SPS and RHIC is largely induced by the canonical suppression factor (note that for central collisions, the results are in good agreement with the excitation function in the left panel of Fig. 42). At LHC, however, the transition to the grand-canonical ensemble is essentially completed at $N_{part} \simeq 100$, so that for larger centralities a distinct increase of $N_{J/\psi}/N_{c\bar{c}}$ occurs, signalling the dominance of the recombination of uncorrelated c and \bar{c} quarks into J/ψ 's.

3.3.5 Excited Charmonia

In all phenomenological applications discussed in this section thus far the number of J/ψ 's refers to inclusive production, i.e., contains the feeddown contributions of excited charmonia ($\sim 32(8)\%$ from $\chi_c(\psi')$ in pp reactions). E.g., a comprehensive interpretation of SPS and RHIC data in terms of a schematic “sequential melting” scenario has recently been presented in Ref. [196]. In addition to their role in J/ψ production, excited charmonia provide valuable complementary information on the produced medium as their (in-medium) binding energies, dissociation widths and dissolution temperatures (are expected to) differ significantly from the J/ψ . Consequently, future experimental programs put a large emphasis on direct measurements of χ_c and ψ' , as elaborated in Sec. 4. E.g., ratios of different charmonia can be used to test (the approach to) relative chemical equilibrium; in Ref. [197] it has been suggested that a dropping σ -meson mass (as a consequence of (partial) chiral symmetry restoration) leads to a substantial acceleration of the transition rate for $\psi' \leftrightarrow J/\psi + \sigma$ close to T_c , which provides an explanation for the observed ψ'/ψ ratio in central Pb–Pb. The same result is obtained in the statistical hadronization model [21], although here the underlying mechanism is different, i.e., a QGP hadronizing into thermal and (relative) chemical equilibrium (with explicit conservation of the number of charm and anticharm quarks). In the thermal rate-equation approach of Ref. [17], regeneration at SPS energies is a small effect, and the QGP phase is too short to provide sufficient ψ' suppression to describe the NA50 data for the ψ'/ψ ratio (dashed line in the left panel of Fig. 43). However, if effects of (partial) chiral restoration are implemented via a reduction of the in-medium D -mesons masses (associated with their light-quark content), the direct $\psi' \rightarrow D\bar{D}$ channel opens and leads to a large increase of the ψ' dissociation rate in the hadronic phase close to T_c (in the vacuum, the ψ' mass

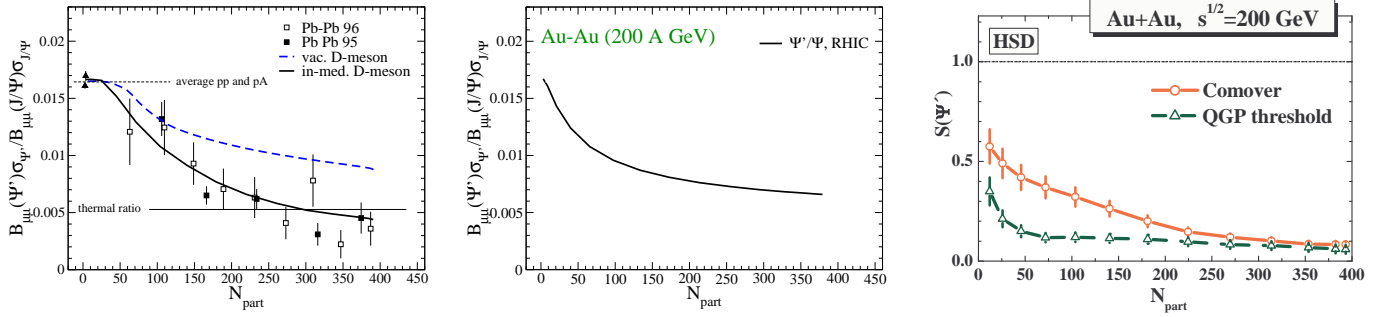


Figure 43: ψ' production in ultrarelativistic heavy-ion collisions. Left and middle panel: ψ'/ψ ratio as computed in the thermal rate-equation approach with quasifree dissociation in the QGP and hadronic dissociation with (solid lines) and without (dashed lines) in-medium D -meson masses at SPS (left) [17] and RHIC (middle). Right panel: suppression (nuclear modification) factor for the ψ' in the HSD transport approach in the comover-interaction (circles) and QGP threshold-suppression (triangles) scenarios [198]. Note that upon dividing the ψ' suppression factor by the one for the J/ψ , the comover results are quite compatible with the thermal rate equation in the middle panel.

is only ~ 50 MeV below the $D\bar{D}$ threshold). This allows for a good description of the NA50 ψ' data. We note that reduced in-medium D -meson masses (or a broadening of their spectral function which also opens phase space for direct $\psi' \rightarrow D\bar{D}$ decays) and relative equilibration via $J/\psi + \sigma \leftrightarrow \psi'$ are not mutually exclusive mechanisms (neither is statistical hadronization, which, however, requires the prevalence of regeneration). At full RHIC energy, both the thermal rate-equation approach (middle panel in Fig. 43) and HSD transport calculations using pre-hadronic and comover interactions with regeneration (right panel in Fig. 43) predict a ψ'/ψ ratio which is very similar to SPS energies. On the other hand, threshold-melting scenarios predict significantly sharper suppression patterns in the centrality dependence. Similar features are expected for χ_c production.

3.3.6 Bottomonia

Bottomonium observables are expected to add at least two valuable aspects, relative to charmonia, for the study of the medium in heavy-ion collisions at RHIC and LHC: (i) larger binding energies (parametrically, for Coulombic wave functions, $\varepsilon_B^{Q\bar{Q}} \propto \alpha_s^2 m_Q$), implying larger dissociation temperatures and thus different dissociation patterns. (ii) a larger mass of the bottom quark, reducing its primordial production (e.g., $N_{b\bar{b}} \approx 0.1$ per central Au–Au at RHIC), which suggests that recombination effects are suppressed. The latter assertion, however, has to be taken with care since primordial Υ production is also relatively small (typically $N_\Upsilon/N_{b\bar{b}} \simeq 0.1\%$ compared to 1% for charm), and bottom-quark fugacities can be rather large.

Early studies of bottomonium production in heavy-ion collisions have focused on suppression effects [137, 138]. Similarly, in Ref. [199], the threshold-melting scenario, combined with formation effects, has been utilized to compute the p_t dependence of suppression factors, $S(p_t) \equiv R_{AA}(p_t)$, at the LHC. Assuming initial temperatures of $T_0 \simeq 0.8 - 1.2$ GeV, a large suppression for all states has been predicted at low p_t , which, however, gradually disappears in the range of $p_t \simeq 5 - 30$ GeV (qualitatively similar to the right panel in Fig. 39), depending on the Debye mass and surface effects in the fireball. An extension of the threshold-melting scenario to RHIC [186] suggests that directly produced Υ 's do not undergo any suppression, while inclusive Υ 's (which receive about 40-50% feeddown from χ_b and Υ') are suppressed by up to 45% at low p_t due to an almost complete melting of the excited states. As mentioned above, the threshold-melting picture represents a sharp transition between stable and dissolved quarkonia, i.e., a sudden “jump” of the inelastic width from zero to infinity. This is obviously an oversimplification of a more realistic situation where the width gradually increases with temperature,

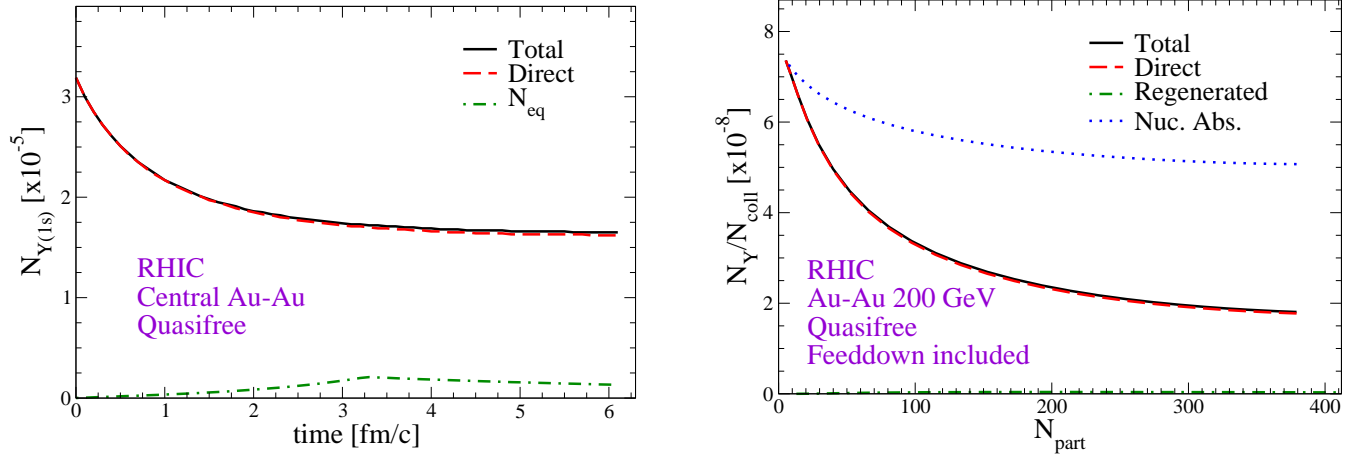


Figure 44: Predictions for Υ production at RHIC within the thermal rate-equation approach using quasifree dissociation with in-medium binding [72] in an expanding fireball. Left panel: time evolution of Υ abundance in central Au–Au; right panel: centrality dependence of inclusive Υ yield.

as found in more microscopic calculations discussed in Sec. 2.3 (in the context of Fig. 19).

Quantitative studies of bottomonium suppression and regeneration have been performed in Ref. [72] within the thermal rate equation (21), solved in an expanding fireball background. When assuming vacuum binding energies for the Υ throughout the QGP evolution at RHIC (with an initial temperature of $T_0=370$ MeV, dropping to 300 MeV within the first 0.5 fm/c), the results of Ref. [186] have been confirmed in that no significant (direct) Υ suppression (nor regeneration) occurs; this is understandable due to the large lifetime of several tens of fm/c for temperatures below 300 MeV (recall left panel in Fig. 19). The situation changes appreciably when in-medium reductions of the bottomonium binding energies are included (based on the in-medium rates displayed in the left panel of Fig. 19). In central Au–Au at RHIC, direct Υ 's are suppressed by $\sim 40\%$, with most of the suppression occurring in the first 1 fm/c, i.e., for temperatures above 250 MeV (cf. left panel of Fig. 44). In the centrality dependence of inclusive Υ production (right panel in Fig. 44) the suppression is further amplified, due to $\sim 50\%$ feeddown contributions from excited χ_b ($\sim 40\%$) and Υ' ($\sim 10\%$) states; regeneration contributions are (very) small. An important point here is that direct Υ suppression at RHIC appears to be a rather direct measure of the Debye screening in the heavy-quark potential, especially since regeneration is absent. The binding energies figuring into the calculations of Ref. [72] are, in fact, somewhat smaller than potential models based on the internal energy (but significantly larger than based on the free energy), as discussed in Sec. 2.2. In either case, one could envisage a situation where the production of Υ is as (or even more) suppressed as for J/ψ . This would be a rather unique QGP signature [72], and provide undisputable evidence of charmonium regeneration.

At the LHC, the situation becomes more involved. The rate-equation approach (left panel in Fig. 45) [72] predicts a suppression of up to a factor of ~ 10 stronger than the statistical hadronization model [121]. Besides moderate differences in input cross sections (e.g., a factor of 0.8 shadowing correction in Ref. [72]), there are several sources of this uncertainty: (i) the equilibrium limit in the rate equation is computed in the QGP with (in-medium) bottom-quark masses (rather than bottom hadrons), leading to smaller bottom-quark fugacities; the resulting equilibrium number is up to a factor of 3-6 smaller, depending on the (not very well known) spectrum of bottom hadrons. (ii) the equilibrium limit in the rate equation is reduced by a schematic thermal relaxation-time factor, $\mathcal{R}(\tau) < 1$, to mimic incomplete b -quark thermalization; at the end of the QGP phase this factor has reached to about 0.3-0.5 (smaller before). However, close to T_c , the inelastic reaction rates for the bottomia are already rather small; (iii) as mentioned for charmonia at SPS, there is a question over which range in rapidity the thermal ensemble of bottom quarks should be defined (e.g., $\Delta=3.6$ and 1 in Refs. [72] and [121], respectively). More work is needed to clarify these questions.

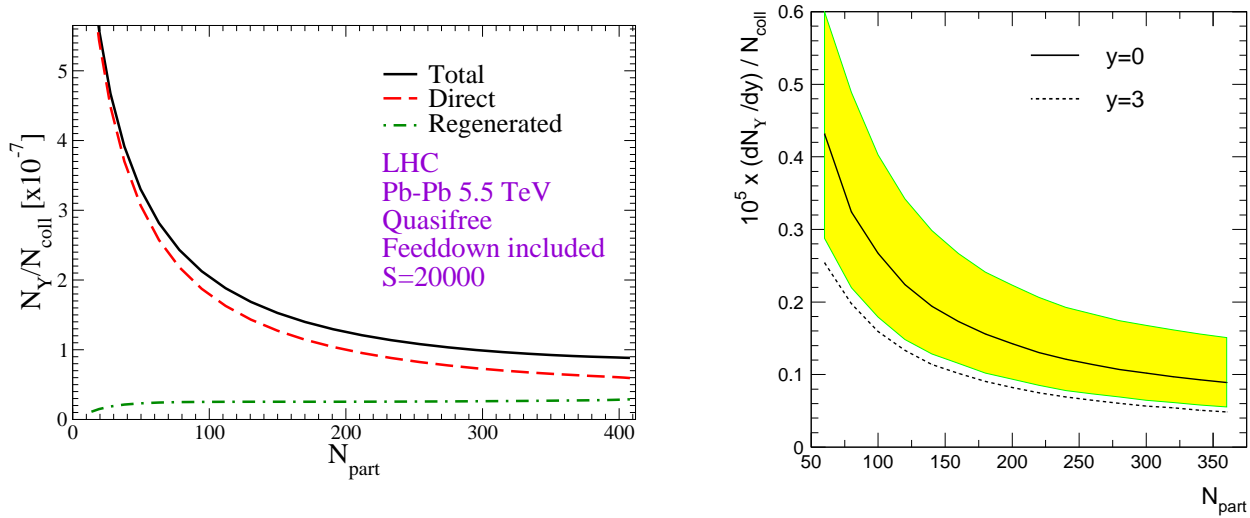


Figure 45: Predictions for the centrality dependence of inclusive Υ production at LHC. Left panel: thermal rate-equation approach [72]. Right panel: statistical hadronization model [121].

4 Future experiments

This chapter is devoted to the presentation of future opportunities of quarkonia measurements in heavy ion collisions. Detectors are currently being designed, built, installed, commissioned or upgraded around three accelerators which will deliver heavy ion beams in three different energy domains:

- RHIC-II (starting time scheduled for 2013) is an upgrade program of the existing RHIC (Relativistic Heavy Ion Collider) at Brookhaven National Laboratory, USA, which delivers beams up to $\sqrt{s_{NN}} = 200$ GeV for Au. The upgrade of the machine consists of an increase of the present luminosity by an order of magnitude as well as a low energy program ($\sqrt{s_{NN}} = 5 - 15$ GeV). Whereas the low energy physics program will mainly focus on the discovery of the critical point, the high-luminosity high-energy physics program aims at completing existing measurements with a strong emphasis in the heavy flavor sector. To achieve this goal, an upgrade program of two detectors (PHENIX and STAR) is underway;
- The LHC (Large Hadron Collider) at CERN will provide, from 2008 on, the largest energy ever delivered by an accelerator with proton beams up to $\sqrt{s} = 14$ TeV and Pb beams up to $\sqrt{s_{NN}} = 5.5$ TeV. Three of the four LHC experiments (ALICE, ATLAS and CMS) will take heavy-ion data with an important part of their physics program devoted to quarkonia measurements. Whereas ATLAS and CMS are designed for proton-proton physics, ALICE is dedicated to the study of heavy-ion collisions;
- The SIS-300, located at the FAIR (Facility for Antiproton and Ion Research) at GSI, Darmstadt, will deliver, from 2015 on, heavy ion beams in fixed target mode with beam energy from 10 AGeV to 45 AGeV ($\sqrt{s_{NN}} = 4.5 - 9.3$ GeV). The CBM detector will allow to explore, with high statistics measurements of rare signals like quarkonia, the moderate temperature and large baryon chemical potential region of the QCD phase diagram.

It is worth noticing that in two of these energy ranges (LHC and SIS-300) heavy quark resonances will be measured for the first time. This certainly ensures a rich and exciting future physics program. In the following, we present the motivations for studying quarkonium production in these three energy ranges as well as a short overview of the detector capabilities needed to achieve this goal. All detectors have

in common the goal of performing quarkonium measurements as a function of centrality and reaction plane, in a broad acceptance, with large statistics and low background, to ensure a mass resolution good enough to separate all vector resonances and to identify feed-down from excited states. For more details about these experimental programs we refer to [200] (RHIC-II), [201, 202, 203, 204] (LHC) and [205] (SIS-300).

4.1 Quarkonia in heavy ion collisions at the RHIC-II

The RHIC has started delivering heavy-ion beams in 2000. Since then, the four heavy-ion experiments (BRAHMS, PHENIX, PHOBOS and STAR) have collected a large set of data for various systems at energies $\sqrt{s_{NN}} = 20 - 200$ GeV. The status of information gathered up to 2004 has been summarized both from the theoretical side [206] and from the experimental side [207]. Hard probe precision measurements have become accessible at RHIC with the high statistics runs performed since 2004. The measurements, done by the PHENIX and STAR collaborations, have revealed some of the most exciting aspects of the hot and dense matter produced at RHIC. A particularly striking and unexpected observation in the quarkonium sector is the J/ψ suppression whose magnitude in mid-central and central heavy-ion collisions is similar to that measured at SPS energy for the Pb-Pb system (recall Figs. 36 and 38). As a consequence, several models which offer a successful quantitative description of J/ψ suppression at SPS energy (assuming that the suppression is driven by the system temperature or its energy density) strongly over-predict the suppression observed at RHIC. Furthermore, the observed J/ψ suppression is larger in the forward region than in the central region (Fig. 41). This observation is again striking as most of the suppression models predict an opposite effect, i.e., the higher the energy density the larger the suppression. The interpretation of these observations has been discussed in Sec. 3.3.

Further detailed measurements are mandatory in order to disentangle the different theoretical interpretations and to achieve a comprehensive understanding of quarkonia production in heavy-ion collisions at RHIC. Indeed, a direct evidence for resonance dissociation by color screening requires the centrality dependence of J/ψ , χ_c and ψ' to be measured simultaneously. Regeneration models can be constrained from the inspection of J/ψ rapidity distributions which are expected to narrow [129, 121] (recall Fig. 41), as well as from a precise measurement of the (open) charm production cross-section. Trends in the excitation function of J/ψ suppression could also reveal the relative importance of the regeneration process as it should increase with the multiplicity of $c\bar{c}$ pairs [23]. More stringent tests include measurements of J/ψ elliptic flow since, as open charm shows non-zero flow⁶, J/ψ , if produced by regeneration, should inherit this flow (recall Fig. 40). In addition, both J/ψ flow and suppression should exhibit a specific p_t dependence marked by QGP effects at relatively low p_t whereas the high p_t region should be mostly populated by J/ψ which could escape the medium unaffected. In this respect it is also important to be able to identify secondary J/ψ from bottom decay whose yield might be sizable at high p_t . Furthermore, detailed measurements in p -A collisions are mandatory in order to unravel cold and hot nuclear effects. We finally note the possibility to identify the presence of the deconfined medium from the measurement of J/ψ polarization [208]. In addition to the above observables based on charmonia, the measurement of bottomonium states should provide additional insights. The temperature of the medium at RHIC is expected to be large enough to induce the break-up of $\Upsilon(2S)$ and $\Upsilon(3S)$ whereas the $\Upsilon(1S)$ is supposed to melt at higher temperatures (of course, it might still be affected by inelastic reactions with partons in the QGP, as discussed in Sec 2.3).

The previously exposed physics program can partially be covered in the next years with the existing RHIC machine and detectors. However, it is clear that the full physics program requires high statistics

⁶In contrast to light flavor hadrons, the heavy flavor flow is, so far, not measured experimentally through identified hadrons, but in an inclusive way via the flow of non-photonic electrons. The latter is obtained from full distributions of electrons after subtraction of Dalitz-decay electrons from light hadrons and photon-conversion electrons.

and excellent data quality. This quality will be achieved by means of an upgrade of the machine luminosity and of the detectors.

4.1.1 Experimental conditions

With the luminosity upgrade of the machine, the integrated luminosity per week is expected to be $2500\mu\text{b}^{-1}$ and 33pb^{-1} for Au–Au and pp collisions at $\sqrt{s_{NN}} = 200$ GeV, respectively. A typical run at RHIC consists of 24 weeks of data taking. This is significantly longer than a LHC run in heavy-ion mode (see below). As a consequence, although the heavy flavor production cross-sections are much bigger at the LHC, the lower cross-sections at RHIC-II are compensated by the integrated luminosity and the heavy flavor yields for one year of running are expected to be similar at RHIC-II and at the LHC.

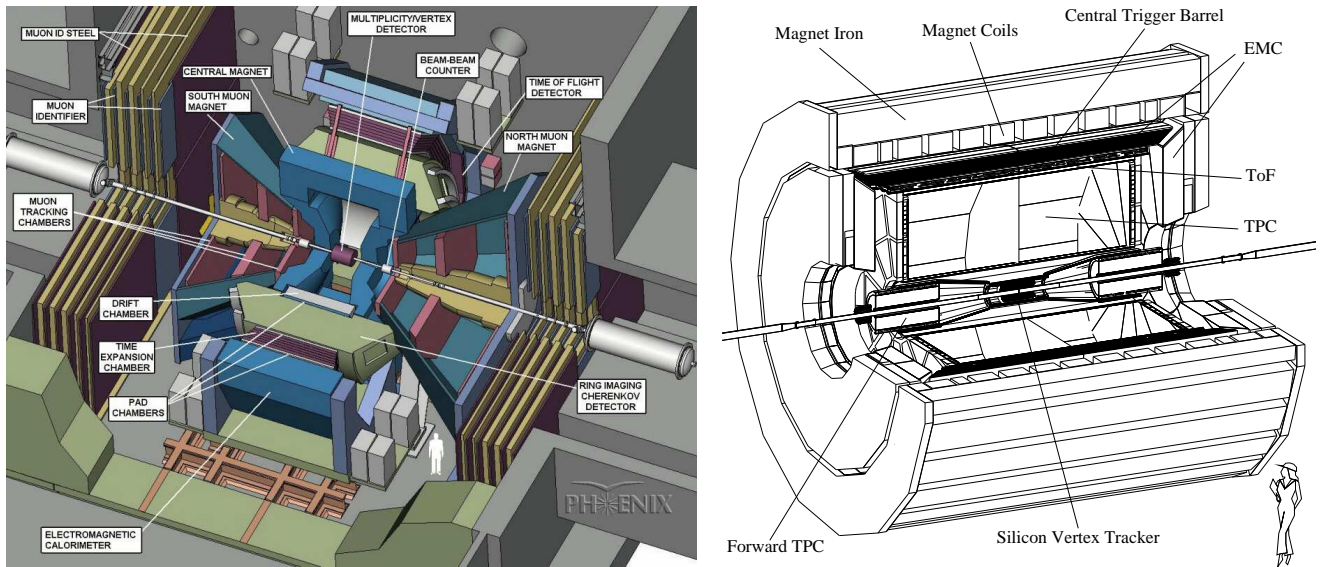


Figure 46: Longitudinal view of the PHENIX (left) and STAR (right) detectors.

4.1.2 The PHENIX experiment

The PHENIX experiment is made of four spectrometers and a set of specialized detectors to determine the collision centrality and to provide triggers (Fig. 46 left). In the central region, two arms allow to detect electrons, photons and charged hadrons. They consist of a complex arrangement of drift chambers, pad chambers, Time Expansion Chambers (TEC) operated as transition detectors, time-of-flight detectors, RICH detectors, aerogel detectors and electromagnetic calorimeters. A magnet supplying a field parallel to the beam is placed around the interacting vertex. In the forward and backward regions, two spectrometers allow muon measurements in the rapidity range $-2.25 < y < -1.15$ and $1.15 < y < 2.44$. They consist of a muon tracker (three stations of multi-plane drift chambers) placed inside a radial magnetic field followed by a muon identifier (alternating layers of steel absorbers and streamer tubes for tracking) both with full azimuthal coverage.

The upgrade program of PHENIX [200] consists of a barrel and two end-caps Silicon Vertex Detectors (SVDs), two Nose Cone Calorimeters (NCCs) and an upgrade of the muon trigger. The SVD will provide inner tracking with full azimuthal coverage for $|\eta| < 2.5$. This will improve the dilepton mass resolution and reduce the background both in the electron and in the muon channels. It will further allow to measure displaced vertices which is mandatory for identification of secondary J/ψ from B hadron decay.

The NCCs contain electromagnetic and hadronic sections covering the acceptance $0.9 < |\eta| < 3.5$. These are key detectors for measuring $\chi_c \rightarrow J/\psi + \gamma$ decay. The muon trigger upgrade consists in adding three layers of RPC detectors in each muon arm together with associated Front-End Electronics and trigger logic. This will improve the level-1 trigger selection for both single and di-muons.

Typical expected yields with the upgraded PHENIX detector for 12 week physics run with Au beams at RHIC-II are 45000 (395000) J/ψ and 400 (1040) Υ in the electron (muon) channel.

4.1.3 The STAR experiment

The different sub-systems of the STAR experiment (Fig. 46 right) are placed in a solenoidal magnet operating at 0.5 T. These main detectors are (i) a large azimuthally symmetric TPC providing charged particle tracking within $|\eta| < 1.8$, (ii) the Silicon Vertex Tracker (SVT) and Silicon Strip Detector (SSD) for charge particle tracking close to the interacting point and vertexing, (iii) the Forward Time Projection Chambers (FTPC) covering $2.8 < |\eta| < 3.8$ to track particles at forward and backward rapidities, (iv) the time-of-flight system providing additional particle identification in the (partial) acceptance of the central detectors and (v) the electromagnetic calorimeter (both in the central region and at forward angles) which ensure neutral particle measurements. Additional specialized detectors complement the setup for centrality measurements and trigger.

The upgrade program of STAR [200] includes a time-of-flight system (TOF) covering the full acceptance of the central barrel, new front end electronics for the existing TPC, an upgrade of the data acquisition system and a new inner tracking system based on two layers of silicon pixel sensors and three layers of silicon strip detectors. The TOF will extend the momentum range for hadron identification and, in conjunction with the electromagnetic calorimeter, will provide a level-2 trigger for $J/\psi \rightarrow e^+e^-$ measurements. The new inner tracking system will make displaced vertex measurements accessible. In PHENIX this will be used to tag J/ψ from B hadron decays, to reconstruct charm hadron in their hadronic decay channel and will allow open heavy flavor measurements from single electrons. Finally, the DAQ upgrade will allow to collect rare signals with large statistics.

Simulations indicate that up to $220 \cdot 10^3$ J/ψ and 11200 Υ could be reconstructed in STAR during a 12 week physics run at RHIC-II in Au–Au collisions.

4.2 Quarkonia in heavy ion collisions at the LHC

With a nucleus-nucleus center-of-mass energy nearly 30 times larger than the one reached at RHIC, the LHC will provide the biggest step in energy in the history of heavy ion collisions and will open a new era for studying the properties of strongly interacting matter under extreme thermodynamical conditions. This new energy regime will lead to a much higher energy density, to a faster equilibration and to a bigger and longer lifetime of the deconfined system resulting in an enhanced role of the QGP over final state hadronic interactions [209]. The higher temperature and close to vanishing baryon chemical potential of the system will render it close to the conditions of the primordial universe. On the other hand, heavy ion collisions at the LHC access unprecedented small Bjorken- x values where low momentum gluons are expected to be close to saturation and lead to a significant shadowing effect. As a consequence (high density) parton distributions are expected to dominate particle production. Another exciting aspect of this new energy regime is the massive production rate of hard processes. They will provide an ideal tool for a detailed characterization of the deconfined medium. Also the heavy flavor sector at LHC energy is subject to significant differences with respect to SPS and RHIC energies. First, the large production rate offers the possibility to use new and large variety of observables⁷. The

⁷From RHIC to LHC, it is expected that the number of $c\bar{c}$ and $b\bar{b}$ pairs produced in central nucleus-nucleus collisions will increase by a factor 10 and 100 respectively [202]: up to 115 $c\bar{c}$ pairs and 5 $b\bar{b}$ pairs are expected to be produced in central (5%) Pb–Pb collisions at 5.5 TeV. This estimate is based on next-to-leading order calculations and includes

magnitude of most of the in-medium effects is therefore anticipated to be dramatically enhanced. Some of these aspects are discussed hereafter.

New observables. The $\Upsilon(1S)$ state is expected to dissolve significantly above the critical temperature, at $\sim 3\text{--}4 T_c$ [42, 50, 57], which presumably comes into reach only with the LHC. The spectroscopy of the Υ family at LHC should then reveal unique characteristics of the QGP. In particular, the p_t dependence of the $\Upsilon(2S)/\Upsilon(1S)$ ratio presents significant sensitivity to the dissociation temperatures [199] (see [72, 210] for updates). Measuring the $\Upsilon(2S)$ is also particularly interesting in order to unravel J/ψ suppression versus regeneration. Indeed, the $\Upsilon(2S)$ and J/ψ dissociation temperatures are predicted to be similar [42] whereas, in contrast to charmonia, bottomonia are expected to be little affected by the regeneration process [72]. On the other hand, electroweak Z^0 and W^\pm bosons will be available with large statistics and can serve as reference processes for quarkonium suppression studies.

Large resonance dissociation rate. In addition to comoving hadrons and color screening, quarkonia can be destroyed by parton ionization [211]. This mechanism, induced by quasi-free partons in the QGP, starts being effective for temperatures above the critical temperature but before the temperature of resonance dissociation by color screening (cf. Sec. 2.3). Recall, however, the interplay between the two mechanisms on the final quarkonium yields: a large dissociation by color screening implies a low binding and which facilitates a large break-up by parton ionization. Recent estimates [212] (see [64] for an update) of the quarkonium dissociation cross-sections show that none of the J/ψ survives the deconfined phase at LHC and that about 20% of the Υ are destroyed, possibly (substantially) more if color-screening is strong, cf. Fig. 45 [72].

Large secondary charmonium production. Secondary charmonia yields can arise due to statistical hadronization [213] and/or kinetic recombination [22]. These processes result in an increase of J/ψ yield with collision centrality roughly proportional to N_{cc}^2 . Here again, this effect is expected to induce dramatic consequences at the LHC. Due to the large number of $c\bar{c}$ pairs produced in heavy ion collisions at LHC, models predict a qualitatively different centrality dependence of the J/ψ yield [212, 214], recall right panel of Fig. 42.

Large charmonium rate from B hadron decay. Another source of non-direct charmonia arises from the decay of B hadrons. The ratio $N(B \rightarrow J/\psi)/N(\text{direct } J/\psi)$ can be determined as follows. The number of directly produced J/ψ in central (5%) Pb–Pb collisions at 5.5 TeV is 0.49 [212]⁸. The corresponding number of $b\bar{b}$ pairs (with shadowing) amounts to 4.56 [212]. The $B \rightarrow J/\psi$ branching ratio is $1.16 \pm 0.10\%$ [215]. Therefore $N(B \rightarrow J/\psi)/N(\text{direct } J/\psi) = 20\%$ in 4π ⁹. These secondary J/ψ from B hadron decay must be subtracted from the primary J/ψ yield prior to J/ψ suppression studies. They can further be used in order to measure the B hadron production cross-section in pp collisions [167], to estimate shadowing in $p\text{--}A$ collisions and to probe the medium induced b quark energy loss in AA collisions. Indeed, it has been shown [216] that the p_t and η distributions of those J/ψ exhibit pronounced sensitivity to b quark energy loss.

shadowing. See [202, 212] for more details.

⁸Including shadowing and feed-down from higher states.

⁹This ratio is subject to large uncertainties since (i) the color-octet model (CEM) used to predict the J/ψ cross-section at LHC under-predicts the CDF data by a factor 2, and (ii) the total $b\bar{b}$ production cross-section in pp collisions at LHC is predicted within a factor 2 to 3 uncertainty resulting from the choice of the quark mass, the renormalization and factorization scales and the parton distribution function. In addition, resonance suppression and/or regeneration, heavy-quark energy loss and other effects not taken into account here could play a significant role.

4.2.1 Experimental conditions

The LHC will be operated seven months per year in pp mode and one month per year in heavy-ion mode. The corresponding estimated effective running time is 10^7 s and 10^6 s for pp collisions and heavy-ion collisions, respectively. The expected luminosity for Pb–Pb collisions is about $5 \cdot 10^{26} \text{ cm}^{-2}\text{s}^{-1}$ which results in a minimum-bias interaction rate of 4 kHz. As described in [201], the heavy- (and light-) ion runs include, over the first five years of operation, one Pb–Pb run at low luminosity, two Pb–Pb runs at high luminosity, one p –A run and one light ion-ion run. In the following years different options are considered depending on the first results.

4.2.2 The ALICE experiment

ALICE (A Large Ion Collider Experiment) is the only LHC experiment dedicated to the study of nucleus-nucleus collisions [201, 202]. The ALICE experiment is designed to ensure high precision measurements of numerous observables based on hadrons, leptons and photons, in a broad acceptance.

The detector (Fig. 47) consists of a central part, a forward muon spectrometer and forward/backward small acceptance detectors. The central part of ALICE consists of four layers of detectors placed in the solenoidal field ($B \leq 0.5$ T) provided by the LEP L3 magnet. From the inner side to the outer side, these detectors are (i) the Inner Tracker System (ITS) consisting of six layers of silicon detectors, (ii) the Time Projection Chamber (TPC), (iii) the Transition Radiation Detector (TRD) and (iv) the Time of Flight system (TOF) based on multi-gap resistive plate chambers. They provide charged particle reconstruction and identification in the pseudo-rapidity range $|\eta| < 0.9$, with full azimuthal coverage and a broad p_t acceptance. The ALICE central barrel will later be equipped with a large acceptance ($|\eta| < 1.4$, $\Delta\Phi = 110^\circ$) Electromagnetic Calorimeter (not shown in Fig. 47). These large area devices are complemented by two smaller acceptance detectors: the High Momentum Particle IDentification (HMPID) and the PHOTon Spectrometer (PHOS). In the forward/backward region, additional detectors (T0, V0 and FMD, not shown in Fig. 47) allow fast characterization and selection of the events as well as charged particle measurement in the pseudo-rapidity range $-3.4 < \eta < 5.1$. At large rapidities, photon multiplicity and spectator nucleons in heavy-ion collisions will be measured by the Photon Multiplicity Detector (PMD) and the Zero-Degree Calorimeters (not shown in Fig. 47), respectively. A forward muon spectrometer covering the pseudo-rapidity range $-4 < \eta < -2.4$ complements the central part. It consists of a front absorber, a dipole magnet, ten high-granularity tracking chambers, a muon filter and four large area trigger chambers.

The performances of the ALICE detector in the quarkonium sector are shown in Fig. 48. Quarkonium states will be measured in both in the electron ($|\eta| < 0.9$) and muon channel ($2.4 < |\eta| < 4.0$). The acceptance will allow reconstruction of differential distributions down to very low transverse momentum in most cases. The resolution of the apparatus, better than $100 \text{ MeV}/c^2$ for invariant masses around $10 \text{ GeV}/c^2$ allows the separation of all resonance states. The expected number of reconstructed J/ψ and Υ during one month of data taking is $677 \cdot 10^3$ and 9600, respectively, in the muon channel for minimum-bias Pb–Pb collisions. The corresponding numbers in the electron channel for central (10%) collisions are $121 \cdot 10^3$ and 1800.

4.2.3 The CMS experiment

CMS (Compact Muon Solenoid) is a general-purpose detector (Fig. 49 right) designed to measure muons, electrons, photons and jets. Although the detector is optimized for pp collisions, a strong heavy ion program has been developed for several years [203]. CMS is composed, from the interaction point to the outer side, of a tracking system, an electromagnetic calorimeter, a hadronic calorimeter and muon chambers arranged in a central barrel and two end-caps. The central element of CMS is a 13 m long, 3 m diameter magnet which delivers a $B = 4$ T solenoidal field surrounding the tracking and

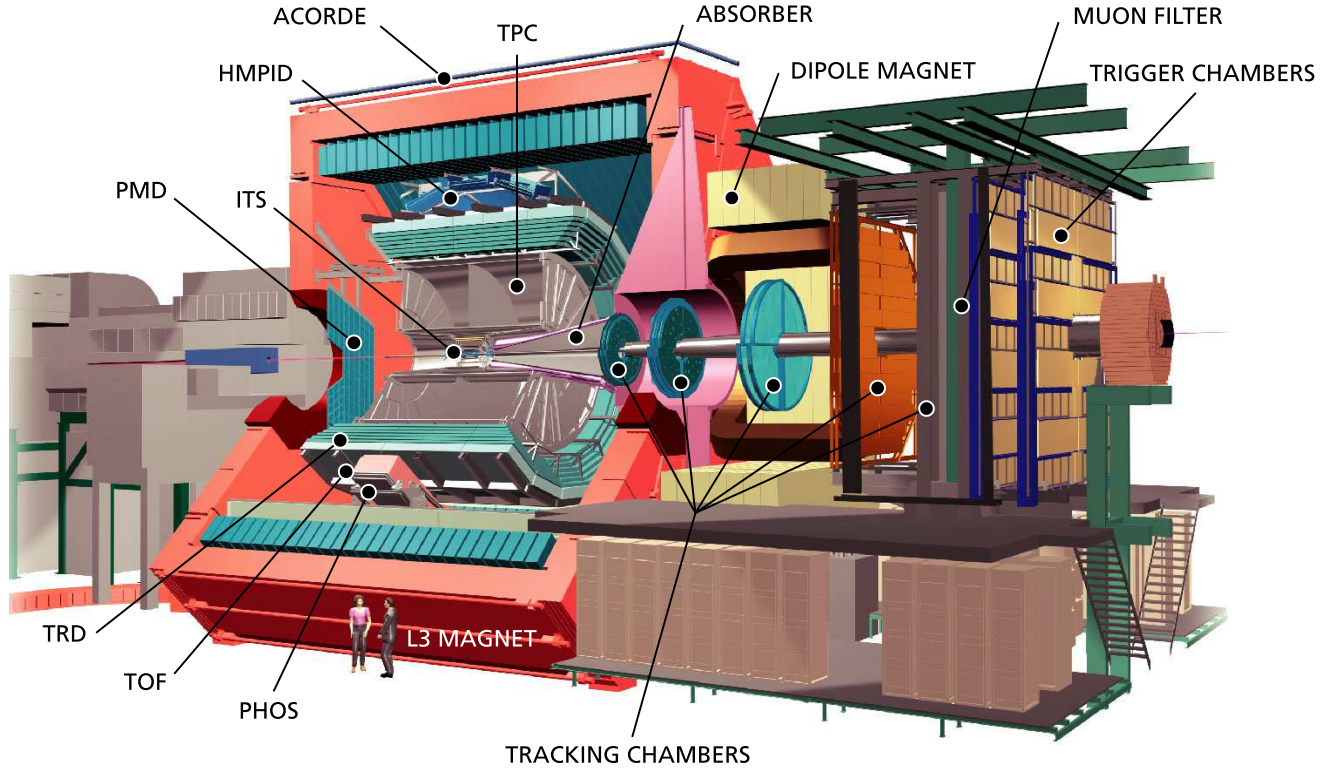


Figure 47: Longitudinal view of the ALICE detector.

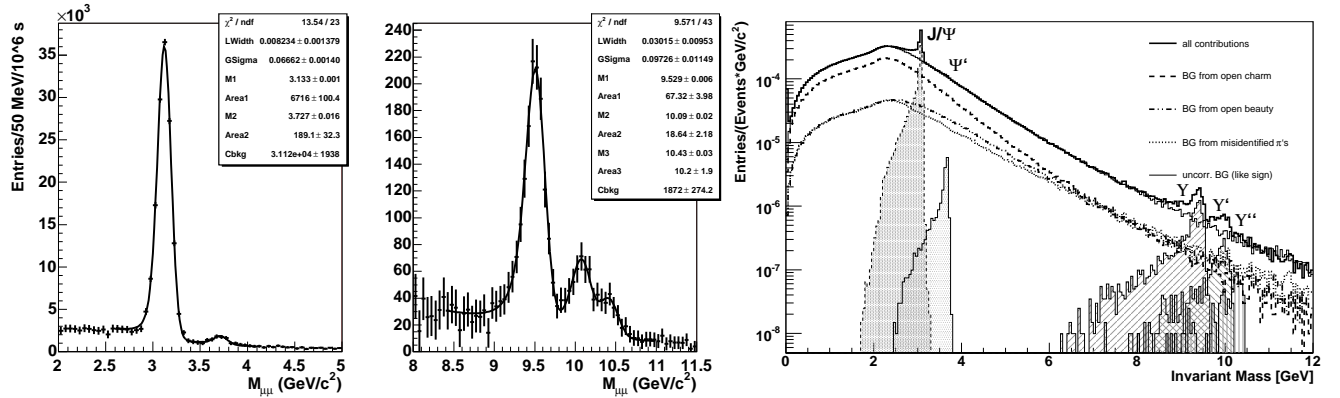


Figure 48: Invariant mass spectra of low mass dimuon (left), high mass dimuon (middle), and dielectron (right), expected to be measured with the ALICE detector within a month of Pb beams (extracted from [202]). In the left and middle plots, the non-correlated background is subtracted from the total spectrum assuming a perfect subtraction i.e. the statistical error of the “full” spectrum is assigned to the remaining spectrum of the sum of the correlated sources.

calorimetric systems. The tracker is based on several layers of silicon pixel and strip counters and covers the pseudo-rapidity region $|\eta| < 2.5$. The electromagnetic calorimeter, made of lead-tungstenate crystals, covers the pseudo-rapidity region $|\eta| < 1.5$ in the central barrel. This coverage is extended to $|\eta| < 3$ with the end-caps. The hadronic calorimeter is made of copper plates and plastic scintillator sandwiches. Its acceptance is $|\eta| < 2$ in the central barrel and reaches $|\eta| < 5.3$ with the end-caps. Two additional very-forward calorimeters ensure coverage in the pseudo-rapidity range $\pm 3 < \eta < \pm 5$. The muon system is located outside the central magnet. It consists of four layers of detectors (three

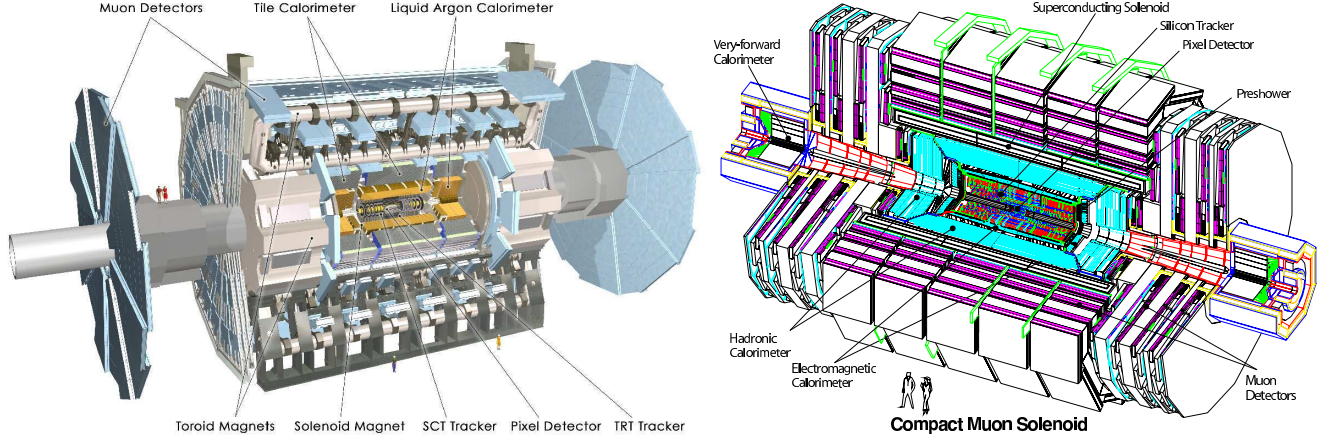


Figure 49: Longitudinal view of the ATLAS (left) and of the CMS (right) detectors.

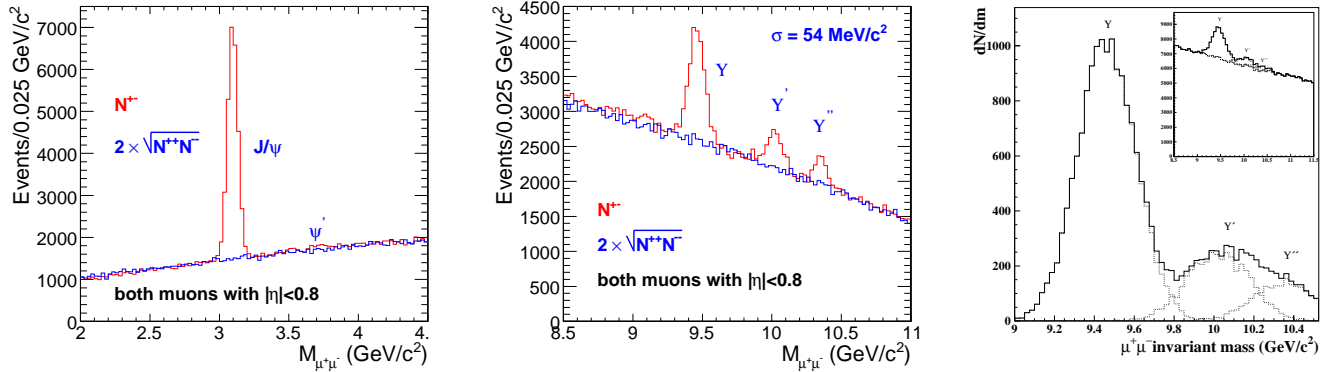


Figure 50: Invariant mass spectra of opposite-sign and like-sign muon pairs in the J/ψ (left) and Υ (middle) mass regions expected to be measured with the central barrel of the CMS detector within one month of Pb–Pb collisions [203]. Right: corresponding invariant mass spectrum of high-mass opposite-sign muon pairs reconstructed with the ATLAS detector [204].

for tracking and one for trigger) covering the pseudo-rapidity range $|\eta| < 2.4$ ($|\eta| < 1.5$ in the barrel). Very forward calorimeters, including two Zero Degree Calorimeters ($\pm 3 < \eta < \pm 5.2$) and a quartz fiber calorimeter ($\pm 5.3 < \eta < \pm 6.7$) allow measurements of the collision centrality and electromagnetic energy (these detectors are not shown in Fig. 49).

Figure 50 shows the dimuon invariant mass spectra expected to be measured for charmonia (left) and bottomonia (middle). The muon acceptance ranges in η from -0.8 to $+0.8$ in the central barrel and from ± 0.8 to ± 2.4 in the end-caps. The excellent mass resolution of the apparatus will allow a very clean separation of quarkonia from the J/ψ to the $\Upsilon(3S)$. In the acceptance of the central barrel, J/ψ measurement will be limited to $p_t > 4$ GeV/c due to the high p_t threshold induced by the calorimeters on single muons. This can be extended to lower p_t when detecting muons in the end-caps thanks to the extra longitudinal Lorentz boost. Due of its higher mass, bottomonium will be measured down to zero p_t in the whole η acceptance. Simulation results indicate that the typical number of reconstructed J/ψ and Υ will be $184 \cdot 10^3$ and $37.7 \cdot 10^3$ in minimum-bias Pb–Pb collisions for one month of data taking.

4.2.4 The ATLAS experiment

Like CMS, ATLAS (A Toroidal LHC ApparatuS) is designed for pp physics. The detector capabilities for heavy ion physics have been recently investigated [204]. The design of the detector (Fig. 49 left) is similar to that of CMS with a tracking system, an electromagnetic calorimeter, a hadronic calorimeter and muon chambers placed in a barrel and two end-caps. The tracking system of ATLAS is composed of silicon pixel detectors, the SemiConductor Tracker (SCT) made of silicon strip detectors, and the Transition Radiation Tracker (TRT). It is placed inside a $B = 2$ T solenoidal magnet and covers the pseudo-rapidity range $|\eta| < 2.5$. The electromagnetic calorimeter is a liquid argon device covering $|\eta| < 4.9$. It is surrounded by the hadronic calorimeter which consists of lead-scintillators in the barrel ($|\eta| < 1.7$) and liquid argon in the end-caps ($\pm 1.5 < \eta < \pm 3.2$). Two additional (electromagnetic and hadronic) calorimeters cover the very forward region ($\pm 3.2 < \eta < \pm 4.9$). The muon spectrometer consists of a toroidal magnet providing a $B = 4$ T field and several muon chambers with different technologies in the barrel and in the end-caps. The acceptance of the muon spectrometer covers $|\eta| < 1.0$ in the barrel and extends to $\eta = \pm 2.5$ in the end-caps.

As an illustration of the ATLAS performances for measuring quarkonium signals, the right panel of Fig. 50 shows the invariant mass spectrum of high-mass muons pairs. In the full η acceptance, the corresponding mass resolution is $145 \text{ MeV}/c^2$. The corresponding expected statistics for one month of Pb–Pb minimum-bias collisions is $10 - 15 \cdot 10^3$ (with a muon p_t threshold of $3 \text{ GeV}/c$). The number of reconstructed J/ψ ranges from 8000 to $216 \cdot 10^3$ depending on the trigger threshold.

4.3 Quarkonia in heavy ion collisions at the SIS-300

While the future heavy-ion experiments at RHIC-II and at the LHC will focus on the study of the QCD phase diagram at large temperatures and small chemical potential, the SIS-300 accelerator at FAIR aims at exploring the region of moderate temperatures and large baryon chemical potentials. In this region of the phase diagram, LQCD calculations predict a critical end-point whose location is not precisely known. Beyond this critical end-point, for higher baryon chemical potentials and lower temperatures, one expects a first order phase transition from hadronic to partonic matter. This regime has been very little explored experimentally so far. Indeed, the corresponding beam energy range (from $\sim 10 \text{ AGeV}$ to $\sim 45 \text{ AGeV}$) has only been partially covered in the past by pioneering experiments at the AGS in Brookhaven and, more recently, by experiments at CERN. A non-monotonous behavior was observed in the excitation function of several observables, such as the $\langle K^+ \rangle / \langle \pi^+ \rangle$ ratio, at a beam energy of about 30 AGeV . An interpretation of this intriguing finding as a signal for the onset of deconfinement is still under debate. Note that a low mass dielectron enhancement was also observed at 40 AGeV by the CERES experiment [217] and could corroborate the trend in the $\langle K^+ \rangle / \langle \pi^+ \rangle$ excitation function. In fact, experimental limitations, both from the accelerators (beam intensities) and from the detectors (capabilities to measure rare signals) prevented comprehensive measurements to be performed at such low beam energies. Consequently, charm (and charmonium) hadrons have never been measured in this beam energy range. Such measurements could be, however, especially interesting as this beam energy range is close to the production threshold for $c\bar{c}$ pairs. Therefore, the characteristics of the produced charm hadrons are expected to be particularly sensitive to the properties of the medium in the early stage of the collision. We further note that this region of the phase diagram is well suited for investigating properties of hadrons in a dense baryonic medium. This is based on the increasing gap between the putative phase boundary and the chemical freeze-out line when decreasing the beam energy from RHIC and top-SPS to FAIR. It furthermore suggests that, contrary to RHIC and top-SPS energies, at FAIR energies the produced system spends a relatively long time in a dense baryonic phase¹⁰.

¹⁰Note, however, that the uncertainty from LQCD calculations on the phase boundary is still large.

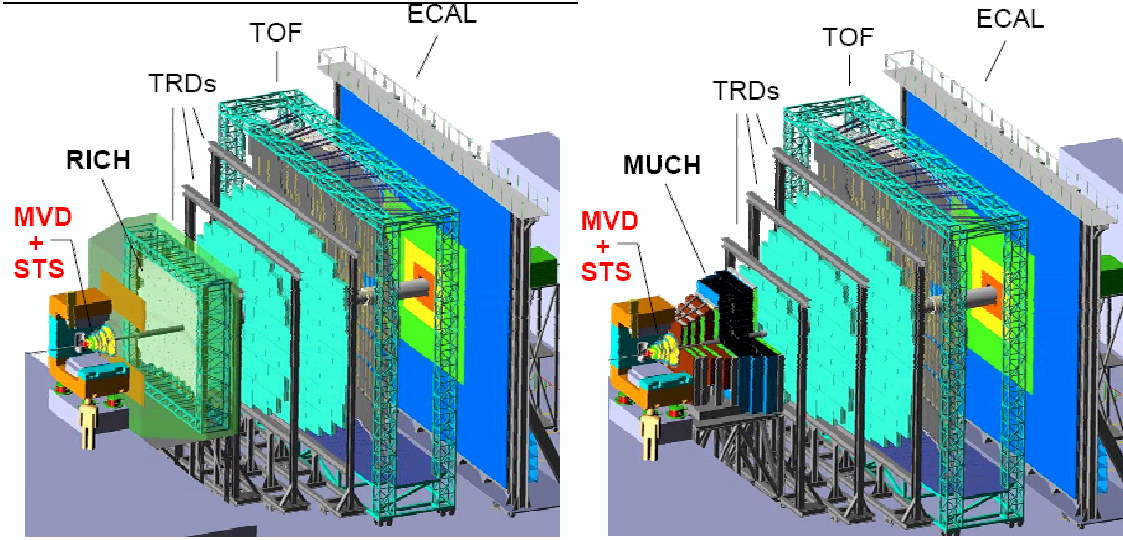


Figure 51: Longitudinal view of the CBM detector. Left: configuration for electron-hadron measurements. Right: configuration for muon measurements.

4.3.1 Experimental conditions

The SIS-300 synchrotron at the FAIR facility will deliver heavy-ion beams from 10 AGeV up to 35 AGeV for uranium and up to 45 AGeV for lighter ions with $Z/A = 0.5$. Proton beams will be available up to 90 GeV. Thanks to the unprecedented high beam intensities of $2 \cdot 10^9/\text{s}$, rare probes such as J/ψ , whose typical production rate is $2 \cdot 10^{-5}$ per central Au–Au collision at 25 AGeV, will become available. Detection of such a small signal in such a high intensity environment and among about 1000 charged tracks per event is highly challenging. It requires excellent detector performances in terms of radiation hardness, read-out speed, online-event selection, particle identification and data processing. The CBM detector is currently being designed to meet these requirements.

4.3.2 The CBM experiment

The CBM experiment is a next generation of fixed target universal detector capable of measuring hadronic, leptonic and photonic probes in a large geometrical acceptance with good vertexing. Currently, two configurations are being evaluated for electron and muon measurements (Fig. 51). Hadron track reconstruction and momentum measurements will be performed by the Silicon Tracking System (STS) which consists of several stations of radiation hard silicon strips located inside the aperture of a 1 Tm bending dipole magnet. Displaced vertices will be measured with high precision by means of a Micro Vertex Detector (MVD) based on monolithic active pixel sensors operated in vacuum close to the target. Electrons will be identified by a combination of RICH and TRD detectors placed downstream. For muon measurements, the RICH detector will be replaced by an active absorber system (MUCH) made of sandwiches of detection planes and iron layers. The setup is completed by a RPC-based Time-Of-Flight (TOF) system for charged hadron measurements and by an Electromagnetic Calorimeter (ECAL) for neutral particle measurements.

Figure 52 shows the J/ψ signal extracted from $4 \cdot 10^{10}$ central Au–Au collisions at 25 AGeV. The simulation assumes a π^\pm suppression of 10^4 from the RICH, TRD and TOF systems in the electron channel and a very good suppression of muons from π^\pm , K^\pm decay in the muon channel thanks to kink detection with the STS. The obtained reconstruction performances are comparable in both channels.

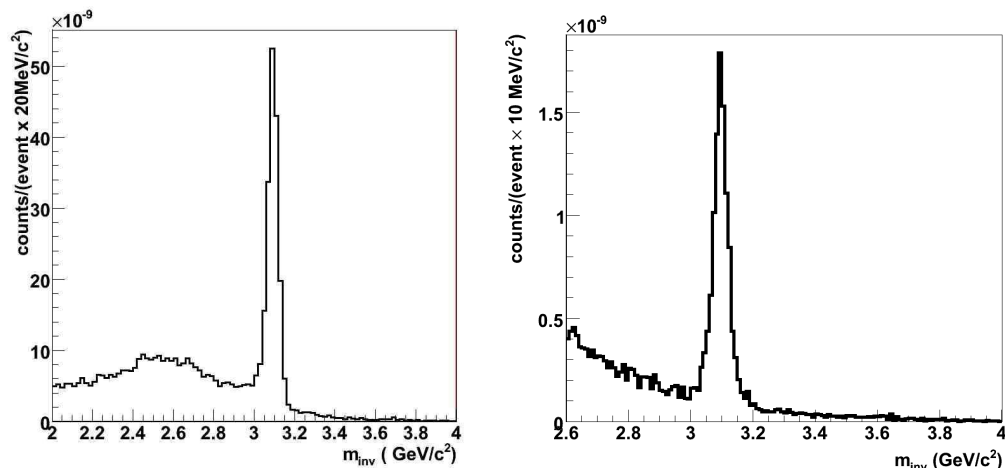


Figure 52: Invariant mass spectrum showing J/ψ reconstruction in central Au–Au collisions at 25 AGeV with the CBM detector in the electron (left) and the muon (right) channels [218].

5 Summary

The description of quarkonium production in ultrarelativistic heavy-ion collisions remains a challenging task, but new insights keep emerging on the three major frontiers, i.e., theoretical, phenomenological and experimental. In this review we have elaborated on recent developments in the above areas, and have attempted to combine the current knowledge toward developing a consistent framework.

First principle lattice QCD computations of quarkonium correlation functions at finite temperature, now also available including dynamical light quarks, have consolidated the finding that ground-state charmonia (bottomonia) are little affected up to temperatures of $\sim 2(3) T_c$. This translates into the presence of bound (or resonance) states in the pertinent spectral functions, as extracted from the Euclidean correlators using probabilistic methods. On the other hand, lQCD computations of the free energy of a heavy-quark pair clearly exhibit the effect of color screening. When the free energies are employed as a potential model in a Schrödinger equation, the J/ψ melts at significantly smaller temperatures than suggested by the correlators, slightly above T_c . Higher melting temperatures are obtained when employing the lQCD-based internal energies, which apparently agrees better with the spectral function results. For both cases, potential models are able to reproduce the approximate constancy of the correlation functions. One of the main reasons for this somewhat unsatisfactory situation is that a reduced binding can be compensated by a reduced open-charm threshold, corresponding to a reduced thermal charm-quark mass. Furthermore, nonperturbative rescattering effects typically lead to a large enhancement in the continuum part of the quarkonium spectral functions, especially close to threshold. Thus, in addition to better criteria for the definition of a potential at finite temperature, a reliable determination of the in-medium charm-quark mass, as well as of finite width effects (for both charmonia and open-charm states), are needed for improved evaluations of the dissolution temperatures. The in-medium binding energies turn out to play an important role in the dissociation reactions: while for strong binding leading-order gluo-dissociation is the most important process, next-to-leading order processes (“quasifree” destruction) are dominant for weakly bound quarkonia, especially close to the “melting” temperatures. The pertinent inelastic widths reach up to several hundred MeV, translating into lifetimes (well) below 1 fm/c. This reiterates that a consistent treatment of screening and finite width effects is mandatory. Similar considerations apply to the hadronic phase, as well as the transition region, where, in particular, the spectral properties of open-charm states are expected to change appreciably. Taking guidance from well developed concepts in electromagnetic plasma physics, finite temperature T -matrix approaches seem to be a suitable tool to incorporate all of these aspects.

In-medium equilibrium properties of quarkonia (masses and widths) are a key ingredient to transport

theoretical evaluations of quarkonium observables in heavy-ion collisions, especially if carried out in a thermally evolving bulk medium (which appears to be a reasonable approximation at SPS and RHIC). Nuclear modifications to the initial quarkonium spectra, e.g., Cronin effect, shadowing and nuclear absorption, are an important prerequisite to extract “anomalous” suppression in the medium. If, in addition, secondary regeneration (e.g., $c\bar{c}$ coalescence) occurs, the charmonium yields and spectra are coupled to the number and spectra of open charm, which themselves are subject to substantial medium modifications. We have emphasized the importance of constraining the calculations by taking advantage of the large data sets (becoming) available in collision centrality, energy, system size, and 3-momentum of the quarkonia. Current calculations find that the observed J/ψ suppression at the SPS mostly occurs in a hot/dense medium at energy densities above the critical one found in lattice QCD, with initial temperatures of $T_0 \simeq 220\text{--}250$ MeV. At RHIC energies, a significant regeneration component develops, accounting for up to 50% of the measured J/ψ yield in central Au-Au. This assertion is corroborated by the observed narrowing in the rapidity distributions and an approximately constant average transverse momentum with increasing centrality, where regeneration is concentrated at low p_t . If regeneration becomes dominant at LHC, a qualitatively new (increasing) centrality dependence of the nuclear modification factor has been predicted. A more direct probe for color screening could be the Υ : with its vacuum binding energy, it is rather inert under RHIC conditions, but an in-medium reduction in binding increases the dissociation rates noticeably which might suppress Υ production as much as J/ψ production! Such a signal benefits from the absence of bottomonium regeneration at RHIC. A similar feature is plausible (or may be even more pronounced) at the LHC, especially if regeneration for the J/ψ is large (while it is still expected to be small for Υ). Transverse-momentum spectra will further illuminate the different mechanisms, and/or reveal new ones. E.g., first RHIC data for J/ψ ’s at high $p_t \geq 5$ GeV indicate a nuclear modification factor close to one, very different from light hadron spectra. Elliptic flow is another good discriminator between direct and secondary production. Finally, the in-medium “spectroscopy” of the Ψ and Υ families might eventually provide the long suggested “thermometer” of QCD matter.

The quantitative realization of the above observables requires an advanced experimentation which will become available at RHIC-II and the LHC. While the former appears to operate at an energy suited to study the properties of a strongly coupled, liquid-like QGP, the latter may, for the first time, reach into a weakly coupled gas-like regime. At lower energies, the FAIR project is aimed at studying matter at maximum (net) baryon density; little (nothing) is known theoretically (experimentally) about charmonium properties under these conditions. In view of these developments, and with an adequate theoretical support, the climax in utilizing quarkonia to probe high-energy density matter in heavy-ion collisions may not have been reached yet.

Acknowledgment

We are indebted to A. Andronic, R. Averbeck, A. Beraudo and P. Senger for useful comments. The work of RR has been supported by a U.S. National Science Foundation CAREER award under grant no. PHY-0449489, and by a Bessel Research Award from the A.-v.-Humboldt foundation.

References

- [1] T. Matsui and H. Satz, Phys. Lett. B **178**, 416 (1986).
- [2] R. Vogt, Phys. Rept. **310**, 197 (1999).
- [3] N.F. Mott, Rev. Mod. Phys. **40**, 677 (1968).
- [4] R. Redmer, Phys. Rep. **282**, 35 (1997).

- [5] C. Baglin *et al.* [NA38 Collaboration], Phys. Lett. B **220** (1989) 471.
- [6] C. Gerschel and J. Hüfner, Z. Phys. C **56**, 171 (1992).
- [7] C. Gerschel and J. Hüfner, Phys. Lett. B **207**, 253 (1988).
- [8] S. Gavin, M. Gyulassy and A. Jackson, Phys. Lett. B **207**, 257 (1988).
- [9] R. Vogt, M. Prakash, P. Koch and T. H. Hansson, Phys. Lett. B **207**, 263 (1988).
- [10] M. Gonin *et al.* [NA50 Collaboration], Nucl. Phys. A **610**, 404C (1996).
- [11] M. C. Abreu *et al.* [NA50 Collaboration], Phys. Lett. B **410**, 337 (1997).
- [12] J. P. Blaizot and J. Y. Ollitrault, Phys. Rev. Lett. **77**, 1703 (1996)
- [13] D. Kharzeev, C. Lourenco, M. Nardi and H. Satz, Z. Phys. C **74**, 307 (1997)
- [14] R. Arnaldi *et al.* [NA60 Collaboration], Nucl. Phys. A **783**, 261 (2007)
- [15] R. Arnaldi *et al.* [NA60 Collaboration], Nucl. Phys. A **774** (2006) 711.
- [16] M. C. Abreu *et al.* [NA50 Collaboration], Phys. Lett. B **477**, 28 (2000).
- [17] L. Grandchamp, R. Rapp and G. E. Brown, Phys. Rev. Lett. **92**, 212301 (2004)
- [18] R. L. Thews, Eur. Phys. J. C **43**, 97 (2005)
- [19] M. J. Leitch, AIP Conf. Proc. **892** (2007) 404 [arXiv:nucl-ex/0610031].
- [20] A. Adare *et al.* [PHENIX Collaboration], Phys. Rev. Lett. **98**, 232301 (2007)
- [21] P. Braun-Munzinger and J. Stachel, Phys. Lett. B **490**, 196 (2000)
- [22] R. L. Thews, M. Schroedter and J. Rafelski, Phys. Rev. C **63**, 054905 (2001)
- [23] L. Grandchamp and R. Rapp, Phys. Lett. B **523**, 60 (2001)
- [24] C. E. Detar and J. B. Kogut, Phys. Rev. D **36**, 2828 (1987).
- [25] K. D. Born, S. Gupta, A. Irback, F. Karsch, E. Laermann, B. Petersson and H. Satz [MT(c) Collaboration], Phys. Rev. Lett. **67**, 302 (1991).
- [26] M. Asakawa, T. Hatsuda and Y. Nakahara, Prog. Part. Nucl. Phys. **46**, 459 (2001)
- [27] M. Asakawa and T. Hatsuda, Phys. Rev. Lett. **92**, 012001 (2004)
- [28] S. Datta, F. Karsch, P. Petreczky and I. Wetzorke, Phys. Rev. D **69**, 094507 (2004)
- [29] R. Morrin, A. P. O Cais, M. B. Oktay, M. J. Peardon, J. I. Skullerud, G. Aarts and C. R. Allton, PoS **LAT2005**, 176 (2006)
- [30] A. Jakovac, P. Petreczky, K. Petrov and A. Velytsky, Phys. Rev. D **75**, 014506 (2007)
- [31] G. Aarts, C. Allton, M. B. Oktay, M. Peardon and J. I. Skullerud, Phys. Rev. D **76**, 094513 (2007);
M. B. Oktay, M. J. Peardon, J. I. Skullerud, G. Aarts and C. R. Allton, PoS LAT2007, 227 (2007).
- [32] K. Petrov, A. Jakovac, P. Petreczky and A. Velytsky, PoS **LAT2005**, 153 (2006)

- [33] L. D. McLerran and B. Svetitsky, Phys. Lett. B **98**, 195 (1981).
- [34] G. S. Bali, Phys. Rept. **343**, 1 (2001)
- [35] N. Brambilla *et al.*, CERN Yellow Rep. 2005-005, arXiv:hep-ph/0412158.
- [36] O. Kaczmarek and F. Zantow, Phys. Rev. D **71**, 114510 (2005)
- [37] O. Kaczmarek, F. Karsch, P. Petreczky and F. Zantow, Phys. Lett. B **543**, 41 (2002)
- [38] P. Petreczky and K. Petrov, Phys. Rev. D **70**, 054503 (2004)
- [39] N. Brambilla, J. Ghiglieri, A. Vairo and P. Petreczky, arXiv:0804.0993 [hep-ph].
- [40] F. Karsch, M. T. Mehr and H. Satz, Z. Phys. C **37**, 617 (1988).
- [41] O. Kaczmarek, F. Karsch, F. Zantow and P. Petreczky, Phys. Rev. D **70**, 074505 (2004) [Erratum-
ibid. D **72**, 059903 (2005)]
- [42] S. Digal, P. Petreczky and H. Satz, Phys. Rev. D **64**, 094015 (2001)
- [43] E. V. Shuryak and I. Zahed, Phys. Rev. D **70**, 054507 (2004)
- [44] C. Y. Wong, Phys. Rev. C **72**, 034906 (2005)
- [45] W. M. Alberico, A. Beraudo, A. De Pace and A. Molinari, Phys. Rev. D **72**, 114011 (2005)
- [46] M. Mannarelli and R. Rapp, Phys. Rev. C **72**, 064905 (2005).
- [47] R. Rapp, Eur. Phys. J A **18**, 459 (2003).
- [48] A. Mocsy and P. Petreczky, Phys. Rev. D **73**, 074007 (2006)
- [49] W. M. Alberico, A. Beraudo, A. De Pace and A. Molinari, Phys. Rev. D **75**, 074009 (2007)
- [50] D. Cabrera and R. Rapp, Phys. Rev. D **76**, 114506 (2007)
- [51] W. Ebeling, W.-D. Kraeft, D. Kremp, G. Röpke, *Quantum Statistics of Charged Many-Particle Systems*, Plenum, New York (1986).
- [52] R. Machleidt, Adv. Nucl. Phys. **19**, 189 (1989).
- [53] O. Kaczmarek and F. Zantow, arXiv:hep-lat/0506019.
- [54] T. Umeda, Phys. Rev. D **75**, 094502 (2007)
- [55] P. Petreczky and D. Teaney, Phys. Rev. D **73**, 014508 (2006)
- [56] D. Cabrera and R. Rapp, in preparation (2008).
- [57] A. Mocsy and P. Petreczky, Phys. Rev. Lett. **99**, 211602 (2007); Phys. Rev. D **77**, 014501 (2008).
- [58] W. M. Alberico, A. Beraudo, A. De Pace and A. Molinari, Phys. Rev. D **77**, 017502 (2008).
- [59] S. Datta, A. Jakovac, F. Karsch and P. Petreczky, AIP Conf. Proc. **842**, 35 (2006)
- [60] C. Y. Wong and H. W. Crater, Phys. Rev. D **75**, 034505 (2007)

- [61] G. Bhanot and M. E. Peskin, Nucl. Phys. B **156**, 391 (1979).
- [62] M. E. Peskin, Nucl. Phys. B **156**, 365 (1979).
- [63] F. Arleo, J. Cugnon and Y. Kalinovsky, Phys. Lett. B **614**, 44 (2005).
- [64] D. Blaschke, Y. Kalinovsky and V. Yudichev, Lect. Notes Phys. **647**, 366 (2004).
- [65] L. Grandchamp and R. Rapp, Nucl. Phys. A **709**, 415 (2002)
- [66] G. Röpke, D. Blaschke and H. Schulz, Phys. Rev. D **38**, 3589 (1988).
- [67] D. Kharzeev, L. D. McLerran and H. Satz, Phys. Lett. B **356**, 349 (1995)
- [68] Y. Park, K. I. Kim, T. Song, S. H. Lee and C. Y. Wong, Phys. Rev. C **76**, 044907 (2007)
- [69] T. Song, Y. Park, S. H. Lee and C. Y. Wong, Phys. Lett. B **659**, 621 (2008)
- [70] X. Zhao and R. Rapp, arXiv:0712.2407[hep-ph], Phys. Lett. B in press.
- [71] B. L. Combridge, Nucl. Phys. B **151**, 429 (1979).
- [72] L. Grandchamp, S. Lumpkins, D. Sun, H. van Hees and R. Rapp, Phys. Rev. C **73**, 064906 (2006)
- [73] K. Martins, D. Blaschke and E. Quack, Phys. Rev. C **51**, 2723 (1995).
- [74] T. Barnes and E. S. Swanson, Phys. Rev. D **46**, 131 (1992).
- [75] D. Blaschke and G. Ropke, Phys. Lett. B **299**, 332 (1993).
- [76] C. Y. Wong, E. S. Swanson and T. Barnes, Phys. Rev. C **62**, 045201 (2000)
- [77] T. Barnes, E. S. Swanson, C. Y. Wong and X. M. Xu, Phys. Rev. C **68**, 014903 (2003)
- [78] C. D. Roberts and A. G. Williams, Prog. Part. Nucl. Phys. **33**, 477 (1994)
- [79] D.B. Blaschke, G.R.G. Burau, M.A. Ivanov, Yu.L. Kalinovsky and P. C. Tandy, arXiv:hep-ph/0002047.
- [80] M. A. Ivanov, J. G. Korner and P. Santorelli, Phys. Rev. D **70**, 014005 (2004)
- [81] S. G. Matinyan and B. Muller, Phys. Rev. C **58**, 2994 (1998)
- [82] K. L. Haglin, Phys. Rev. C **61**, 031902 (2000)
- [83] Z. w. Lin and C. M. Ko, Phys. Rev. C **62**, 034903 (2000)
- [84] K. L. Haglin and C. Gale, Phys. Rev. C **63**, 065201 (2001)
- [85] Z. w. Lin and C. M. Ko, Nucl. Phys. A **715**, 533 (2003)
- [86] Y. s. Oh, T. Song and S. H. Lee, Phys. Rev. C **63**, 034901 (2001)
- [87] V. V. Ivanov, Yu. L. Kalinovsky, D. Blaschke and G. R. G. Burau, arXiv:hep-ph/0112354.
- [88] Y. s. Oh, T. s. Song, S. H. Lee and C. Y. Wong, J. Korean Phys. Soc. **43**, 1003 (2003)
- [89] A. Bourque, C. Gale and K. L. Haglin, Phys. Rev. C **70**, 055203 (2004)

- [90] A. Sibirtsev, K. Tsushima and A. W. Thomas, Phys. Rev. C **63**, 044906 (2001)
- [91] W. Liu, C. M. Ko and Z. W. Lin, Phys. Rev. C **65**, 015203 (2002).
- [92] Z. w. Lin and C. M. Ko, Phys. Lett. B **503**, 104 (2001)
- [93] A. Sibirtsev, K. Tsushima, K. Saito and A. W. Thomas, Phys. Lett. B **484**, 23 (2000)
- [94] K. Tsushima, A. Sibirtsev, K. Saito, A. W. Thomas and D. H. Lu, Nucl. Phys. A **680**, 280 (2001)
- [95] G. R. G. Burau, D. B. Blaschke and Y. L. Kalinovsky, Phys. Lett. B **506**, 297 (2001).
- [96] D. Blaschke, G. Burau, Yu. Kalinovsky, V. Yudichev, Prog. Theor. Phys. Suppl. **149**, 182 (2003).
- [97] C. Fuchs, B. V. Martemyanov, A. Faessler and M. I. Krivoruchenko, Phys. Rev. C **73**, 035204 (2006).
- [98] D. Blaschke, G. Burau and Yu. L. Kalinovsky, arXiv:nucl-th/0006071.
- [99] D. Blaschke, G. Burau, Yu. Kalinovsky and T. Barnes, Eur. Phys. J. A **18**, 547 (2003) [arXiv:nucl-th/0211058].
- [100] M. Schlages, Th. Bornath and D. Kremp, Phys. Rev. A **38**, 2174 (1988).
- [101] R. Zimmermann, K. Kilimann, W. D. Kraeft, D. Kremp and G. Röpke, phys. stat. sol. (b) **90**, 175 (1978).
- [102] G. Röpke, et al., Nucl. Phys. A **379**, 536 (1982)
- [103] G. Röpke, et al., Nucl. Phys. A **399**, 587 (1983)
- [104] C. J. Horowitz, E. J. Moniz and J. W. Negele, Phys. Rev. D **31**, 1689 (1985).
- [105] G. Ropke, D. Blaschke and H. Schulz, Phys. Rev. D **34**, 3499 (1986).
- [106] A. Beraudo, J. P. Blaizot and C. Ratti, arXiv:0712.4394 [nucl-th].
- [107] W. Ebeling and K. Kilimann, Z. Naturforsch. **44a**, 519 (1989).
- [108] F. J. Rogers, H. C. Garboske, Jr. and D. J. Harwood, Phys. Rev. A **1**, 1577 (1970).
- [109] G. W. Fehrenbach, W. Schäfer, J. Treusch, and R. G. Ulbrich, Phys. Rev. Lett. **49**, 1281 (1981)
- [110] G. Ecker and W. Weitzel, Ann. Phys. (Lpz.) **17**, 126 (1956).
- [111] V. V. Dixit, Mod. Phys. Lett. A **5**, 227 (1990).
- [112] M. B. Voloshin, arXiv:0711.4556 [hep-ph].
- [113] A. Capella, E. G. Ferreira and A. B. Kaidalov, Phys. Rev. Lett. **85**, 2080 (2000)
- [114] W. Cassing and C. M. Ko, Phys. Lett. B **396**, 39 (1997)
- [115] C. Spieles *et al.*, Phys. Lett. B **458**, 137 (1999).
- [116] A. K. Chaudhuri, Phys. Rev. C **68**, 037901 (2003)
- [117] C. M. Ko, B. Zhang, X. N. Wang and X. F. Zhang, Phys. Lett. B **444**, 237 (1998)

- [118] P. Braun-Munzinger and K. Redlich, Eur. Phys. J. C **16**, 519 (2000).
- [119] M. Gazdzicki and M. I. Gorenstein, Phys. Rev. Lett. **83**, 4009 (1999)
- [120] M. I. Gorenstein, A. P. Kostyuk, H. Stöcker and W. Greiner, Phys. Lett. B **509**, 277 (2001)
- [121] A. Andronic, P. Braun-Munzinger, K. Redlich and J. Stachel, Nucl. Phys. A **789**, 334 (2007)
- [122] H. van Hees, M. Mannarelli, V. Greco and R. Rapp, Phys. Rev. Lett. **100**, 192301 (2008)
- [123] V. Greco, C. M. Ko and R. Rapp, Phys. Lett. B **595**, 202 (2004)
- [124] L. Yan, P. Zhuang and N. Xu, Phys. Rev. Lett. **97**, 232301 (2006)
- [125] P. Levai, B. Müller and X. N. Wang, Phys. Rev. C **51**, 3326 (1995)
- [126] S. S. Adler *et al.* [PHENIX Collaboration], Phys. Rev. Lett. **94**, 082301 (2005)
- [127] R. Shahoyan [NA60 Collaboration], J. Phys. G **34**, S1029 (2007).
- [128] K. A. Bugaev, M. Gazdzicki and M. I. Gorenstein, Phys. Lett. B **523**, 255 (2001)
- [129] R. L. Thews and M. L. Mangano, Phys. Rev. C **73**, 014904 (2006)
- [130] R. Rapp and L. Grandchamp, J. Phys. G **30**, S305 (2004)
- [131] A. Andronic, P. Braun-Munzinger, K. Redlich and J. Stachel, Phys. Lett. B **659**, 149 (2008)
- [132] V. Greco, H. van Hees and R. Rapp, arXiv:0709.4452 [hep-ph].
- [133] P. B. Gossiaux, V. Guiho and J. Aichelin, J. Phys. G **31**, S1079 (2005)
- [134] F. Karsch and R. Petronzio, Phys. Lett. B **193**, 105 (1987).
- [135] J. P. Blaizot and J. Y. Ollitrault, Phys. Lett. B **199**, 499 (1987).
- [136] M. C. Chu and T. Matsui, Phys. Rev. D **37**, 1851 (1988).
- [137] G. Ropke, D. Blaschke and H. Schulz, Phys. Lett. B **202**, 479 (1988).
- [138] F. Karsch and H. Satz, Z. Phys. C **51**, 209 (1991).
- [139] J. Cugnon and P. B. Gossiaux, Phys. Lett. B **359**, 375 (1995).
- [140] B. Zhang, C. M. Ko, B. A. Li, Z. W. Lin and S. Pal, Phys. Rev. C **65**, 054909 (2002)
- [141] O. Linnyk, E. L. Bratkovskaya, W. Cassing and H. Stöcker, Nucl. Phys. A **786**, 183 (2007)
- [142] O. Linnyk, E. L. Bratkovskaya, W. Cassing and H. Stöcker, Phys. Rev. C **76**, 041901 (2007)
- [143] E. L. Bratkovskaya, W. Cassing and H. Stöcker, Phys. Rev. C **67**, 054905 (2003)
- [144] A. Capella, L. Bravina, E. G. Ferreira, A. B. Kaidalov, K. Tywoniuk and E. Zabrodin, arXiv:0712.4331 [hep-ph].
- [145] M. J. Leitch *et al.* [FNAL E866/NuSea collaboration], Phys. Rev. Lett. **84**, 3256 (2000)
- [146] P. Faccioli [HERA-B Collaboration], AIP Conf. Proc. **814**, 545 (2006).

- [147] B. Alessandro *et al.* [NA50 Collaboration], Eur. Phys. J. C **33**, 31 (2004).
- [148] L. Ramello [NA50 Collaboration], Nucl. Phys. A **774**, 59 (2006).
- [149] C. Lourenco, Nucl. Phys. A **783**, 451 (2007) [arXiv:nucl-ex/0612014].
- [150] Y. B. He, J. Hufner and B. Z. Kopeliovich, Phys. Lett. B **477**, 93 (2000) [arXiv:hep-ph/9908243].
- [151] T. Matsui, Annals Phys. **196**, 182 (1989).
- [152] J. Cugnon and P. B. Gossiaux, Z. Phys. C **58**, 77 (1993).
- [153] J. Cugnon and P. B. Gossiaux, Z. Phys. C **58**, 95 (1993).
- [154] D. Koudela and C. Volpe, Phys. Rev. C **69**, 054904 (2004) [arXiv:hep-ph/0301186].
- [155] J. P. Blaizot and J. Y. Ollitrault, Phys. Lett. B **217**, 386 (1989).
- [156] S. Gavin, R. Vogt, Nucl. Phys. B **345** (1990) 104.
- [157] F. Arleo, P. B. Gossiaux, T. Gousset and J. Aichelin, Phys. Rev. C **61**, 054906 (2000) [arXiv:hep-ph/9907286].
- [158] F. Arleo, P. B. Gossiaux and J. Aichelin, Phys. Rev. C **65**, 054911 (2002) [arXiv:hep-ph/0105047].
- [159] K. J. Eskola, V. J. Kolhinen and C. A. Salgado, Eur. Phys. J. C **9**, 61 (1999) [arXiv:hep-ph/9807297].
- [160] K. J. Eskola, V. J. Kolhinen and R. Vogt, Nucl. Phys. A **696**, 729 (2001) [arXiv:hep-ph/0104124].
- [161] A. Accardi *et al.*, arXiv:hep-ph/0308248.
- [162] D. de Florian and R. Sassot, Phys. Rev. D **69**, 074028 (2004) [arXiv:hep-ph/0311227].
- [163] A. Adare *et al.* [PHENIX Collaboration], Phys. Rev. C **77**, 024912 (2008) [arXiv:0711.3917 [nucl-ex]].
- [164] F. Arleo and V. N. Tram, Eur. Phys. J. C **55**, 449 (2008) [arXiv:hep-ph/0612043].
- [165] I. Abt *et al.* [HERA-B Collaboration], Phys. Lett. B **561**, 61 (2003)
- [166] I. Abt *et al.* [HERA-B Collaboration], Eur. Phys. J. C **49**, 545 (2007)
- [167] D. E. Acosta *et al.* [CDF Collaboration], Phys. Rev. D **71** (2005) 032001
- [168] X. l. Zhu, P. f. Zhuang and N. Xu, Phys. Lett. B **607**, 107 (2005)
- [169] C. Spieles, R. Vogt, L. Gerland, S. A. Bass, M. Bleicher, H. Stöcker and W. Greiner, Phys. Rev. C **60**, 054901 (1999)
- [170] S. Digal, S. Fortunato and H. Satz, Eur. Phys. J. C **32**, 547 (2004)
- [171] R. Rapp, Eur. Phys. J. C **43**, 91 (2005)
- [172] A. Capella and E. G. Ferreira, Eur. Phys. J. C **42**, 419 (2005)
- [173] B. Alessandro *et al.* [NA50 Collaboration], Eur. Phys. J. C **39**, 335 (2005)

- [174] R. Arnaldi *et al.* [NA60 Collaboration], J. Phys. G **32**, S51 (2006)
- [175] C. Lourenco *et al.* [NA60 Collaboration], PoS **HEP2005**, 133 (2006).
- [176] R. Arnaldi *et al.* [NA60 Collaboration], Phys. Rev. Lett. **99**, 132302 (2007).
- [177] H. Pereira Da Costa [PHENIX Collaboration], Nucl. Phys. A **774**, 747 (2006)
- [178] P. f. Zhuang and X. L. Zhu, Phys. Rev. C **67**, 067901 (2003)
- [179] J.P. Blaizot, J.Y. Ollitrault, Phys. Rev. D **39** (1989) 232.
- [180] L. Gerland, L. Frankfurt, M. Strikman, H. Stoecker and W. Greiner, Phys. Rev. Lett. **81**, 762 (1998)
- [181] J. P. Blaizot and J. Y. Ollitrault, Phys. Lett. B **217**, 392 (1989).
- [182] J. Hufner, Y. Kurihara and H. J. Pirner, Phys. Lett. B **215**, 218 (1988) [Acta Phys. Slov. **39**, 281 (1989)].
- [183] S. Gavin and M. Gyulassy, Phys. Lett. B **214**, 241 (1988).
- [184] M. C. Abreu *et al.* [NA50 Collaboration], Phys. Lett. B **499** (2001) 85.
- [185] M. I. Gorenstein, K. A. Bugaev and M. Gazdzicki, Phys. Rev. Lett. **88**, 132301 (2002)
- [186] D. Pal, B. K. Patra and D. K. Srivastava, Eur. Phys. J. C **17**, 179 (2000)
- [187] Z. Tang [STAR Collaboration], Proc. of 24. Winter Workshop on Nuclear Dynamics, South Padre Island (TX, USA), April 05-12, 2008; arXiv:0804.4846 [nucl-ex].
- [188] X. Zhao and R. Rapp, Proc. of 24. Winter Workshop on Nuclear Dynamics, South Padre Island (TX, USA), April 05-12, 2008; arXiv:0806.1239 [nucl-th].
- [189] X. N. Wang and F. Yuan, Phys. Lett. B **540**, 62 (2002)
- [190] H. van Hees, V. Greco and R. Rapp, Phys. Rev. C **73**, 034913 (2006)
- [191] A. Adare *et al.* [PHENIX Collaboration], Phys. Rev. Lett. **98**, 172301 (2007)
- [192] L. Ravagli and R. Rapp, Phys. Lett. B **655**, 126 (2007)
- [193] M. Cacciari, P. Nason and R. Vogt, Phys. Rev. Lett. **95**, 122001 (2005).
- [194] A. Adare *et al.* [PHENIX Collaboration], Phys. Rev. Lett. **98**, 232002 (2007)
- [195] A. Adare *et al.* [PHENIX Collaboration], Phys. Rev. Lett. **97**, 252002 (2006)
- [196] F. Karsch, D. Kharzeev and H. Satz, Phys. Lett. B **637**, 75 (2006)
- [197] H. Sorge, E. V. Shuryak and I. Zahed, Phys. Rev. Lett. **79**, 2775 (1997)
- [198] O. Linnyk, E. L. Bratkovskaya and W. Cassing, arXiv:0801.4282 [nucl-th].
- [199] J. F. Gunion and R. Vogt, Nucl. Phys. B **492** (1997) 301
- [200] A. D. Frawley, T. Ullrich and R. Vogt, arXiv:0806.1013 [nucl-ex].

- [201] F. Carminati *et al.* [ALICE Collaboration], J. Phys. G **30** (2004) 1517.
- [202] B. Alessandro *et al.* [ALICE Collaboration], J. Phys. G **32** (2006) 1295.
- [203] D. G. d’Enterria *et al.*, J. Phys. G **34** (2007) 2307.
- [204] ATLAS Collaboration, CERN/LHCC/**2004–009**.
- [205] CBM Collaboration, Technical Status Report (2005), <http://www.gsi.de/fair/experiments/CBM/>
- [206] T.D. Lee, Nucl. Phys. A 750 (2005) 1; T. Ludlam, Nucl. Phys. A 750 (2005) 9; M. Gyulassy and L. McLerran, Nucl. Phys. A 750 (2005) 30; E. Shuryak, Nucl. Phys. A 750 (2005) 64; B. Müller, Nucl. Phys. A 750 (2005) 84; X.-N. Wang, Nucl. Phys. A 750 (2005) 98; H. Stöcker, Nucl. Phys. A 750 (2005) 121; J.-P. Blaizot and F. Gelis, Nucl. Phys. A 750 (2005) 148.
- [207] I. Arsene *et al.* (BRAHMS Collaboration), Nucl. Phys. A 757 (2005) 1; R.R. Betts *et al.* (PHOBOS Collaboration), Nucl. Phys. A 757 (2005) 28; J. Adams *et al.* (STAR Collaboration), Nucl. Phys. A 757 (2005) 102; K. Adcox *et al.* (PHENIX Collaboration), Nucl. Phys. A 757 (2005) 184.
- [208] B. L. Ioffe and D. E. Kharzeev, Phys. Rev. C **68** (2003) 061902
- [209] J. Schukraft, Nucl. Phys. A **698** (2002) 287.
- [210] N. Armesto *et al.*, J. Phys. G **35** (2008) 054001
- [211] X. M. Xu, D. Kharzeev, H. Satz and X. N. Wang, Phys. Rev. C **53** (1996) 3051.
- [212] M. Bedjidian *et al.*, arXiv:hep-ph/0311048.
- [213] P. Braun-Munzinger and J. Stachel, Phys. Lett. B **490** (2000) 196.
- [214] A. Andronic, P. Braun-Munzinger, K. Redlich and J. Stachel, Phys. Lett. B **652** (2007) 259
- [215] W. M. Yao *et al.* [Particle Data Group], J. Phys. G **33** (2006) 1.
- [216] I. P. Lokhtin and A. M. Snigirev, Eur. Phys. J. C **21** (2001) 155.
- [217] D. Adamova *et al.* [CERES/NA45 Collaboration], Phys. Rev. Lett. **91** (2003) 042301
- [218] C. Höhne for the CBM Collaboration, Int. Journ. of Mod. Phys. E **16** (2008) 2419.